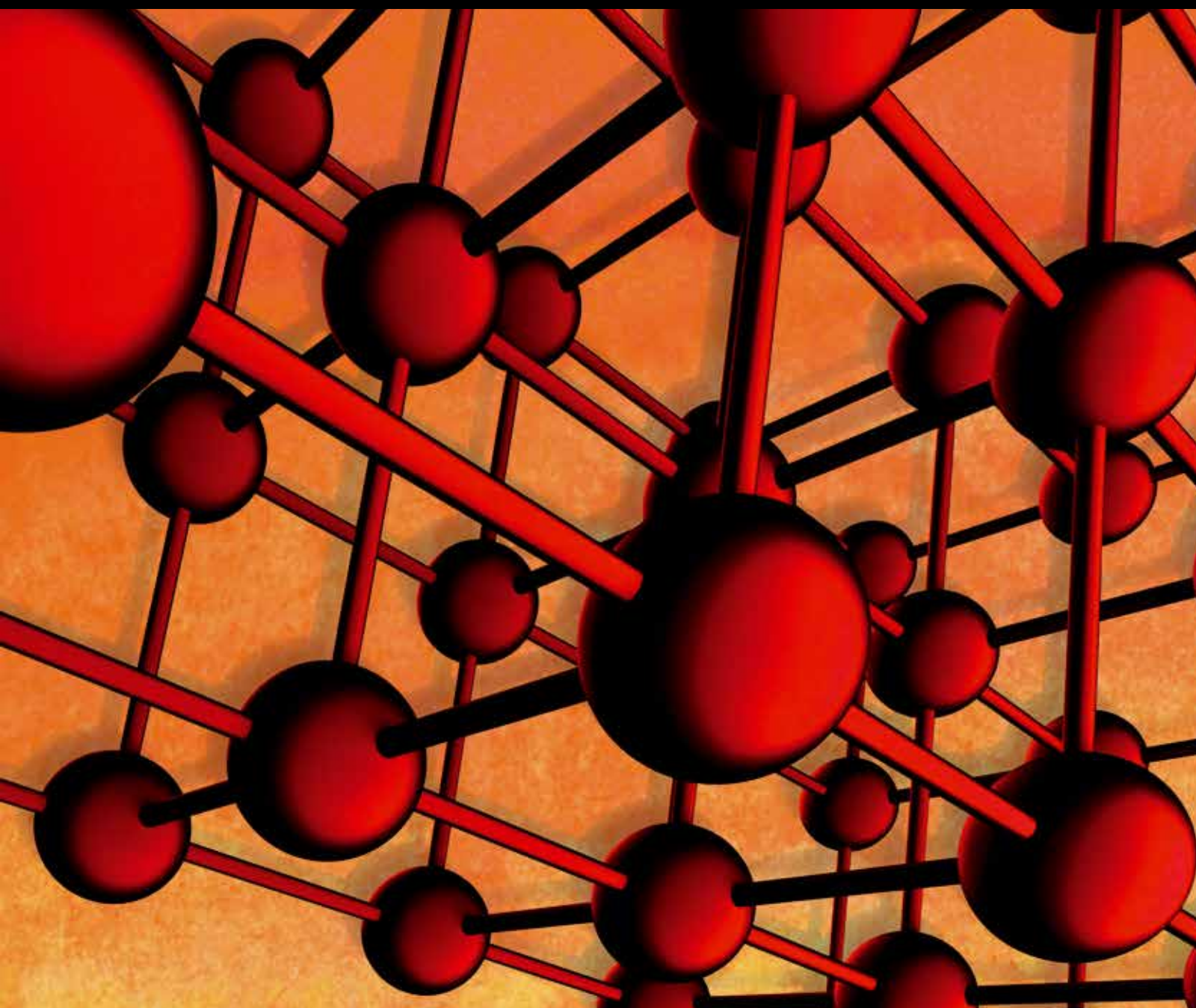


Advances in Materials Science and Engineering

Experimental and Theoretical Advances in Amorphous Alloys

Guest Editors: Na Chen, Limei Xu, Yang Shao, and Konstantinos Georgarakis





Experimental and Theoretical Advances in Amorphous Alloys

Advances in Materials Science and Engineering

Experimental and Theoretical Advances in Amorphous Alloys

Guest Editors: Na Chen, Limei Xu, Yang Shao,
and Konstantinos Georgarakis



Copyright © 2014 Hindawi Publishing Corporation. All rights reserved.

This is a special issue published in “Advances in Materials Science and Engineering.” All articles are open access articles distributed under the Creative Commons Attribution License, which permits unrestricted use, distribution, and reproduction in any medium, provided the original work is properly cited.

Editorial Board

- Dimitrios G. Aggelis, Belgium
K. G. Anthymidis, Greece
Amit Bandyopadhyay, USA
Arun Bansil, USA
Zoe Barber, UK
Massimiliano Barletta, Italy
Jozef Bednarcik, Germany
Jamal Berakdar, Germany
Alessandra Bianco, Italy
Susmita Bose, USA
Heinz-Gunter Brokmeier, Germany
Steve Bull, UK
Peter Chang, Canada
Daolun Chen, Canada
Manish U. Chhowalla, USA
Sanjeeviraja Chinnappanadar, India
Chi-Wai Chow, Taiwan
Narendra B. Dahotre, USA
Jie Dai, Singapore
Joo P. Davim, Portugal
Francesco Delogu, Italy
Seshu B. Desu, USA
Yong Ding, USA
Kaveh Edalati, Japan
Gilbert Fantozzi, France
Sergi Gallego, Spain
Lian Gao, China
Santiago Garcia-Granda, Spain
Filippo Giannazzo, Italy
Hiroki Habazaki, Japan
Joke Hadermann, Belgium
Richard Hennig, USA
Rui Huang, USA
Shyh-Chin Huang, Taiwan
Baibiao Huang, China
Jacques Huot, Canada
Maarit Karppinen, Finland
Katsuyuki Kida, Japan
Jaehwan Kim, Republic of Korea
Jae-Ho Kim, Republic of Korea
Akihiko Kimura, Japan
Takayuki Kitamura, Japan
Sridhar Komarneni, USA
Hongchao Kou, China
Prashant Kumta, USA
Jui-Yang Lai, Taiwan
Pavel Lejcek, Czech Republic
Cristina Leonelli, Italy
Markku Leskela, Finland
Bin Li, China
Feng Li, China
Ying Li, USA
Yuanhua Lin, China
Zhimin Liu, China
Meilin Liu, Georgia
Wei Liu, France
Ying Liu, USA
Jun Liu, China
Yunqi Liu, China
Haiming Lu, China
Fernando Lusquios, Spain
Peter Majewski, Australia
Philippe Miele, France
Hossein Moayedi, Malaysia
Paul Munroe, Australia
Luigi Nicolais, Italy
Hiroshi Noguchi, Japan
José L. Ocaña, Spain
Tsutomu Ohzuku, Japan
Xiaoqing Pan, USA
Bart Partoens, Belgium
Ganapathiraman Ramanath, USA
Manijeh Razeghi, USA
Antonio Riveiro, Spain
Pascal Roussel, France
Fawzy H. Samuel, Canada
Jainagesh A. Sekhar, USA
Jiangbo Sha, China
Liyuan Sheng, China
Fridon Shubitidze, USA
You Song, China
Charles C. Sorrell, Australia
Costas M. Soukoulis, USA
Sam-Shajing Sun, USA
Weihua Tang, China
Kohji Tashiro, Japan
Philippe Thomas, France
Somchai Thongtem, Thailand
Achim Trampert, Germany
Vladimir Tsukruk, USA
Filip Tuomisto, Finland
Stuart Turner, Belgium
Krystyn Van Vliet, USA
Rui Vilar, Portugal
Holger von Wenckstern, Germany
Rong Wang, USA
Min Wang, China
Rui Wang, China
Qiang Wang, China
Lu Wei, China
Jörg M K Wiezorek, USA
Wei Wu, USA
Gongnan Xie, China
Aiguo Xu, China
Hemmige S. Yathirajan, India
Jianqiao Ye, UK
Wenbin Yi, China
Jinghuai Zhang, China
Tao Zhang, China
Bin Zhang, China
Jun Zhang, China
Jian Zhang, Singapore
Kai Zhang, China
Kai Zhang, China
Jing Zhang, China
Li Zhang, China
Ming-Xing Zhang, Australia
Wei Zhou, China

Contents

Experimental and Theoretical Advances in Amorphous Alloys, Na Chen, Limei Xu, Yang Shao, and Konstantinos Georgarakis
Volume 2014, Article ID 514104, 2 pages

Investigation of Mechanical Properties and Plastic Deformation Behavior of $(\text{Ti}_{45}\text{Cu}_{40}\text{Zr}_{10}\text{Ni}_5)_{100-x}\text{Al}_x$ Metallic Glasses by Nanoindentation, Lanping Huang, Xuzhe Hu, TaoTao Guo, and Song Li
Volume 2014, Article ID 215093, 5 pages

Formation and Mechanical Properties of Pd-Si Binary Bulk Metallic Glasses, Na Chen, Hongxia Zhang, and Ke-Fu Yao
Volume 2014, Article ID 647197, 5 pages

Amorphous Alloy: Promising Precursor to Form Nanoflowerpot, Guo Lan, Zhiqiang Xie, Zhenwei Huang, Shengchen Yang, Xuhai Zhang, Yuqiao Zeng, and Jianqing Jiang
Volume 2014, Article ID 263681, 5 pages

Selection of the Composition with High Glass Forming Ability in Zr-Cu-Ni-Al Bulk Metallic Glasses, Yajuan Sun, Yumin Li, and Hongjing Wang
Volume 2014, Article ID 827191, 6 pages

Nanocrystalline Phase Formation inside Shear Bands of Pd-Cu-Si Metallic Glass, Yang Shao, Guannan Yang, and Kefu Yao
Volume 2014, Article ID 490181, 4 pages

A Ti/Ti-Based-Metallic-Glass Interpenetrating Phase Composite with Remarkable Mutual Reinforcement Effect, J. Mu, Z. W. Zhu, H. F. Zhang, H. W. Zhang, H. M. Fu, H. Li, A. M. Wang, and Z. Q. Hu
Volume 2014, Article ID 127172, 6 pages

Surface Crystallization in Mg-Based Bulk Metallic Glass during Copper Mold Casting, Xin Wang
Volume 2014, Article ID 798479, 4 pages

A Centimeter-Sized Quaternary Ti-Zr-Be-Ag Bulk Metallic Glass, S. F. Zhao, Y. Shao, P. Gong, and K. F. Yao
Volume 2014, Article ID 192187, 5 pages

Enzyme-Free Electrochemical Glucose Sensors Prepared by Dealloying Pd-Ni-P Metallic Glasses, Yuqiao Zeng, Hua Xiang, Chunlei Yang, Shengchen Yang, Luyang Chen, Mingwei Chen, Akihisa Inoue, Xuhai Zhang, and Jianqing Jiang
Volume 2014, Article ID 518641, 6 pages

Editorial

Experimental and Theoretical Advances in Amorphous Alloys

Na Chen,¹ Limei Xu,² Yang Shao,¹ and Konstantinos Georgarakis³

¹*School of Materials Science and Engineering, Tsinghua University, Beijing 100084, China*

²*International Center for Quantum Materials, Peking University, Beijing 100084, China*

³*WPI Advanced Institute for Materials Research, Sendai 9808577, Japan*

Correspondence should be addressed to Na Chen; chennadm@mail.tsinghua.edu.cn

Received 2 September 2014; Accepted 2 September 2014; Published 31 December 2014

Copyright © 2014 Na Chen et al. This is an open access article distributed under the Creative Commons Attribution License, which permits unrestricted use, distribution, and reproduction in any medium, provided the original work is properly cited.

Unlike crystalline alloys having long-range order in atomic arrangements, amorphous alloys are disordered solids [1–4]. Yet their structure when solidified is not completely disordered but contains short- to medium-range ordered clusters [5, 6]. This unique structure endows them with superior mechanical, physical, and chemical properties. Therefore, amorphous alloys are of both scientific and technological interests. Recent progress in experimental and computational techniques has greatly advanced our understanding of a number of key issues such as glass structure at atomic level, glass-forming ability (GFA), and structure-property relationship in this field [7, 8]. In spite of this, ongoing research efforts remain necessary to uncover the atomic-level mechanisms underlying the glass formation and the deformation, as well as the glass structure.

Bulk amorphous alloys (BAAs) with diameters of more than one centimeter are preferred for practical engineering applications. To develop such alloy systems with extremely high GFA, several strategies, including large undercooling (LU), Inoue's three empirical rules (ITER), and flux treatment, have been proposed [2, 9–11]. Among them, minor alloying additions (MAA) and fluxing prove to be significantly beneficial for enhancing GFA and thus enabling the formation of centimeter-scale BAAs [12–14]. As listed in Table 1, a combination of these strategies could be employed for producing centimeter-scale BAAs.

In addition to glass formation, the mechanical property of amorphous alloys is also one of the hot topics in this field. Although shear localization is responsible for their catastrophic failure, there is a need for a better understanding of initiation, development, and percolation of these shear

transformation events. At atomic level, shear transformation zones (STZs) are supposed to be activated in response to external stimuli and eventually develop into shear bands during deformation. Unfortunately, these clusters are very small with an average size of ~1 nm and appear only at a very early stage of deformation, which makes it very difficult to be observed experimentally. On the other hand, both structural disordering and the formation of nanocrystals have been evidenced inside shear bands after deformation [15], implying that atomic rearrangements must occur. Moreover, the nanocrystal size and their distributions could be related to shear transformations, particularly when the energy barrier to crystallize is comparable to or even smaller than that to activate percolated STZs globally. As a consequence of deformation, structural evolution inside shear bands could help uncover the underlying deformation mechanisms for amorphous alloys.

Last but not least, dealloying amorphous alloys has raised tremendous attentions by producing highly active nanoporous metals used for catalysts and electric devices such as solar cells, sensors, or some other electric components. This provides a convenient way to design novel nanostructured materials with desirable functionalities.

In summary, this special issue is mainly focused on the development of bulk amorphous alloy, mechanical response, and new functionalities explored in amorphous alloys. We hope that the readers will find in this special issue not only interesting experimental results on the formation of centimeter-scale BAAs induced by fluxing or minor alloy additions and new functional nanoporous metals by dealloying amorphous alloys and amorphous alloy composites

TABLE 1: The strategies for producing centimeter-scale amorphous alloys.

Representative BAAs	Critical size for glass formation (mm)	LU	ITER	Fluxing	MAA
Pd-Ni-Cu-P [16]	80	√	√	√	√
Zr-Ti-Cu-Ni-Be [17]	50	√	√		
Cu-Zr-Al-Ag [16]	30	√	√		
Fe-Cr-Co-Mo-Mn-C-B-Y [18]	12	√	√		√

combining with high strength and large ductility but also theoretical advances in the underlying deformation mechanisms at atomic scale.

Na Chen

Limei Xu

Yang Shao

Konstantinos Georgarakis

References

- [1] A. L. Greer, "Metallic glasses," *Science*, vol. 267, no. 5206, pp. 1947–1953, 1995.
- [2] A. Inoue, "Stabilization of metallic supercooled liquid and bulk amorphous alloys," *Acta Materialia*, vol. 48, no. 1, pp. 279–306, 2000.
- [3] W. L. Johnson, "Bulk glass-forming metallic alloys: science and technology," *MRS Bulletin*, vol. 24, no. 10, pp. 42–56, 1999.
- [4] W. H. Wang, C. Dong, and C. H. Shek, "Bulk metallic glasses," *Materials Science and Engineering R: Reports*, vol. 44, no. 2-3, pp. 45–90, 2004.
- [5] D. B. Miracle, "A structural model for metallic glasses," *Nature Materials*, vol. 3, no. 10, pp. 697–702, 2004.
- [6] H. W. Sheng, W. K. Luo, F. M. Alamgir, J. M. Bai, and E. Ma, "Atomic packing and short-to-medium-range order in metallic glasses," *Nature*, vol. 439, no. 7075, pp. 419–425, 2006.
- [7] A. Hirata, P. Guan, T. Fujita et al., "Direct observation of local atomic order in a metallic glass," *Nature Materials*, vol. 10, no. 1, pp. 28–33, 2011.
- [8] Y. Q. Cheng and E. Ma, "Atomic-level structure and structure-property relationship in metallic glasses," *Progress in Materials Science*, vol. 56, no. 4, pp. 379–473, 2011.
- [9] M. Marcus and D. Turnbull, "On the correlation between glass-forming tendency and liquidus temperature in metallic alloys," *Materials Science and Engineering*, vol. 23, no. 2-3, pp. 211–214, 1976.
- [10] H. W. Kui, A. L. Greer, and D. Turnbull, "Formation of bulk metallic-glass by fluxing," *Applied Physics Letters*, vol. 45, no. 6, pp. 615–616, 1984.
- [11] N. Chen, K. Yao, and F. Ruan, "Influence of flux treatment on the glass forming ability of Pd-Si binary alloys," *Journal of University of Science and Technology Beijing*, vol. 14, no. 1, pp. 4–7, 2007.
- [12] Z. P. Lu and C. T. Liu, "Role of minor alloying additions in formation of bulk metallic glasses: a review," *Journal of Materials Science*, vol. 39, no. 12, pp. 3965–3974, 2004.
- [13] W. H. Wang, "Roles of minor additions in formation and properties of bulk metallic glasses," *Progress in Materials Science*, vol. 52, no. 4, pp. 540–596, 2007.
- [14] N. Chen, L. Martin, D. V. Luzguine-Luzgin, and A. Inoue, "Role of alloying additions in glass formation and properties of bulk metallic glasses," *Materials*, vol. 3, no. 12, pp. 5320–5339, 2010.
- [15] A. L. Greer, Y. Q. Cheng, and E. Ma, "Shear bands in metallic glasses," *Materials Science and Engineering R: Reports*, vol. 74, no. 4, pp. 71–132, 2013.
- [16] A. Inoue and A. Takeuchi, "Recent development and application products of bulk glassy alloys," *Acta Materialia*, vol. 59, no. 6, pp. 2243–2267, 2011.
- [17] W. L. Johnson, "Bulk amorphous metal—an emerging engineering material," *JOM*, vol. 54, no. 3, pp. 40–43, 2002.
- [18] Z. P. Lu, C. T. Liu, J. R. Thompson, and W. D. Porter, "Structural amorphous steels," *Physical Review Letters*, vol. 92, no. 24, Article ID 245503, 2004.

Research Article

Investigation of Mechanical Properties and Plastic Deformation Behavior of $(\text{Ti}_{45}\text{Cu}_{40}\text{Zr}_{10}\text{Ni}_5)_{100-x}\text{Al}_x$ Metallic Glasses by Nanoindentation

Lanping Huang, Xuzhe Hu, TaoTao Guo, and Song Li

State Key Laboratory for Powder Metallurgy, Central South University, Changsha 410083, China

Correspondence should be addressed to Song Li; ls2011sl@csu.edu.cn

Received 21 February 2014; Accepted 1 July 2014; Published 17 July 2014

Academic Editor: Yang Shao

Copyright © 2014 Lanping Huang et al. This is an open access article distributed under the Creative Commons Attribution License, which permits unrestricted use, distribution, and reproduction in any medium, provided the original work is properly cited.

The effect of Al addition on mechanical properties and plastic deformation behavior of $(\text{Ti}_{45}\text{Cu}_{40}\text{Zr}_{10}\text{Ni}_5)_{100-x}\text{Al}_x$ ($x = 0, 2, 4, 6$ and 8) amorphous alloy ribbons have been investigated by nanoindentation. The hardness and elastic modulus do not simply increase with the increase of Al content. The alloy with 8 at.% Al exhibits the highest hardness and elastic modulus. The serrations or pop-in events are strongly dependent on the loading rate and alloy composition.

1. Introduction

Ever since the first report of Au-Si amorphous alloy obtained by rapid solidification in 1960 [1], metallic glass formation has been found in a variety of alloy systems by this technique [2–4]. Compared with their crystalline counterparts, metallic glasses exhibit unique mechanical, physical, and chemical properties [5–8]. However, the lack of any significant plastic deformation at room temperature limits their potential applications [9, 10]. Shear localization is considered to be the primary plastic deformation mechanism in metallic glasses [11, 12]. Therefore, mechanical properties and deformation of metallic glasses have been given more and more attention. As an important tool to study nanomechanical properties of various materials, nanoindentation has been widely used for exploring the mechanical response such as hardness and elastic modulus of metallic glasses because it allows considerably larger plastic deformation to be accumulated in quasi-brittle materials in a localized area around the indented regions [13–15].

In this work, mechanical response of a series of $(\text{Ti}_{45}\text{Cu}_{40}\text{Zr}_{10}\text{Ni}_5)_{100-x}\text{Al}_x$ ($x = 0, 2, 4, 6$, and 8) amorphous alloys subjected to nanoindentation tests has been systematically investigated based on the change of alloy composition and the applied loading rate. It is expected that

our work could provide insight into better understanding of the mechanical properties and deformation behavior of metallic glasses during nanoindentation.

2. Experimental

Multicomponent $(\text{Ti}_{45}\text{Cu}_{40}\text{Zr}_{10}\text{Ni}_5)_{100-x}\text{Al}_x$ ($x = 0, 2, 4, 6$, and 8) (all compositions in atomic percent) alloys were prepared by high purity raw materials by arc melting under Ti-gettered argon atmosphere. The alloy ribbons were fabricated using a single-roller melt spinning apparatus at a speed of 40 m/s. The amorphous nature of the as-synthesized specimen was examined by X-ray diffraction (XRD) using $\text{Cu-K}\alpha$ radiation and transmission electron microscopy (TEM). Thermal properties were investigated by a differential scanning calorimeter (DSC) at a heating rate of 0.17 K/s. Nanoindentation tests were conducted using an Ultra Nanoindentation tester with a Berkovich diamond tip. The indentations were performed in the load-control mode with maximum load of 30 mN at various loading rates of 0.5, 1, 2, 4, and 10 mN/s and a constant unloading of 0.33 mN/s. At least 5 indents were measured to verify the accuracy and scatter of the indentation data. The morphologies of the indents were characterized using atomic force microscopy (AFM).

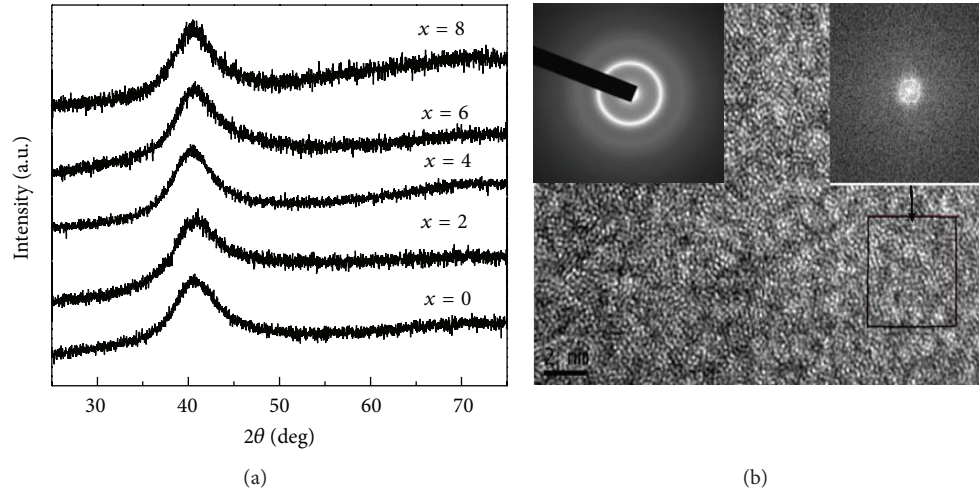


FIGURE 1: (a) XRD patterns of the as-quenched $(\text{Ti}_{45}\text{Cu}_{40}\text{Zr}_{10}\text{Ni}_5)_{100-x}\text{Al}_x$ ($x = 0, 2, 4, 6,$ and 8) alloy ribbons; (b) TEM micrograph and corresponding selected area diffraction (SEAD).

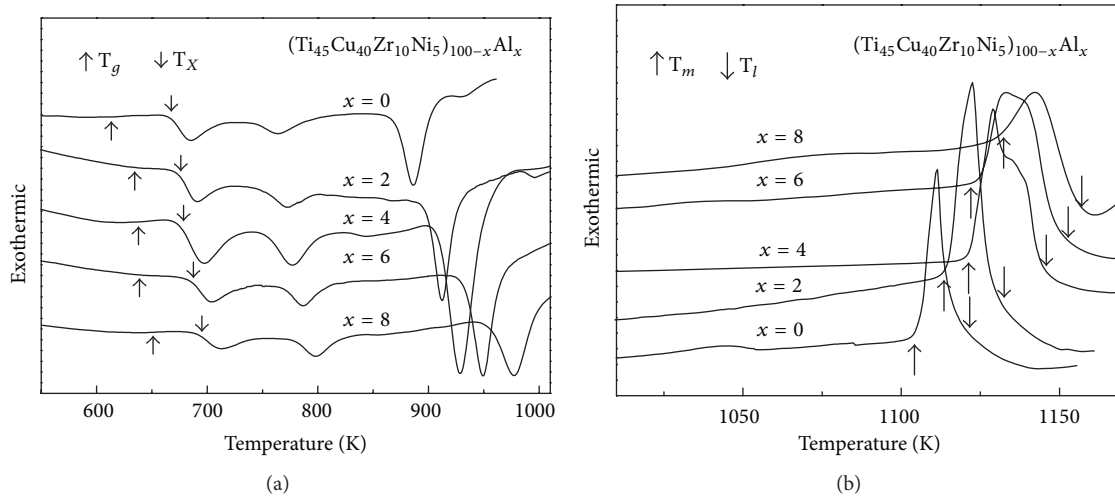


FIGURE 2: DSC curves of the as-quenched $(\text{Ti}_{45}\text{Cu}_{40}\text{Zr}_{10}\text{Ni}_5)_{100-x}\text{Al}_x$ ($x = 0, 2, 4, 6,$ and 8) alloy ribbons.

3. Result and Discussion

Figure 1 shows the XRD patterns of the as-quenched $(\text{Ti}_{45}\text{Cu}_{40}\text{Zr}_{10}\text{Ni}_5)_{100-x}\text{Al}_x$ ($x = 0, 2, 4, 6,$ and 8) alloy ribbons, together with the TEM image of the alloy with 2 at.% Al. As shown in Figure 1(a), only broad diffraction maxima can be seen without distinct sharp peak corresponding to crystalline phases, indicating the formation of a glassy phase in all ribbons. The TEM micrograph and corresponding selected area diffraction (SEAD) displaying diffuse halos for the alloy with 2 at.% Al are shown in Figure 1(b). It can be seen that there is no discernible contrast in the TEM bright field micrograph. This further confirms the amorphous nature of the alloy system and similar features are also observed for other alloy ribbons (not shown here).

Figure 2 indicates the DSC curves of the as-quenched $(\text{Ti}_{45}\text{Cu}_{40}\text{Zr}_{10}\text{Ni}_5)_{100-x}\text{Al}_x$ ($x = 0, 2, 4, 6,$ and 8) alloy ribbons. As shown in Figure 2(a), all alloy ribbons exhibit an endothermic characteristic of the glass transition followed

by three exothermic events indicating the successive step-wise transformations from the super-cooled liquid state to crystalline phases. The glass transition temperature (T_g) and onset crystallization temperature (T_x) steadily increase with the increase of Al content, while thermal stability is not obviously improved by Al addition. The melting behaviors of the $(\text{Ti}_{45}\text{Cu}_{40}\text{Zr}_{10}\text{Ni}_5)_{100-x}\text{Al}_x$ ($x = 0, 2, 4, 6,$ and 8) alloy ribbons are presented in Figure 2(b), where the melting temperature (T_m) and liquidus temperature (T_l) are marked by arrows. The T_m and T_l also increase, and the temperature range for the melting process becomes wider with increasing Al content from 0 to 8 at.%. This means that the composition of the alloys moves away from the pseudoeutectic composition.

Nanoindentation measurement was used to investigate the mechanical properties and plastic deformation behavior of the as-quenched $(\text{Ti}_{45}\text{Cu}_{40}\text{Zr}_{10}\text{Ni}_5)_{100-x}\text{Al}_x$ ($x = 0, 2, 4, 6,$ and 8) amorphous alloy ribbons. The hardness (H), elastic modulus (E), and Vickers hardness (HV) of the as-quenched $(\text{Ti}_{45}\text{Cu}_{40}\text{Zr}_{10}\text{Ni}_5)_{100-x}\text{Al}_x$ ($x = 0, 2, 4, 6,$ and 8) alloy ribbons,

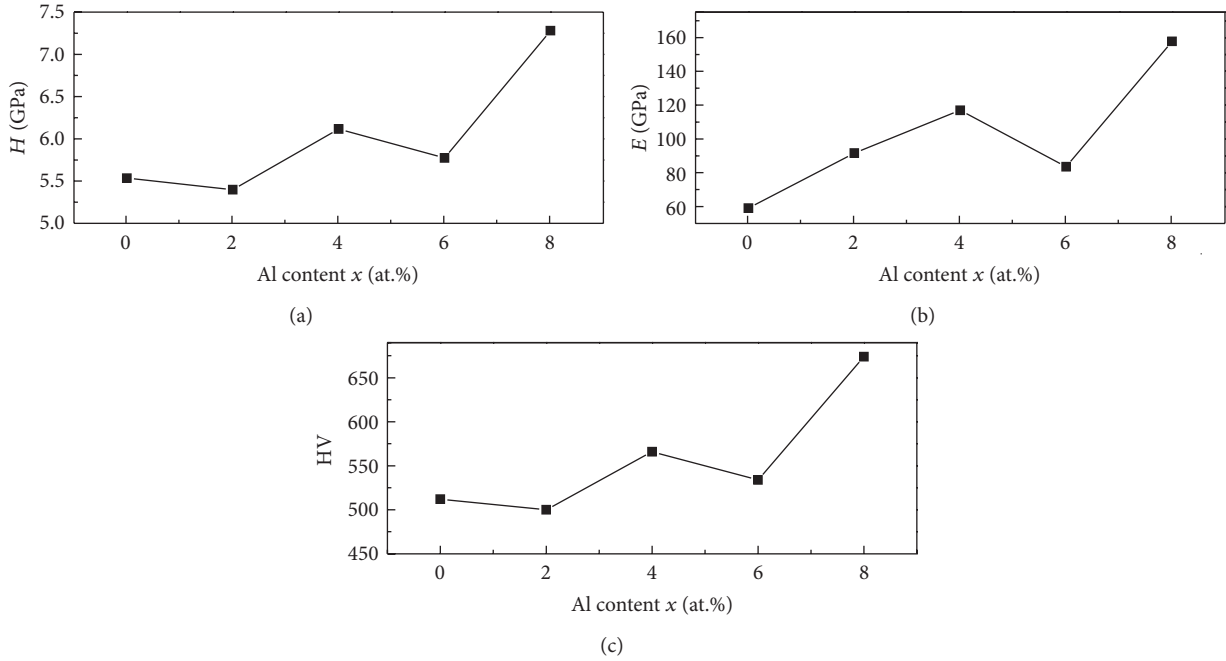


FIGURE 3: Hardness (H), elastic modulus (E), and Vickers hardness (HV) of the as-quenched $(\text{Ti}_{45}\text{Cu}_{40}\text{Zr}_{10}\text{Ni}_5)_{100-x}\text{Al}_x$ ($x = 0, 2, 4, 6,$ and 8) alloy ribbons.

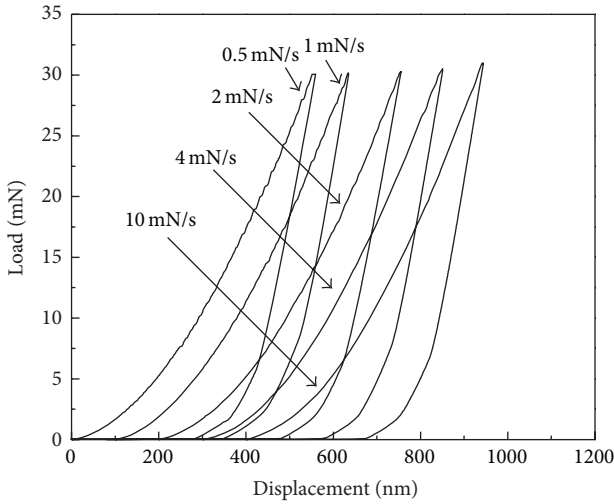


FIGURE 4: Load-displacement curves for the alloy with 2 at.% Al at the loading rates of 0.5, 1, 2, 4, and 10 mN/s.

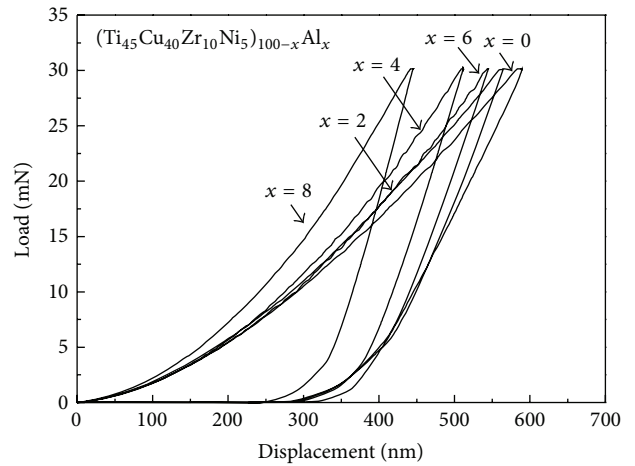


FIGURE 5: Load-displacement curves of the as-quenched $(\text{Ti}_{45}\text{Cu}_{40}\text{Zr}_{10}\text{Ni}_5)_{100-x}\text{Al}_x$ ($x = 0, 2, 4, 6,$ and 8) alloy ribbons at a loading rate of 2 mN/s.

obtained by Oliver-Pharr method, are shown in Figure 3. The E increases from 59 to 159 GPa for the increase of x from 0 to 8, but it does not exhibit a simply increasing trend with the increase of Al content. For H and HV, the minor addition of Al ($x = 2$) induces mechanical softening, manifested in a little decrease of H and HV shown in Figure 3. For other alloys with higher Al content, the H and HV exhibit a similar trend as E .

The effect of the loading rate on plastic deformation behavior of the as-quenched $(\text{Ti}_{45}\text{Cu}_{40}\text{Zr}_{10}\text{Ni}_5)_{100-x}\text{Al}_x$ ($x = 0, 2, 4, 6,$ and 8) amorphous alloy ribbons has been

investigated. As an example, Figure 4 shows the typical load-displacement curves for the alloy with 2 at.% Al at the loading rates of 0.5, 1, 2, 4, and 10 mN/s. For clarity, each successive curve is plotted with its displacement origin offset by 100 nm. As shown in Figure 4, the serration size increases with decreasing loading rate, and the largest serrated flow occurs at the lowest loading rate (0.5 mN/s), which is in agreement with the previous results [16–21]. The similar trend is also observed for other alloys. Figure 5 shows the typical load-displacement curves of the as-quenched $(\text{Ti}_{45}\text{Cu}_{40}\text{Zr}_{10}\text{Ni}_5)_{100-x}\text{Al}_x$ ($x = 0, 2, 4, 6,$ and 8) alloy ribbons at a loading rate of 2 mN/s.

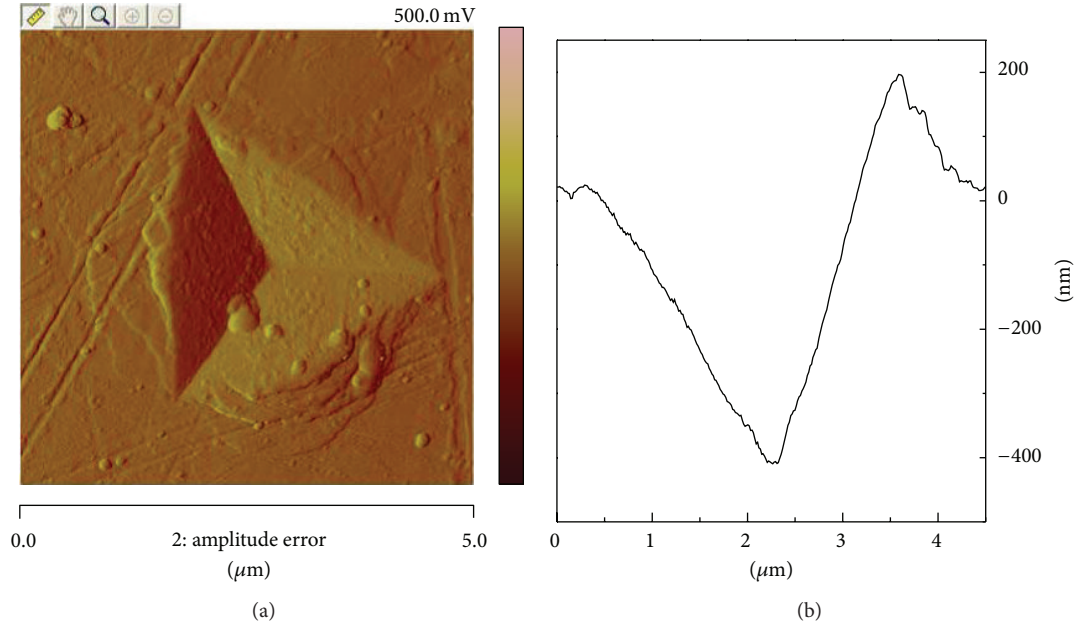


FIGURE 6: Typical surface deformation features and pileup through indentation of the alloy with 2 at.% Al obtained after nanoindentation.

It can be found from Figure 5 that the higher Al content alloy exhibits a higher slope indicating a higher hardness except for the alloy with 6 at.% Al, and the serrated flow is most pronounced in the load-displacement curve for the low Al content and Al-free alloys. The load-displacement curves gradually become smoother with the increase of Al content. At the highest Al content ($x = 8$), there is no obviously serrated flow. This suggests that the Al addition obviously influences the nucleation and propagation of shear bands. According to the previous work [22, 23], the increase of Al content promotes continuous formation and propagation of shear bands in $(\text{Ti}_{45}\text{Cu}_{40}\text{Zr}_{10}\text{Ni}_5)_{100-x}\text{Al}_x$ ($x = 0, 2, 4, 6,$ and 8) amorphous alloys, which decreases serration size and the interval between operations of two consecutive shear bands because Al may decrease the microyield stress of the amorphous alloy. Therefore, with the increase of Al content the serrations or pop-in events gradually disappear. To further characterize the localized plastic deformation behavior, AFM observation around indents has been performed. Figure 6 shows the typical surface deformation features and pileup through indentation of the alloy with 2 at.% Al obtained after nanoindentation. A number of partial circular patterned shear bands can be seen in the pileup region, and the pileup is discontinuous. This reveals that the plastic deformation occurs during nanoindentation.

4. Conclusions

Nanoindentation investigations of mechanical properties and plastic deformation behavior of $(\text{Ti}_{45}\text{Cu}_{40}\text{Zr}_{10}\text{Ni}_5)_{100-x}\text{Al}_x$ ($x = 0, 2, 4, 6,$ and 8) amorphous alloy ribbons have been conducted. The alloy with 8 at.% Al exhibits the highest hardness and elastic modulus, but the hardness and elastic modulus do not simply increase with the increase of Al

content. The currently studied metallic glasses exhibit typical localized plastic deformation during nanoindentation such as serrations or pop-in events. The increase of Al content retards the occurrence of the serrations obviously.

Conflict of Interests

The authors state that there is not conflict of interests regarding the publication of this paper.

Acknowledgments

The work was supported by Open Project Program of Shenzhen Key Laboratory of Special Functional Materials of China (Grant no. T0907) and Open-End Fund for the Valuable and Precision Instruments of Central South University (Grant no. CSUZC2013024 and Grant no. CSUZC2014032).

References

- [1] W. Klement, R. H. Willens, and P. Duwez, "Non-crystalline structure in solidified Gold-Silicon alloys," *Nature*, vol. 187, no. 4740, pp. 869–870, 1960.
- [2] A. L. Greer, "Metallic glasses," *Science*, vol. 267, no. 5206, pp. 1947–1953, 1995.
- [3] A. Inoue, "Stabilization of metallic supercooled liquid and bulk amorphous alloys," *Acta Materialia*, vol. 48, no. 1, pp. 279–306, 2000.
- [4] W. H. Wang, C. Dong, and C. H. Shek, "Bulk metallic glasses," *Materials Science and Engineering R: Reports*, vol. 44, no. 2-3, pp. 45–89, 2004.
- [5] W. Zhou, X. Lin, and J. F. Li, "Effects of Ag addition on crystallization, microstructure and mechanical properties of Zr-Cu-Ni-Al-Ag bulk metallic glasses," *Journal of Alloys and Compounds*, vol. 552, pp. 102–106, 2013.

- [6] G. R. Garrett, M. D. Demetriou, J. Chen, and W. L. Johnson, "Effect of microalloying on the toughness of metallic glasses," *Applied Physics Letters*, vol. 101, no. 24, Article ID 241913, 6 pages, 2012.
- [7] C. Qin, W. Zhang, K. Asami, N. Ohtsu, and A. Inoue, "Glass formation, corrosion behavior and mechanical properties of bulk glassy Cu-Hf-Ti-Nb alloys," *Acta Materialia*, vol. 53, no. 14, pp. 3903–3911, 2005.
- [8] J. Q. Wang, Y. H. Liu, S. Imhoff et al., "Enhance the thermal stability and glass forming ability of Al-based metallic glass by Ca minor-alloying," *Intermetallics*, vol. 29, pp. 35–40, 2012.
- [9] W. L. Johnson, "Bulk glass-forming metallic alloys: science and technology," *Materials Research Society Bulletin*, vol. 24, no. 10, pp. 42–56, 1999.
- [10] J. Eckert, J. Das, S. Pauly, and C. Duhamel, "Mechanical properties of bulk metallic glasses and composites," *Journal of Materials Research*, vol. 22, no. 2, pp. 285–301, 2007.
- [11] Z. F. Zhang, G. He, J. Eckert, and L. Schultz, "Fracture mechanisms in bulk metallic glassy materials," *Physical Review Letters*, vol. 91, Article ID 045505, 2003.
- [12] T. C. Hufnagel, C. Fan, R. T. Ott, J. Li, and S. Brennan, "Controlling shear band behavior in metallic glasses through microstructural design," *Intermetallics*, vol. 10, no. 11-12, pp. 1163–1166, 2002.
- [13] N. Li, L. Liu, K. C. Chan, Q. Chen, and J. Pan, "Deformation behavior and indentation size effect of Au₄₉Ag_{5.5}Pd_{2.3}Cu_{26.9}Si_{16.3} bulk metallic glass at elevated temperatures," *Intermetallics*, vol. 17, no. 4, pp. 227–230, 2009.
- [14] C. A. Schuh and T. G. Nieh, "A nanoindentation study of serrated flow in bulk metallic glasses," *Acta Materialia*, vol. 51, no. 1, pp. 87–99, 2003.
- [15] B. G. Yoo, K. W. Lee, and J. I. Jang, "Instrumented indentation of a Pd-based bulk metallic glass: constant loading-rate test vs constant strain-rate test," *Journal of Alloys and Compounds*, vol. 483, no. 1-2, pp. 136–138, 2009.
- [16] W. J. Wright, R. B. Schwarz, and W. D. Nix, "Localized heating during serrated plastic flow in bulk metallic glasses," *Materials Science and Engineering A*, vol. 319–321, pp. 229–232, 2001.
- [17] Y. I. Golovin, V. I. Ivolgin, V. A. Khonik, K. Kitagawa, and A. I. Tyurin, "Serrated plastic flow during nanoindentation of a bulk metallic glass," *Scripta Materialia*, vol. 45, no. 8, pp. 947–952, 2001.
- [18] B. Yang and T. G. Nieh, "Effect of the nanoindentation rate on the shear band formation in an Au-based bulk metallic glass," *Acta Materialia*, vol. 55, no. 1, pp. 295–300, 2007.
- [19] J. T. Kim, S. H. Hong, C. H. Lee et al., "Role of strontium addition on the phase transition of lanthanum copper oxide from K₂NiF₄ to perovskite structure," *Journal of Alloys and Compounds*, vol. 440, no. 1-2, pp. 62–68, 2007.
- [20] J. W. Qiao, Z. Wang, H. J. Yang, M. Li, W. Liang, and B. S. Xu, "Exponential decay of shearing stress during jerky flows in a Zr-based bulk metallic glass," *AIP Advances*, vol. 3, no. 3, Article ID 032105, 2013.
- [21] L. Cheng, Z. M. Jiao, S. G. Ma, J. W. Qiao, and Z. H. Wang, "Serrated flow behaviors of a Zr-based bulk metallic glass by nanoindentation," *Journal of Applied Physics*, vol. 115, Article ID 084907, 2014.
- [22] B. C. Wei, T. H. Zhang, W. H. Li, Y. F. Sun, Y. Yu, and Y. R. Wang, "Serrated plastic flow during nanoindentation in Nd-based bulk metallic glasses," *Intermetallics*, vol. 12, no. 10-11, pp. 1239–1243, 2004.
- [23] K. M. Liua, H. T. Zhou, B. Yang, D. P. Lu, and A. Atrens, "Influence of Si on glass forming ability and properties of the bulk amorphous alloy Mg₆₀Cu₃₀Y₁₀," *Materials Science and Engineering: A*, vol. 527, no. 29-30, pp. 7475–7479, 2010.

Research Article

Formation and Mechanical Properties of Pd-Si Binary Bulk Metallic Glasses

Na Chen, Hongxia Zhang, and Ke-Fu Yao

School of Materials Science and Engineering, Tsinghua University, Beijing 100084, China

Correspondence should be addressed to Na Chen; chennadm@mail.tsinghua.edu.cn and Ke-Fu Yao; kfyao@tsinghua.edu.cn

Received 17 March 2014; Accepted 7 May 2014; Published 28 May 2014

Academic Editor: Yang Shao

Copyright © 2014 Na Chen et al. This is an open access article distributed under the Creative Commons Attribution License, which permits unrestricted use, distribution, and reproduction in any medium, provided the original work is properly cited.

Glassy spherical samples in the diameters up to 10 mm were produced in a binary Pd-Si alloy system. These Pd-Si bulk metallic glasses (BMGs) combine high strength of about 1600 MPa and superplasticity of over 70% together. In addition to abundant micrometer-scale shear bands, 10–20 nanometer-sized shear bands were also observed on the side surface of the deformed sample. The excellent ductility shown by the Pd-Si BMGs is suggested to arise from the nanoscale structural inhomogeneity.

1. Introduction

The formation of the first metallic glass (MG) in a binary Au-Si system has spurred intensive interest in the fundamental understanding of glass formation and structure-property relationship [1–5]. In particular, the unique mechanical response of bulk metallic glasses (BMGs) makes them more attractive in certain application fields than their crystalline counterparts [6–10]. Based on a “confusion principle,” BMGs are usually formed in multicomponent alloy systems [2–4]. However, some binary alloy systems such as Cu-Zr, Pd-Si, and Cu-Hf as well as Ni-Nb alloys exhibit exceptionally high glass-forming ability (GFA) so that BMGs can be produced from these alloys [11–15]. In addition, these binary BMGs show a combination of both high strength and large ductility [8, 9]. Due to their simple compositions, the binary alloys are more prone to crystallization than the multicomponent alloys, posing extreme difficulties in producing BMGs with sizes larger than 2 mm [11–14]. In this paper, Pd-Si BMGs in the diameter up to 10 mm were produced, which are the largest binary BMGs reported so far. On the basis of the nanoindentation and uniaxial compression tests, the mechanical properties of Pd₈₁Si₁₉BMG alloys have been studied.

2. Experimental Procedure

Ingots of Pd₈₁Si₁₉alloys were prepared by melting the mixtures of Pd and Si with over 99.99 wt% purities in an argon

atmosphere. Pd₈₁Si₁₉ingots were continuously purified by the fluxing medium including B₂O₃ in a quartz tube located in a stove with a constant temperature of 1423 K till glassy alloys were obtained. During this process, the quartz tube was taken out of the stove and cooled under air every 30 minutes in order to promote the fluxing effect. The structure of the glassy alloys was examined by X-ray diffractometry (XRD) with monochromatic CuK_α radiation. The elastic moduli of the Pd₈₁Si₁₉ BMGs, such as Young’s modulus and the shear modulus, were obtained by the ultrasonic measurements. The microstructure of the samples was observed by transmission electron microscope (TEM) using a JEM 120EX (JEOL) and a JEM 2010F high resolution transmission electron microscope (HRTEM) with an accelerating voltage of 200 KV. The thin foil specimens for TEM observation were prepared by a standard twin-jet electropolishing method. Nanoindentation tests were performed at a strain rate of 0.5 s⁻¹ by the Nano Indenter indentation instrument of MTS with Berkovich tip. Uniaxial compression tests were measured by an Instron testing machine.

3. Results and Discussions

Figure 1 shows the XRD patterns of Pd-Si binary alloys. The diameter of the spherical Pd₈₁Si₁₉ sample is about 10 mm while the diameter of the Pd₈₀Si₂₀ glassy ball is around 8 mm. Except the broad diffraction peaks, no distinctive sharp diffraction peak resulted by crystalline phases can be

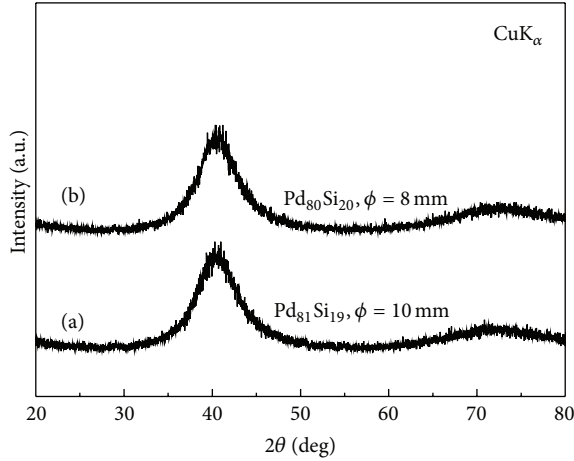


FIGURE 1: XRD patterns of Pd-Si alloys: (a) $\text{Pd}_{81}\text{Si}_{19}$ BMG with a diameter up to 10 mm and (b) $\text{Pd}_{80}\text{Si}_{20}$ BMG with a diameter up to 8 mm.

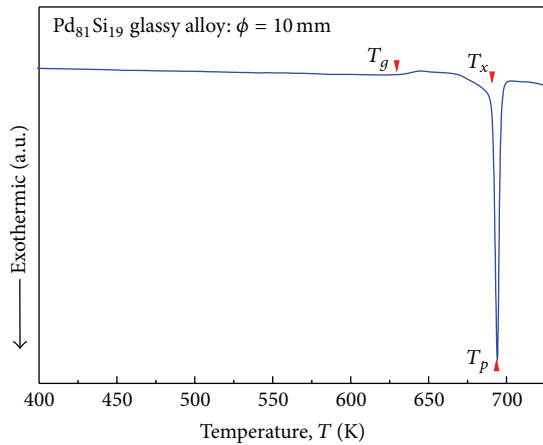


FIGURE 2: DSC curve of the $\text{Pd}_{81}\text{Si}_{19}$ BMG with a diameter of 10 mm.

observed, indicating that glassy structure was formed in both samples.

Figure 2 presents the DSC curve of the $\text{Pd}_{81}\text{Si}_{19}$ BMG with the near eutectic composition ($\text{Pd}_{82.8}\text{Si}_{17.2}$). The glass transition temperature (T_g), initial crystallization temperature (T_x), and the peak crystallization temperature (T_p) are determined to be 629 K, 691 K, and 693 K, respectively. Thus, the supercooled liquid region ΔT defined by the difference between T_g and T_x ($\Delta T = T_x - T_g$) can be obtained to be as large as 62 K. Meanwhile, the DSC trace shows one distinct exothermic peak corresponding to the subsequent devitrification starting at T_x .

Figure 3 shows the structure of the $\text{Pd}_{81}\text{Si}_{19}$ BMG, which is typical for amorphous materials. No distinct evidence of crystalline diffraction spots or thin rings can be found in the selected-area electron diffraction (SAED) pattern shown in Figure 3(b). This further confirms the samples' amorphous structure. The high resolution transmission electron microscope (HRTEM) image evidences the structural inhomogeneity of the $\text{Pd}_{81}\text{Si}_{19}$ BMGs as shown in Figure 3(c).

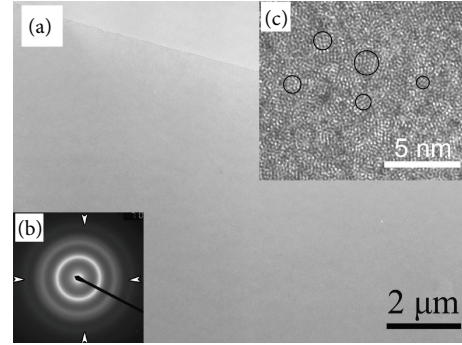


FIGURE 3: The microstructure of the $\text{Pd}_{81}\text{Si}_{19}$ BMG: (a) a bright field (BF) image, (b) a selected-area electron diffraction (SAED) pattern, and (c) a HRTEM image.

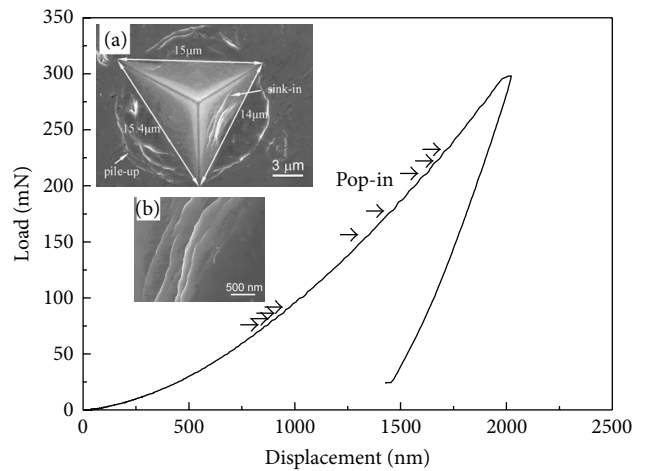


FIGURE 4: Nanoindentation load-displacement curve of the $\text{Pd}_{81}\text{Si}_{19}$ BMG with the inset: (a) SEM of indentation and (b) the enlargement of sinking-in.

For instance, the medium-range order (MRO) clusters less than 2 nm are frequently observed as indicated by the black circles, corresponding to the outer diffraction ring marked with white arrows shown in Figure 3(b).

Figure 4 shows the load-displacement p - h curve of the nanoindentation test for the $\text{Pd}_{81}\text{Si}_{19}$ BMG at a strain rate of 0.05 s^{-1} . A few small discrete pop-in events can be observed during the load process, indicating the operation of individual shear bands as reported in Zr-based, Ni-based, and other amorphous alloys [16–18]. The piling-up is observed as shown in the upper inset of Figure 4(a). Strikingly, the sinking-in phenomena also appear near the indenter, which are more pronounced for the strain-hardening or the non-strain-hardening materials with a low value of E/Y (where E is elastic modulus and Y is the yielding strength) shown in Figure 4(b) [19]. By using the ultrasonic measurements, the elastic moduli of Young's modulus, the shear modulus, and Poisson's ratio were obtained to be 94.53 GPa, 33.43 GPa, and 0.414, respectively. The yielding strength is about 1600 MPa estimated from the compression test. Then the E/Y can be calculated to be 59, a relatively low value compared

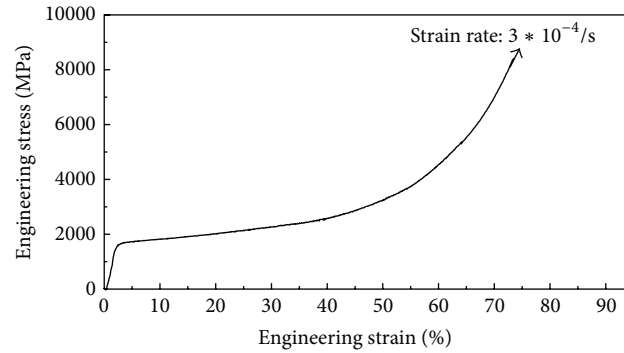


FIGURE 5: The compressive stress-strain curve of the $\text{Pd}_{81}\text{Si}_{19}$ BMG deformed at room temperature.

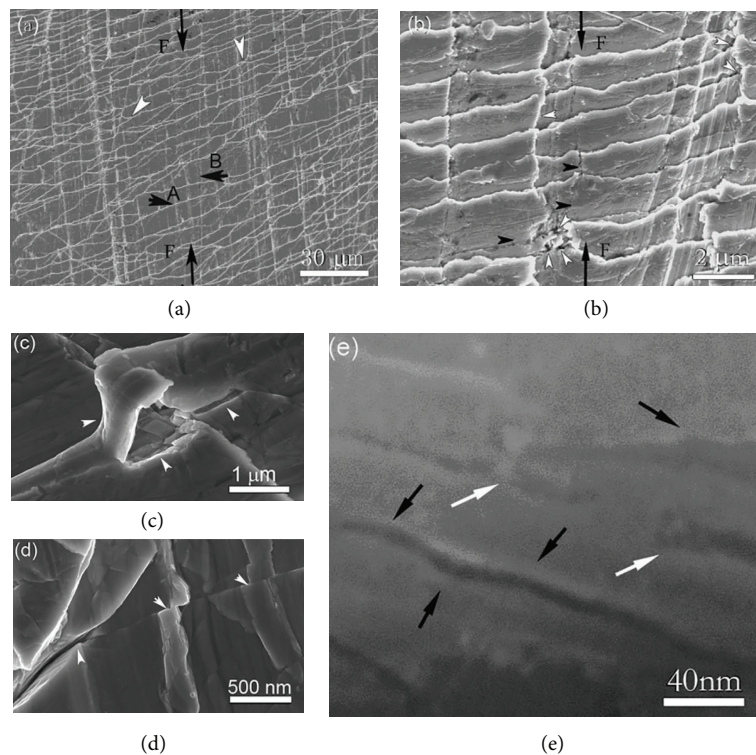


FIGURE 6: SEM side-view images of a deformed $\text{Pd}_{81}\text{Si}_{19}$ BMG specimen with a plastic engineering strain over 70% (a) $\times 2$ K, (b) $\times 20$ K, (c) $\times 100$ K, (d) $\times 50$ K, and (e) $\times 1000$ K.

with the corresponding crystalline materials. MGs usually show higher yielding strength and lower elastic modulus compared with their crystalline counterparts, leading to relatively low values of E/Y . MGs are thus expected to exhibit the sinking-in phenomena. However, most of the studies on the nanoindentation behaviors of MGs scarcely reported the presence of the sinking-in phenomena [16–18].

Figure 5 shows the compression curve of the $\text{Pd}_{81}\text{Si}_{19}$ BMG, showing a unique combination of a high strength of about 1600 MPa and a large plasticity of over 70%. The SEM side-view images of the compression specimen at a plastic engineering strain of $\sim 70\%$ are shown in Figure 6(a). Different from most monolithic BMGs usually undergoing inhomogeneous plasticity and exhibiting poor ductility

($<1\%$) at room temperature, quite uniform multiple shear bands are observed with an interspace ranging from 1 to $10\ \mu\text{m}$. Moreover, these shear bands branch and intersect as marked with white arrows. Meanwhile, many small steps of about 50–100 nm in size are formed along the shear bands (see Figures 6(a) and 6(b)). This indicates that the propagation of shear bands could be blocked, resulting in deflection, bifurcation, and branching. The macroscopic morphology of twisted shear bands is thus rough-and-tumble. In addition, the shear bands can be mainly divided into two types marked with black arrows shown in Figure 6(a): A type at an orientation of $\sim 70^\circ$ with respect to the compression direction and B type nearly parallel to the compression direction. Many A type shear

bands are with angles of $35^\circ \sim 50^\circ$ to the loading axis. It is accepted that the macroscopic plasticity arises from the accumulation of local shear deformation originating from individual shear bands. So the total ductility increases with increasing the number of shear bands [20]. At a higher magnification image shown in Figure 6(b), voids marked by white arrows can be seen. Moreover, the initiation and propagation of the crack are also observed as marked by black arrows in Figure 6(b). Liu and coworkers reported that the formation of voids and cracks was induced by the tensile stress arising from the dilation and coalescence of the free volume [21]. The crack does not propagate along the shear bands but is hindered by the intersecting shear bands as shown in Figure 6(c). However, the intersecting shear bands pile up in Figure 6(d), exhibiting a softening behavior accompanied by microvoids formation.

The high resolution SEM image shows the morphology of microshear bands appearing between the main shear bands shown in Figure 6(e). Many kinks, deflection, and ledges marked by black arrows can be found along the shear bands. The heights of the ledges or kinks are about 10 nm or less. The interspace of these nanoscale shear bands is about 30–50 nm. As indicated by the white arrows in Figure 6(e), the propagation of microshear bands can be locally arrested and the induced new shear bands can be observed ahead.

The nanoscale structural inhomogeneity in $\text{Pd}_{81}\text{Si}_{19}$ is suggested to account for its large plasticity. These MRO clusters could function as a reinforcing source to effectively hinder the further propagation of the matured shear bands and promote formation of new shear bands [22, 23]. Cao et al. also reported that strain hardening occurred in Cu-Zr-Ti metallic glass due to phase separation-induced inhomogeneity during the cold rolling process [24]. This also indicates that the structural inhomogeneity could help generate multiple shear bands contributing to large plasticity. Thus, designing a glass-forming alloy with nanoscale structural inhomogeneity could endow this alloy with a unique combination of high strength and large ductility.

4. Conclusion

$\text{Pd}_{81}\text{Si}_{19}$ binary BMGs were prepared in shape of spheres with diameters up to 10 mm. The supercooled liquid region ΔT of the $\text{Pd}_{91}\text{Si}_{19}$ BMG is 62 K, indicating that the $\text{Pd}_{81}\text{Si}_{19}$ alloys possess high thermal stability and good glass-forming ability. Both piling-up and sinking-in phenomena occurred during the nanoindentation tests, demonstrating a possible strain-hardening deformation mechanism. The uniaxial compression tests proved that $\text{Pd}_{81}\text{Si}_{19}$ glassy alloys exhibit the superductility with a compressive plastic strain over 70%. Abundant shear bands were formed during deforming process, which is attributed to the intrinsically structural inhomogeneity.

Conflict of Interests

The authors declare that there is no conflict of interests regarding the publication of this paper.

Acknowledgments

This work is sponsored by Specialized Research Fund for the Doctoral Program of Higher Education, The National Science Foundation of China, and The Ministry of Science and Technology of China.

References

- [1] W. Klement, R. H. Willens, and P. Duwez, "Non-crystalline structure in solidified gold-silicon alloys," *Nature*, vol. 187, no. 4740, pp. 869–870, 1960.
- [2] A. L. Greer, "Metallic glasses," *Science*, vol. 267, no. 5206, pp. 1947–1953, 1995.
- [3] W. L. Johnson, "Bulk glass-forming metallic alloys: science and technology," *MRS Bulletin*, vol. 24, no. 10, pp. 42–56, 1999.
- [4] A. Inoue, "Stabilization of metallic supercooled liquid and bulk amorphous alloys," *Acta Materialia*, vol. 48, no. 1, pp. 279–306, 2000.
- [5] W.-H. Wang, C. Dong, and C. H. Shek, "Bulk metallic glasses," *Materials Science and Engineering R: Reports*, vol. 44, no. 2–3, pp. 45–89, 2004.
- [6] J. Schroers and W. L. Johnson, "Ductile bulk metallic glass," *Physical Review Letters*, vol. 93, no. 25, Article ID 255506, 2004.
- [7] J. Das, M. B. Tang, K. B. Kim et al., "'Work-hardenable' ductile bulk metallic glass," *Physical Review Letters*, vol. 94, no. 20, Article ID 205501, 2005.
- [8] A. Inoue, W. Zhang, T. Tsurui, A. R. Yavari, and A. L. Greer, "Unusual room-temperature compressive plasticity in nanocrystal-toughened bulk copper-zirconium glass," *Philosophical Magazine Letters*, vol. 85, no. 5, pp. 221–237, 2005.
- [9] K.-F. Yao, F. Ruan, Y. Q. Yang, and N. Chen, "Superductile bulk metallic glass," *Applied Physics Letters*, vol. 88, no. 12, Article ID 122106, 2006.
- [10] Y. H. Liu, G. Wang, R. J. Wang, D. Q. Zhao, M. X. Pan, and W. H. Wang, "Super plastic bulk metallic glasses at room temperature," *Science*, vol. 315, no. 5817, pp. 1385–1388, 2007.
- [11] D. Wang, Y. Li, B. B. Sun, M. L. Sui, K. Lu, and E. Ma, "Bulk metallic glass formation in the binary Cu-Zr system," *Applied Physics Letters*, vol. 84, no. 20, pp. 4029–4031, 2004.
- [12] D. Xu, B. Lohwongwatana, G. Duan, W. L. Johnson, and C. Garland, "Bulk metallic glass formation in binary Cu-rich alloy series— $\text{Cu}_{100-x}\text{Zr}_x$ ($x = 34, 36, 38.2, 40$ at.%) and mechanical properties of bulk $\text{Cu}_{64}\text{Zr}_{36}$ glass," *Acta Materialia*, vol. 52, no. 9, pp. 2621–2624, 2004.
- [13] L. Xia, D. Ding, S. T. Shan, and Y. D. Dong, "The glass forming ability of Cu-rich Cu-Hf binary alloys," *Journal of Physics: Condensed Matter*, vol. 18, no. 15, article 3543, 2006.
- [14] L. Xia, W. H. Li, S. S. Fang, B. C. Wei, and Y. D. Dong, "Binary Ni-Nb bulk metallic glasses," *Journal of Applied Physics*, vol. 99, no. 2, Article ID 026103, 2006.
- [15] N. Chen, Y. Li, and K.-F. Yao, "Thermal stability and fragility of Pd-Si binary bulk metallic glasses," *Journal of Alloys and Compounds*, vol. 504, supplement 1, pp. S211–S214, 2010.
- [16] C. A. Schuh and T. G. Nieh, "A nanoindentation study of serrated flow in bulk metallic glasses," *Acta Materialia*, vol. 51, no. 1, pp. 87–99, 2003.
- [17] J. G. Wang, B. W. Choi, T. G. Nieh, and C. T. Liu, "Crystallization and nanoindentation behavior of a bulk Zr-Al-Ti-Cu-Ni amorphous alloy," *Journal of Materials Research*, vol. 15, no. 3, pp. 798–807, 2000.

- [18] A. L. Greer, A. Castellero, S. V. Madge, I. T. Walker, and J. R. Wilde, "Nanoindentation studies of shear banding in fully amorphous and partially devitrified metallic alloys," *Materials Science and Engineering A*, vol. 375–377, no. 1-2, pp. 1182–1185, 2004.
- [19] A. C. Fischer-Cripps, *Nanoindentation*, edited by F. F. Ling, Springer, New York, NY, USA, 2002.
- [20] H. Bei, S. Xie, and E. P. George, "Softening caused by profuse shear banding in a bulk metallic glass," *Physical Review Letters*, vol. 96, no. 10, Article ID 105503, 2006.
- [21] L. F. Liu, L. H. Dai, Y. L. Bai, B. C. Wei, and J. Eckert, "Behavior of multiple shear bands in Zr-based bulk metallic glass," *Materials Chemistry and Physics*, vol. 93, no. 1, pp. 174–177, 2005.
- [22] K. L. Lee and H. W. Kui, "Phase separation in undercooled molten Pd₈₀Si₂₀: part I," *Journal of Materials Research*, vol. 14, no. 9, pp. 3653–3662, 1999.
- [23] S. Y. Hong, W. H. Guo, and H. W. Kui, "Metastable liquid miscibility gap in Pd–Si and its glass-forming ability: part III," *Journal of Materials Research*, vol. 14, no. 9, pp. 3668–3672, 1999.
- [24] Q. Cao, J. Li, Y. Zhou, and J. Jiang, "Mechanically driven phase separation and corresponding microhardness change in Cu₆₀Zr₂₀Ti₂₀ bulk metallic glass," *Applied Physics Letters*, vol. 86, no. 8, Article ID 081913, 2005.

Research Article

Amorphous Alloy: Promising Precursor to Form Nanoflowerpot

Guo Lan, Zhiqiang Xie, Zhenwei Huang, Shengchen Yang, Xuhai Zhang, Yuqiao Zeng, and Jianqing Jiang

Jiangsu Key Laboratory of Advanced Metallic Materials, School of Materials Science and Engineering, Southeast University, Nanjing 211189, China

Correspondence should be addressed to Yuqiao Zeng; zyuqiao@hotmail.com

Received 7 March 2014; Accepted 23 April 2014; Published 20 May 2014

Academic Editor: Na Chen

Copyright © 2014 Guo Lan et al. This is an open access article distributed under the Creative Commons Attribution License, which permits unrestricted use, distribution, and reproduction in any medium, provided the original work is properly cited.

Nanoporous copper is fabricated by dealloying the amorphous Ti_2Cu alloy in 0.03 M HF electrolyte. The pore and ligament sizes of the nanoporous copper can be readily tailored by controlling the dealloying time. The as-prepared nanoporous copper provides fine and uniform nanoflowerpots to grow highly dispersed Au nanoflowers. The blooming Au nanoflowers in the nanoporous copper flowerpots exhibit both high catalytic activity and stability towards the oxidation of glucose, indicating that the amorphous alloys are ideal precursors to form nanoflowerpot which can grow functional nanoflowers.

1. Backgrounds

Owing to the unique combination of physical, chemical, and mechanical properties, amorphous alloys have been posed as promising new materials for structural and functional utilizations [1, 2]. One of the most attractive applications is to use the amorphous alloys in nanotechnology. If the amorphous alloy is in a glassy state, the supercooled liquid region where the Newton's flow can take place may provide fascinating fabrication capability for the alloys. Nanorods, nanobars, and even micogears have been successfully prepared by nanoimprinting in the supercooled liquid region of Zr-based and Pt-based amorphous alloys [3, 4]. However, the amorphous alloys which have large supercooled liquid region are quite limited. Dealloying, on the other hand, can be performed on most of the amorphous alloys to form uniform nanostructure, no matter the alloy exhibits supercooled liquid region or not. During dealloying, the less noble elements are selectively dissolved and noble element keeps self-assembling through surface diffusion, leaving behind a bicontinuous nanoporous (NP) structure [5]. Usually, dealloying is applied on crystalline alloys composed by a single phase, such as intermetallic compounds or solid solutions, to form NP metals which have various functional applications in catalysis, chemical sensors, and electrochemistry [6–9]. Recently, there are some attempts to form nanoporous alloy

by dealloying amorphous alloys and the results show that the nanoporous structure obtained by dealloying amorphous alloy was finer and more uniform than that obtained by dealloying crystalline alloys. Therefore, there are intensive interests in the catalytic, thermal, and optical applications of the NP materials prepared by dealloying amorphous alloys. For instance, Yu et al. synthesized NPPd by electrochemically dealloying the $Pd_{30}Ni_{50}P_{20}$ amorphous alloy [10] and Lang et al. prepared NPAu by dealloying the Au-based amorphous alloy [11]. These NP materials exhibited high catalytic activity towards the oxidation of formic acid. Luo et al. obtained NP copper (NPC) by dealloying AlCuMg amorphous alloys. The NPC had extremely high specific surface area and could be used as low-temperature heat exchanger [12]. However, to our knowledge, there is no report on growing functional nanoflowers on the fine and uniform NP structures which are prepared by dealloying amorphous alloys.

In this study, we use Ti_2Cu amorphous alloy as the dealloying precursor to form “nanoflowerpot” to grow Au nanoflowers. Au in a nanoarchitecture form, such as NPAu, Au nanoflower, and Au nanoparticle, is an ideal material for enzyme-free electrochemical glucose sensor due to the high catalytic activity towards the oxidation of glucose [13, 14]. However, most of the Au nanomaterials suffer from the structure degradation [15]. For instance, nanopores and ligaments in NPAu will get coarsened and finally lose the

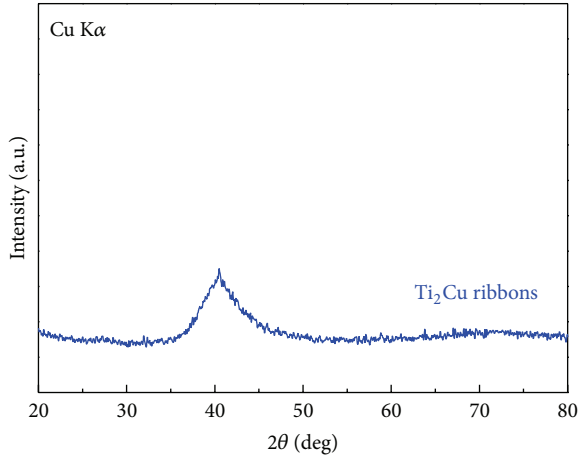


FIGURE 1: XRD pattern of the as-prepared Ti_2Cu ribbon sample.

catalytic activity during catalysis. It is expected that when NPC is used as the flowerpots to grow Au nanoflowers, that NPC dealloyed from amorphous alloy can provide homogenous dispersed growing sites for Au and stabilize the catalytic activity of the Au nanoflowers.

2. Experimental Methods

The Ti_2Cu amorphous alloy ribbon was prepared by arc melting Ti and Cu metals in a high-purity argon gas atmosphere, followed by melt spinning with a copper wheel velocity of about 40 ms^{-1} . The as-prepared amorphous ribbon is about 20 μm in thickness and 1 mm in width. The XRD pattern of the ribbon was recorded using an X-ray diffractometer with Cu K α radiation.

NPC samples are fabricated by selective etching of the Ti_2Cu amorphous ribbons in 0.03 M HF solutions. The dealloyed samples were firstly rinsed in pure water more than three times to remove the residual chemical substances and then were dried by freeze drier. With the aim of growing Au nanoflowers with tunable size, the dried NPC was immersed into a 0.5 mM HAuCl_4 solution in a three-neck flask at 0°C under Ar-protected magnetic stirring conditions.

The microstructures of the NPC as well as the NPC-G were observed by field-emission scanning electron microscope (SEM) and the compositions were characterized by energy dispersive X-ray spectrometer (EDS). The electrochemical performance of the NPC-G towards the oxidation of d-glucose is tested by electrochemical workstation CHI760D, where the NPC-G was used as the working electrode, saturated calomel electrode was used as a reference electrode, and a Pt foil was used as the counter electrode. The electrolyte is mixed with 0.01 M PBS and 50 mM glucose.

3. Results and Discussion

The XRD pattern of the ribbon in Figure 1 shows only a broad diffraction maximum without any observable crystalline peaks, demonstrating the formation of a homogenous amorphous structure in the ribbon sample.

TABLE 1: Chemical compositions of the NPC samples test by EDS.

Sample number	Cu (at%)	Ti (at%)
Amorphous ribbon	33.3	66.7
NPC number 1	85.3	14.7
NPC number 2	99.0	1.0
NPC number 3	99.5	0.5

TABLE 2: Chemical compositions of the NPC-G samples test by EDS.

Sample number	Au (at%)	Cu (at%)
NPC-G number 1	87.2	12.8
NPC-G number 2	95.9	4.1
NPC-G number 3	96.9	3.1

When the Ti_2Cu amorphous alloy is used as the precursor, the morphology development with the dealloying time is observed by SEM and the corresponding images are shown in Figure 2. Three-dimensional, interpenetrating ligament-channel nanoporous structure can be seen after 1 h of etching (Figure 2(a)). The ligaments are in a size ranging within 50–100 nm and the nanopores are about 5–20 nm. 10 h of etching leads to the formation of a fine continuous nanoporous structure. The ligaments are about 50–100 nm in size and the pores are in a bimodal distribution; that is, small pores are about 5 nm and large pores are about 15 nm. After 96 h of dealloying, ligaments increase up to about 200–500 nm and collapse occurs in many areas, resulting in the formation of large pores (100–200 nm). Visible nanoporous structure coarsening can be seen with the increase of dealloying time, indicating that the nanoflowerpot size can be readily tailored by controlling the dealloying time.

The chemical compositions of the dealloyed samples are measured by EDS and the results are summarized in Table 1. The Ti content first decreases from 66.7 at% to 14.7 at% after 1 h of dealloying, then goes down to 1.0 at% after 10 h of dealloying. Finally, it decreases to 0.5 at% after 96 h of corrosion. The gradually decrease of the Ti content and the coarsening of the NPC structure with the dealloying time suggest that the selective dissolving of Ti and the uphill diffusion of Cu carry through simultaneously the whole dealloying process.

Due to the fine and uniform structure, the NPC prepared by dealloying the Ti_2Cu amorphous alloys for 10 h was chosen as the flowerpot to grow Au flowers. The NPC was immersed into a 0.5 mM HAuCl_4 solution for 20, 40, and 60 min and the samples are named as NPC-G 1 number, NPC-G 2 number, and NPC-G 3 number, respectively. The SEM images of the NPC-G samples are shown in Figure 3 and the corresponding EDS results are summarized in Table 2. As shown in Figures 3(a) and 3(b), after 20 min of immersion, original bicontinuous nanoporous structure can barely be seen. Highly dispersed Au flowers with a size of 200–300 nm appear. The EDS results show that the sample contains 87.24 at% of Au, indicating the formation of NPC-G structure. After 40 min of immersion, a large number of Au nanoflowers with a size of about 500 nm “open” (Figure 3(c)). The flowers

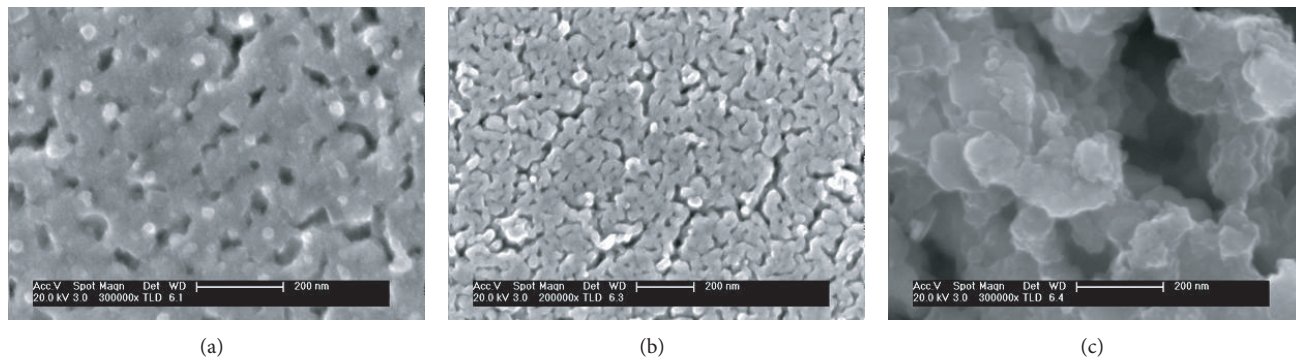


FIGURE 2: SEM images of NPC 1 number (a), NPC 2 number (b), and NPC 3 number (c).

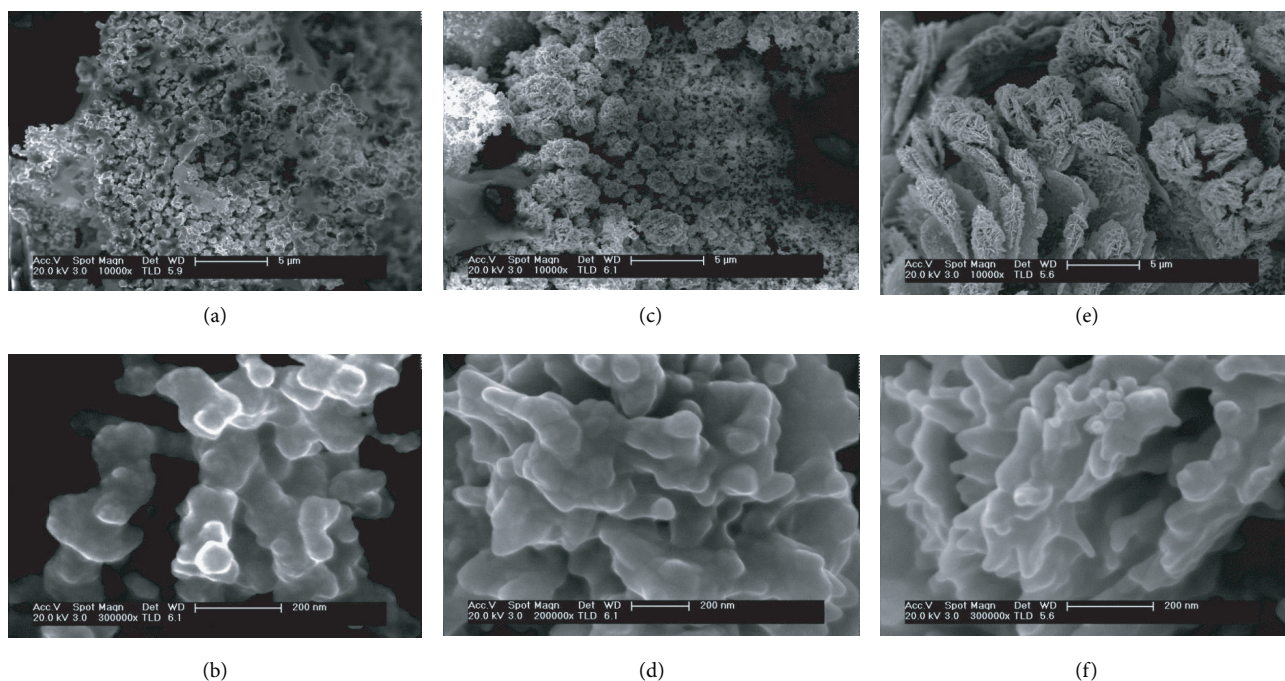


FIGURE 3: SEM images of NPC-G 1 number ((a), (b)), NPC-G 2 number ((c), (d)), and NPC-G 3 number ((e), (f)).

are composed by small Au nanoparticles with a size ranging within 100–150 nm (Figure 3(d)). The further increase of immersion time leads to a slight increase of Au content to 96.88 at% and dramatic growth of the Au flowers. As can be seen in Figure 3(e), the flowers are about 5 μm in diameter. The detailed morphology observation (Figure 3(f)) shows that the petals are still made by Au nanoparticles, indicating that the growth mechanism of Au is the same as that in NPC-G 2 number. Thus, the planting of Au nanoflowers on NPC may be divided into two steps: seeding and growing. Parts of the Cu atoms on the NPC surface are firstly replaced by Au according to the replacement reaction: $3\text{Cu} + 2\text{HAuCl}_4 = 3\text{CuCl}_2 + 2\text{HCl} + 2\text{Au}$. As the reaction time increases, all the Cu atoms on the surface of the NPC are replaced. However, the rapid formation of nanoporous Au provides the Au atoms high surface energy, which may drive the diffusion of Au towards an up-hill way. As a consequence, Au nanoparticles

can form. Due to the Ostwald Ripening, the nanoparticles agglomerate, making the flower growing and open. Due to the high porosity of the NPC formed by dealloying amorphous alloy, the Au nanoflowers are arranged in a highly dispersive way, providing large number of active points which may benefit the catalytic reaction.

The electrocatalytic activities of the NPC-G towards glucose electrooxidation were characterized by CV curves in 0.1 mol/L KOH alkaline aqueous solutions with and without 50 mM glucose (Figure 4). When compared with that in KOH solution, the CV curves in KOH + glucose solutions exhibit an extra current density hump in the potential range of -0.4 – 0.6 V during the positive scan, where glucose oxidation, including the absorption of OH^{-1} ($\text{Au} + \text{H}_2\text{O} = \text{Au}(\text{OH})_{\text{ads}}^{1-x} + \text{H}^+ + xe^-$) and the oxidation of glucose (the interaction between the hemiacetal group of glucose molecules and

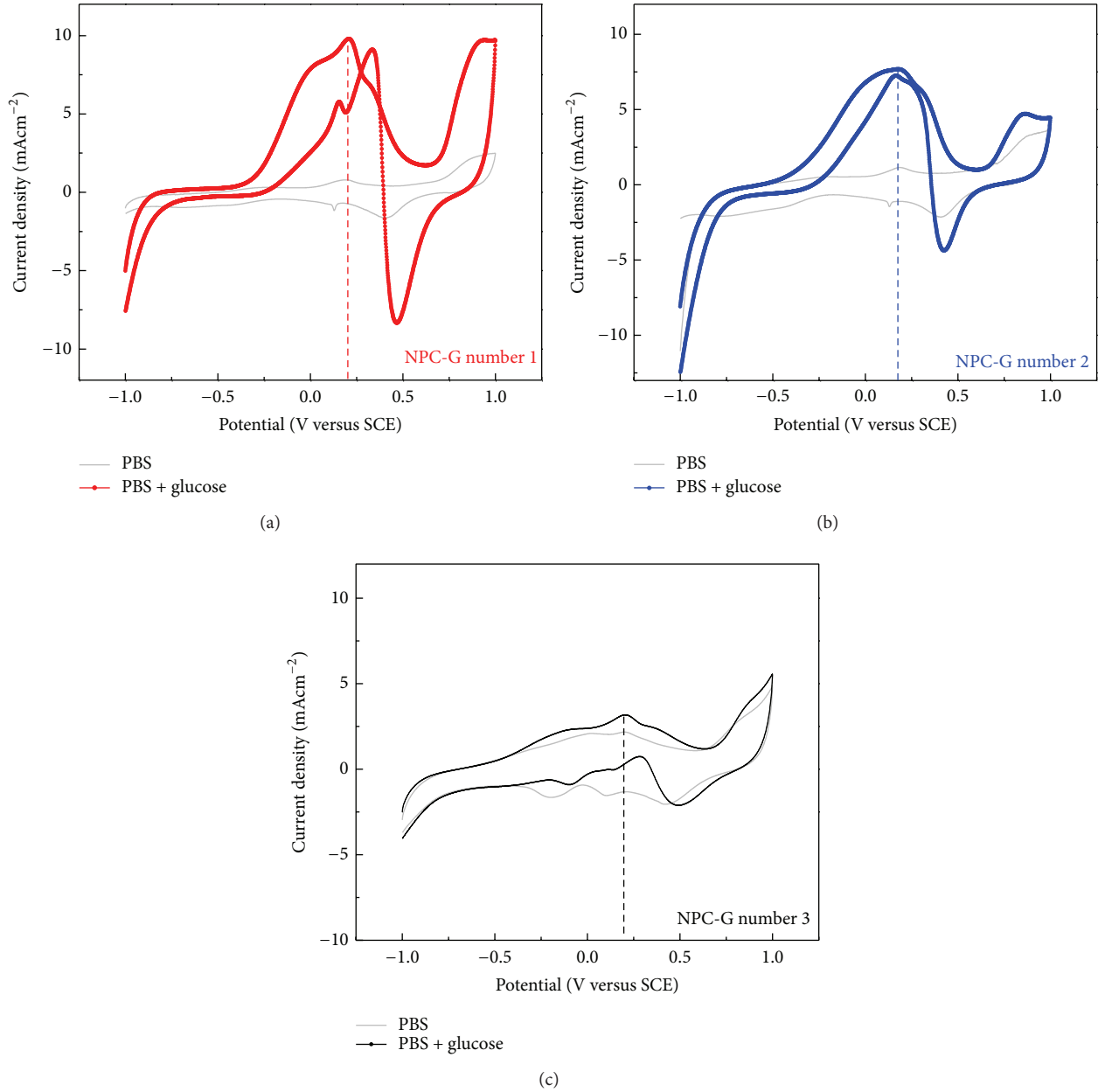


FIGURE 4: CV curves of the NPC-G samples in in 0.1 mol/L KOH alkaline aqueous solutions with 50 mmol/L glucose, scan rate 0.05 V/min, versus SCE.

Au(OH)_{ads}, takes place on the surface of the NPC-G samples. The peak position is at about 0.2 V, agreeing with the reported data on NPG and Au nanoparticles [13–17]. The current density value of the peak is 9.8 mA/cm², 7.6 mA/cm² a, and 3.2 mA/cm² for NPC-G 1 number, NPC-G 2 number, and NPC-G 3 number, respectively. The current peak density of NPC-G 1 number higher than that of the other NPC-G samples indicates that NPC-G 1 number has the highest catalytic activity. Therefore, NPC-G 1 number is chosen for the stability test and the result is shown in Figure 5. CV curves of a NPG sample with a characteristic pore size of 10 nm are also involved for comparison. In the case of NPG, the oxidation peak current value drops rapidly, decreasing

to 85.7% after one hundred cycle. Meanwhile, the oxidation peak (potential) shift with the increasing scans can be vividly seen. For NPC-G 1 number, neither peak shift nor peak current density decrease can be observed, indicating that NPC-G has both high catalytic activity and high stability.

4. Conclusions

NPC can be fabricated by dealloying the amorphous Ti₂Cu alloy in 0.03 M HF electrolytes. The characteristic pore size and ligament size of the NPC can be readily tailored by controlling the dealloying time. The as-prepared NPC provides fine nanoflowerpots to form highly dispersed Au

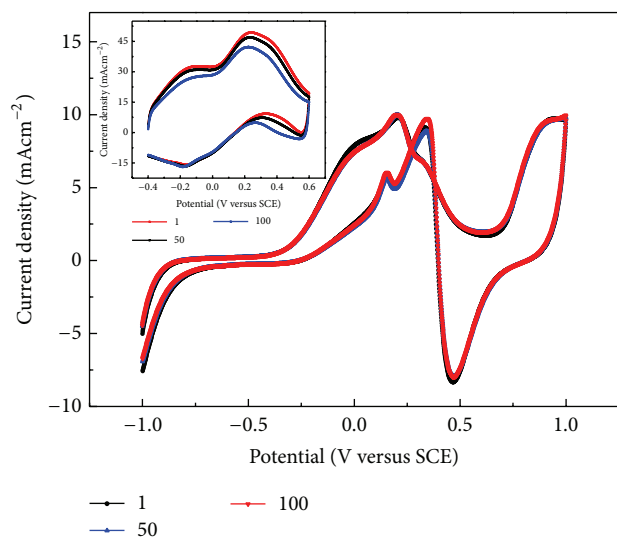


FIGURE 5: CV curves of NPC-G2 number before and after 100 potential cycles in 0.1 mol/L KOH alkaline aqueous solutions with 50 mmol/L glucose, scan rate 0.05 V/min. The inset is the CV curves of NPG during 100 potential cycles in the same conditions, versus SCE.

nanoflowers. The NPC-G structure exhibits both high catalytic activity and stability towards the oxidation of d-glucose, indicating that the amorphous alloys are ideal precursors to form nanoflowerpot which can grow functional nanoflowers.

Conflict of Interests

The authors declare that there is no conflict of interests regarding the publication of this paper.

Acknowledgments

This work is supported by the Project sponsored by the National Science Foundation of China (51001026), the Project sponsored by SRF for ROCS, SEM (6812000013), the Project sponsored by Nanjing for ROCS (7912000011), Opening Project of Jiangsu Key Laboratory of Advanced Metallic Materials (AMM201101), and the Fundamental Research Funds for the Central Universities (3212002205, 3212003102).

References

- [1] A. Inoue, "Stabilization of metallic supercooled liquid and bulk amorphous alloys," *Acta Materialia*, vol. 48, no. 1, pp. 279–306, 2000.
- [2] W. H. Wang, C. Dong, and C. H. Shek, "Bulk metallic glasses," *Materials Science and Engineering R: Reports*, vol. 44, no. 2, pp. 45–89, 2004.
- [3] I. Akihisa, "Stabilization of supercooled liquid and opening-up of bulk glassy alloys," *Proceedings of the Japan Academy B: Physical and Biological Sciences*, vol. 73, no. 2, pp. 19–24.
- [4] G. Kumar, H. X. Tang, and J. Schroers, "Nanomoulding with amorphous metals," *Nature*, vol. 457, no. 7231, pp. 868–873, 2009.

- [5] J. Erlebacher, M. J. Aziz, A. Karma, N. Dimitrov, and K. Sieradzki, "Evolution of nanoporosity in dealloying," *Nature*, vol. 410, no. 6827, pp. 450–453, 2001.
- [6] T. Fujita, L.-H. Qian, K. Inoke, J. Erlebacher, and M.-W. Chen, "Three-dimensional morphology of nanoporous gold," *Applied Physics Letters*, vol. 92, no. 25, Article ID 251902, 2008.
- [7] X. Ge, R. Wang, P. Liu, and Y. Ding, "Platinum-decorated nanoporous gold leaf for methanol electrooxidation," *Chemistry of Materials*, vol. 19, no. 24, pp. 5827–5829, 2007.
- [8] Z. Yi, X. Tan, G. Niu et al., "Facile preparation of dendritic Ag-Pd bimetallic nanostructures on the surface of Cu foil for application as a SERS-substrate," *Applied Surface Science*, vol. 258, no. 14, pp. 5429–5437, 2012.
- [9] J. Erlebacher, "An atomistic description of dealloying porosity evolution, the critical potential, and rate-limiting behavior," *Journal of the Electrochemical Society*, vol. 151, pp. 614–626, 2004.
- [10] J. Yu, Y. Ding, C. Xu, A. Inoue, T. Sakurai, and M. Chen, "Nanoporous metals by dealloying multicomponent metallic glasses," *Chemistry of Materials*, vol. 20, no. 14, pp. 4548–4550, 2008.
- [11] X. Y. Lang, H. Guo, L. Y. Chen et al., "Novel nanoporous Au-Pd Alloy with high catalytic activity and excellent electrochemical stability," *Journal of Physical Chemistry C*, vol. 114, no. 6, pp. 2600–2603, 2010.
- [12] X. Luo, R. Li, Z. Liu et al., "Three-dimensional nanoporous copper with high surface area by dealloying Mg-Cu-Y metallic glasses," *Materials Letters*, vol. 76, pp. 96–99, 2012.
- [13] Z. Liu, L. Huang, L. Zhang, H. Ma, and Y. Ding, "Electrocatalytic oxidation of d-glucose at nanoporous Au and Au-Ag alloy electrodes in alkaline aqueous solutions," *Electrochimica Acta*, vol. 54, no. 28, pp. 7286–7293, 2009.
- [14] B. K. Jena and C. R. Raj, "Enzyme-free amperometric sensing of glucose by using gold nanoparticles," *Chemistry*, vol. 12, no. 10, pp. 2702–2708, 2006.
- [15] T. Fujita, T. Tokunaga, L. Zhang et al., "Atomic observation of catalysis-induced nanopore coarsening of nanoporous gold," *Nano Letters*, vol. 3, Article ID 3015, 2014.
- [16] Y. Bai, W. Yang, Y. Sun, and C. Sun, "Enzyme-free glucose sensor based on a three-dimensional gold film electrode," *Sensors and Actuators B: Chemical*, vol. 134, no. 2, pp. 471–476, 2008.
- [17] X.-Y. Lang, H.-Y. Fu, C. Hou et al., "Nanoporous gold supported cobalt oxide, microelectrodes as high-performance electrochemical biosensors," *Nature Communications*, vol. 4, no. 2169, pp. 1–8, 2013.

Research Article

Selection of the Composition with High Glass Forming Ability in Zr-Cu-Ni-Al Bulk Metallic Glasses

Yajuan Sun,¹ Yumin Li,¹ and Hongjing Wang²

¹ School of Science, Tianjin Polytechnic University, Tianjin 300387, China

² Advanced Technology and Materials Co. Ltd., Beijing 100081, China

Correspondence should be addressed to Yajuan Sun; sunyajuan1998@126.com

Received 16 February 2014; Accepted 28 April 2014; Published 15 May 2014

Academic Editor: Limei Xu

Copyright © 2014 Yajuan Sun et al. This is an open access article distributed under the Creative Commons Attribution License, which permits unrestricted use, distribution, and reproduction in any medium, provided the original work is properly cited.

Three new Zr-Cu-Ni-Al bulk metallic glasses were developed through appropriate mixing of three binary eutectics $Zr_{38.2}Cu_{61.8}$, $Zr_{51}Al_{49}$, and $Zr_{64}Ni_{36}$. By suppressing solidification of competing crystalline phases, a new glass forming alloy $Zr_{51}Cu_{24.22}Ni_{14.06}Al_{10.72}$ with the critical diameter of up to 10 mm is obtained.

1. Introduction

Zr-based bulk metallic glasses (BMGs) exhibit many fantastic properties, which are considered as potential structural materials [1–3]. Although some large dimension Zr-based bulk metallic alloys can be obtained as far, such as Zr-Ti-Ni-Cu-Be [4], Zr-Cu-Ni-Al [5, 6], Zr-Ti-Cu-Ni-Al [7], Zr-(Ag, Cu)-Al [8], and so on. However, these high GFA Zr-based metallic glasses more or less contain some toxic element (e.g., Be) or noble metals (e.g., Ag, Pd, and Pt). They are still cannot fulfill the requests from commercial applications. The Zr-Cu-Ni-Al system is a promising candidate for applications due to its nontoxicity and low cost. Hence, developing the new Zr-Cu-Ni-Al glass compositions with high glass forming ability (GFA) is important for the engineering application. At present, various rules have been proposed to design potential glass forming compositions, such as three empirical, but insufficiency and imperfectness still exist [9–11]. Therefore, seeking an efficient guideline to direct this work is still of great challenge.

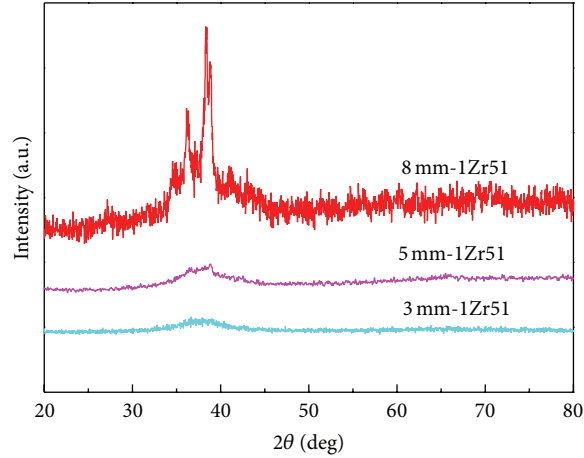
The investigations by Shen et al. [12] and Lu et al. [13] ever suggested that multicomponent glass forming compositions could be approximately synthesized by the compositions of binary eutectics between the constituent elements through appropriate ratios. Usually, there are two features with these binary eutectics: (1) eutectic temperature is relatively low; (2) the products of the eutectic reactions are linear compounds.

This new method was called appropriate mixing of binary eutectics. As far as now, several Zr-based [12], Ni-based [14], and Cu-based [15] bulk metallic glasses have been successfully developed based on this new approach, which thoroughly demonstrated its usefulness for searching new BMG compositions with high GFA.

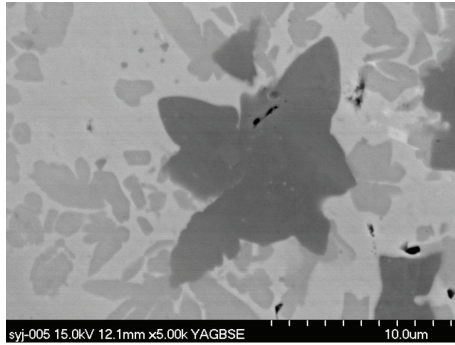
In this paper, three new amorphous alloys of the Zr-Cu-Ni-Al glass forming system were designed, through appropriate mixing of binary eutectic units $Zr_{38.2}Cu_{61.8}$, $Zr_{51}Al_{49}$, and $Zr_{64}Ni_{36}$. In terms of suppressing the competing crystalline phases in the amorphous matrix which precipitated during melt cooling [16], ratios of these binary eutectic units were adjusted. Therefore, on the condition of without increasing the component but only changing the ratios among these components, three new Zr-Cu-Ni-Al alloys with high GFA were obtained. One of the three new alloys with a critical diameter of 10 mm was achieved by only a few times of experiments. Furthermore, GFA of all the three Zr-based amorphous alloys is discussed and investigated through phase selection.

2. Experiment

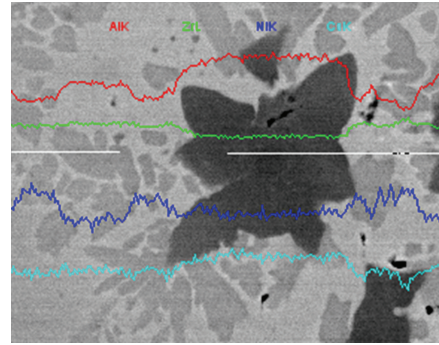
The Zr-Cu-Ni-Al alloy ingots were prepared by arc melting the mixture of pure Zr (99.5%), Cu (99.9%), Ni (99.9%), and Al (99.99%) metals in a purified argon atmosphere. In order



(a) XRD patterns for as-cast 1Zr51 samples with the diameters of 3 mm, 5 mm, and 8 mm



(b) SEM-BSE image for the as-cast 1Zr51 sample with a diameter of 8 mm



(c) EDS line analysis showing element distribution in the as-cast 1Zr51 sample with a diameter of 8 mm

FIGURE 1: The XRD and SEM patterns for as-cast 1Zr51 samples in different diameters.

to ensure the homogeneous composition, master alloys were remelted 4 times, and then they were sucked into the copper mold to form amorphous rod samples in different diameters.

The structure of the as-cast samples was characterized by X-ray diffraction (XRD) with Cu $K\alpha$ radiation (D/MAX-RB diffractometer). Then scanning electron microscopy (SEM) investigations were performed on the Hitachi S-4700. Thermal analysis was carried out by differential scanning calorimetry (Perkin-Elmer DSC7) and differential thermal analysis (Perkin-Elmer DTA7), both at a heating rate of 0.33 K/s.

3. Results and Discussion

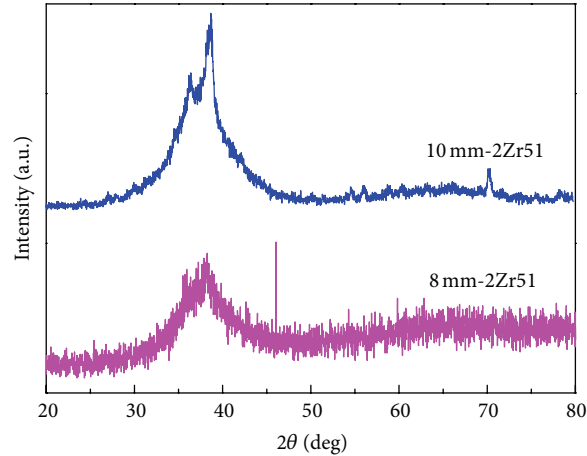
3.1. Formation and Optimization of New Zr-Cu-Ni-Al Glass Alloys. Numerous experimental lines of evidence demonstrated that in Zr-Cu-Ni-Al amorphous alloy system, the primary crystalline phases are mainly Zr-Cu, Zr-Ni, and Zr-Al intermetallic compounds, which are always treated as competing phases with respect to glass phase in this alloy system during cooling melt. Once the driving forces for precipitations of all competing crystalline phases are equivalent, constraints among one another to prevent precipitating might

increase, which then leads to a high glass forming ability. Therefore, based on the mixing of binary deep eutectics of $Zr_{38.2}Cu_{61.8}$, $Zr_{64}Ni_{36}$, and $Zr_{51}Al_{49}$, we choose them as the basic units to design new alloys, which are listed as follows:

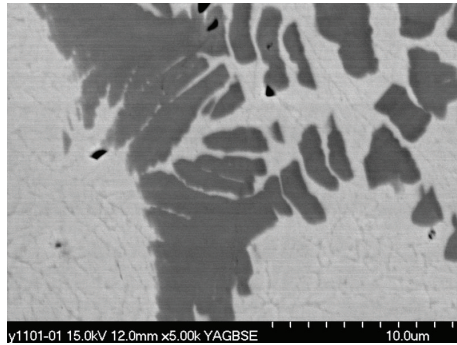
$$C_{am} = a(Zr_{38.2}Cu_{61.8}) + b(Zr_{64}Ni_{36}) + c(Zr_{51}Al_{49}) \quad (a + b + c = 1), \quad (1)$$

where C_{am} is multicomponent alloy composition; a , b , and c are the coefficients for the three basic binary eutectic units, respectively, and their sum is the unity. By varying the coefficients of a , b , and c , the atomic ratios of the alloy components can be changed and then different compositions of Zr-Cu-Ni-Al system can be obtained.

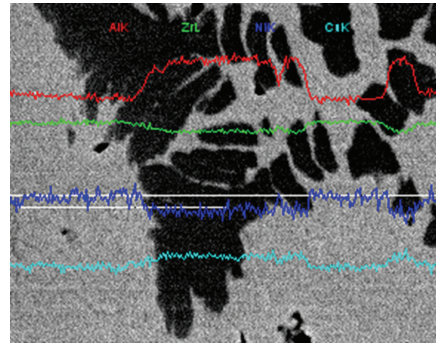
Initially, we assigned the coefficients as $a = 1/3$, $b = 1/3$, and $c = 1/3$ in (1) straightforwardly and then the composition C_{am} of $Zr_{51}Cu_{20.7}Ni_{12}Al_{16.3}$ (abbreviated as 1Zr51) with a D_{max} of 3 mm was followed. The diffuse peak of XRD pattern in Figure 1(a) proves only a single amorphous matrix in this sample. However, for the samples of 5 mm and 8 mm in diameters, both XRD pattern (as shown in Figure 1(a)) and SEM-BSE image (as shown in Figure 1(b)) give out some crystalline phases that are dispersed in the amorphous



(a) XRD patterns for as-cast 2Zr51 samples with the diameters of 8 mm and 10 mm



(b) SEM-BSE image for the as-cast 2Zr51 sample with a diameter of 10 mm



(c) EDS linear analysis showing element distribution in the as-cast 2Zr51 sample with a diameter of 10 mm

FIGURE 2: The XRD and SEM patterns for as-cast 2Zr51 samples in different diameters.

matrix. Furthermore, Al is enriched in the primary crystalline phases by SEM-BSE and EDS (as shown in Figure 1(c)) results. Therefore, it can be implied that the precipitation of enriched Al phases is the main obstacle to further enhance GFA of this alloy 1Zr51 (i.e., content of aluminum element is relatively excessive, compared to other elements).

As a result, in order to improve the GFA of this alloy system without increasing the component species, we tried to decrease the coefficients for $Zr_{51}Al_{49}$ eutectic units in (1) to depress the precipitation of enriched Al phases. Thus, on the base of the initial alloy 1Zr51, the coefficient for $Zr_{51}Al_{49}$ eutectic units was decreased to $c = 2/8$, but coefficients for $Zr_{64}Ni_{36}$ and $Zr_{38.2}Cu_{61.8}$ eutectic units were increased to $a = b = 3/8$. And this led to the new composition of $Zr_{51}Cu_{23.2}Ni_{13.5}Al_{12.25}$ (abbreviated as 2Zr51) accompanied with an amorphous rod sample of 8 mm in diameter. Also the XRD patterns for this as-cast 2Zr51 rod samples in different diameters are shown in Figure 2(a). It can be clearly seen that the 8-mm 2Zr51 is essentially amorphous, evidenced by the unique broad diffuse halo in this XRD. This means GFA of this alloy system has been improved through turning the coefficients of a , b , and c . However, when we increased the size of the 2Zr51 rod sample to a diameter of 10 mm, as the

XRD pattern in Figure 2(a), SEM-BSE, and EDS images in Figures 2(b) and 2(c) results indicated, some enriched Al phases precipitated during cooling the melt.

From the above discussion, to suppress precipitation of enriched Al phases and get better glass former, we can decrease the coefficient of c in (1) to $c = 3.5/16$, while a and b increase to $a = b = 6.25/16$. As a result, it followed another composition of $Zr_{51}Cu_{24.22}Ni_{14.06}Al_{10.72}$ (abbreviated as 3Zr51), and we finally obtained an amorphous rod sample of 10 mm in diameter. The XRD pattern in Figure 3(a) shows only a single diffuse halo that displays a homogeneous matrix without any crystalline phases. Further, SEM-BSE image in Figure 3(b) indicates that there are no crystalline phases. All of these demonstrated that the 3Zr51 rod sample with the diameter of 10 mm is in full amorphous state. However, when increasing the size of the 3Zr51 alloy to 12 mm in diameter, some crystalline phases precipitate. The sharp peaks in XRD pattern are shown in Figure 3(a). It is noted that potential alloy compositions with even better GFA could be difficultly found by adjustment of coefficients further in (1).

The alloy compositions, abbreviations, adjustment of mixing constants, and critical sizes D_{max} are summarized in Table 1.

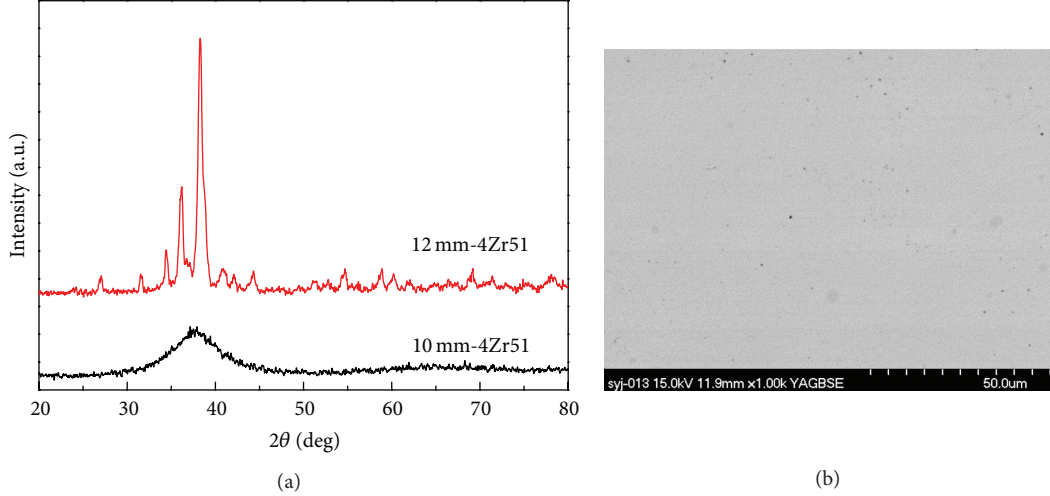


FIGURE 3: The XRD (a) and SEM-BSE (b) patterns for as-cast 3Zr51 sample with the diameter of 10 mm.

TABLE 1: The new alloy compositions, abbreviations, adjustment of mixing constants, critical sizes D_{\max} , and thermal parameters for the Zr-Cu-Ni-Al alloys.

BMGs compositions (abbreviation)	Mixing coefficients a , b , and c	D_{\max}	T_g	T_x	T_m	T_g/T_m
$Zr_{51}Cu_{20.7}Ni_{12}Al_{16.3}$ (1Zr51)	$a = 1/3, b = 1/3, c = 1/3$	<5 mm	727	817	1049	0.6930
$Zr_{51}Cu_{23.2}Ni_{13.5}Al_{12.25}$ (2Zr51)	$a = 3/8, b = 3/8, c = 2/8$	8 mm	726	806	1047	0.6934
$Zr_{51}Cu_{24.22}Ni_{14.06}Al_{10.72}$ (3Zr51)	$a = 6.25/16, b = 6.25/16, c = 3.5/16$	10 mm	725	781	1041	0.6964

TABLE 2: The critical sizes (D_{\max}) in our lab for previously reported Zr-based BMGs.

Amorphous alloy systems with the corresponding abbreviation	D_{\max}
$Zr_{65}Cu_{17.5}Ni_{10}Al_{7.5}$ (Zr65) [5]	<6 mm
$Zr_{55}Cu_{30}Ni_5Al_{10}$ (Zr55) [6]	<10 mm
$Zr_{51}Cu_{24.22}Ni_{14.06}Al_{10.72}$ (3Zr51) [present]	10 mm

For further comparisons, some other previously reported Zr-based amorphous alloys with high GFA were also fabricated under the same experimental condition in our lab. Table 2 lists their critical sizes (D_{\max}) in our lab. The XRD patterns are shown in Figure 4. It indicates that among the Zr-Cu-Ni-Al quaternary alloy systems, 3Zr51 owns the largest size. It is believed that a further improvement of the prepared methods causes the formation of 3Zr51 bulk amorphous alloy with a larger diameter.

3.2. Thermal Analysis of New Zr-Cu-Ni-Al Glass Alloys. DSC and DTA curves for the amorphous alloys of the three different Zr-Cu-Ni-Al alloys are shown in Figure 5. Corresponding thermal parameters are listed in Table 1, including the glass transition temperature T_g , onset crystallization temperature T_x , melting temperature T_m , and reduced glass transition temperature $T_{rg} = T_g/T_m$. As can be seen in Figure 5(a), the three alloys show a distinct glass transition, a significant supercooled liquid region, and a clear endothermic event, illustrating characteristics of BMGs. So as far as now, the

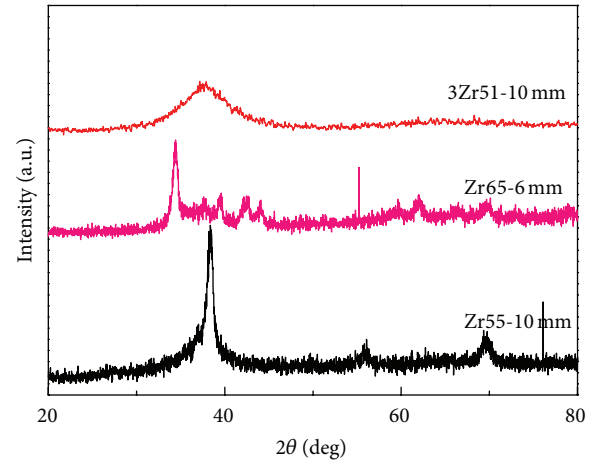


FIGURE 4: The XRD patterns for previously reported as-cast Zr-based amorphous alloy samples in different diameters.

reduced glass transition temperature T_{rg} and the critical size D_{\max} of the samples are the most powerful criteria to characterize the glass forming ability. Distinct correlation is found between GFA and the values of T_{rg} for our newly developed alloys. Among the three new alloys, the best glass forming alloy 3Zr51 processes highest value of T_{rg} .

3.3. Glass Forming Ability of New Zr-Cu-Ni-Al Glass Alloys. As we discussed formerly, eutectic compositions are the best candidates for glass formation. Another thing we should

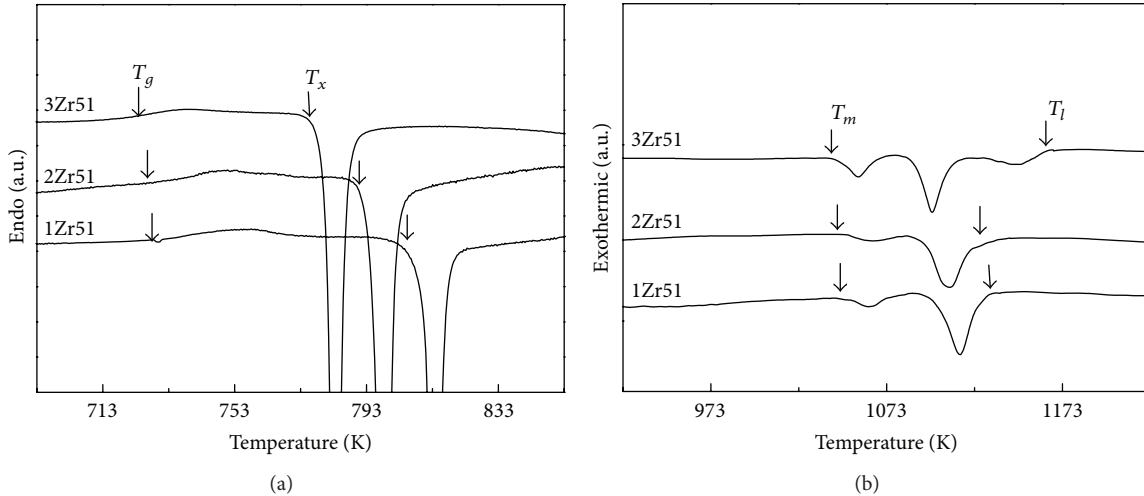


FIGURE 5: The DSC (a) and DTA (b) curves for as-cast 1Zr51, 2Zr51, and 3Zr51 BMG samples.

mention again is that in our mixing of binary eutectics method, the eutectic reaction products are both linear compounds. As Shen et al. [12] ever suggested if the chemical affinity between the eutectic atomic pairs can be balanced to a certain degree, the atomic rearrangement to form crystalline phases during melt cooling is rather difficult, which structurally supports improving glass forming ability. That is why we preferred to choose $Zr_{38.2}Cu_{61.8}$, $Zr_{64}Ni_{36}$, and $Zr_{51}Al_{49}$ as the three preliminary units. We also assumed that such a balance can be achieved by proportionally mixing the corresponding binary eutectic compositions.

As a matter of fact, the physical meaning of this method is ambiguous, but lots of compositions obtained through our new method and reported in the literatures demonstrate that the efficiency of this method is astonishing. The compositions obtained through proportionally combining the binary eutectics are very close to those reported in the literatures [17]. However, it must be noted that the binary eutectics should be involved in reactions with compound products and the ratios between the eutectics should be varied according to experiments.

On the other hand, during cooling the alloy melt phase selection is inevitably avoided. Either crystalline phases or metallic glass will be obtained. However, as Ma et al. [18] pointed out if treating glass as another competing phase, glass formation could be interpreted as the complete suppression of crystal growth by glass phase. So once the crystalline phase's precipitation is depressed, GFA will be naturally improved.

Thus, according to the above concept, we designed the first composition $Zr_{51}Cu_{20.7}Ni_{12}Al_{16.3}$ (1Zr51) by assigning $a = b = c = 1/3$ as described in (1). In fact, this assignment is straightforwardly obtained and we succeeded in obtaining a 3 mm as-cast rod sample. Its efficiency can be proved by experiments. However, some enriched Al crystalline phases appear in a larger sample of 5 mm and 8 mm in diameter. Lu et al. [19] ever suggested that in order to obtain the better glass forming composition, primary precipitation in the melt should be bypassed no matter what crystalline phases they

are. One of the effective approaches is to suppress the precipitation of crystalline phases through phase competition. Here we just choose to vary the ratios of the three eutectic units rather than introduce another component. Consequently, the second composition $Zr_{51}Cu_{23.2}Ni_{13.5}Al_{12.25}$ (2Zr51) was obtained when $a = b = 3/8$, but $c = 2/8$. And correspondingly we obtained a larger as-cast amorphous rod with a diameter of 8 mm. But a larger 10 mm rod sample with some enriched Al crystalline phases once reminded us that if we want to improve the GFA of this alloy system, adjusting the ratios must be tried another time. By varying the ratios of the three units to $a = b = 6.25/16$ while $c = 3.5/16$, the third alloy $Zr_{51}Cu_{24.22}Ni_{14.06}Al_{10.72}$ (3Zr51) finally followed which can be cast into an amorphous rod up to 10 mm in diameter. It is one of the best glass formers in the Zr-Cu-Ni-Al alloy system.

Ma et al. [18] ever suggested a microstructure-based method to pinpoint the best glass forming composition. From lots of their work, pinpointing the composition was largely based on the microstructure evolution. Here the concept is the same. The difference is that their work largely relied on the phase diagram. But we depressed the precipitation of competing phases only through varying the ratios of the three eutectic units. On the other hand, during this variation, chemical affinities of the four components gradually got balanced. The alloy compositions with high GFA were obtained by varying three eutectic units coefficients a , b , and c .

Furthermore, we analyzed the reason for the increase in GFA of 2Zr51 and 3Zr51 compared with 1Zr51. As can be seen from Table 1, T_m decreases with the composition. High T_{rg} for 2Zr51 and 3Zr51 indicates that the alloy is close to deep eutectic and, therefore, exhibits better GFA. Especially, 3Zr51 has a rather low T_m . The decrease in melting point indicates that the liquid phase is stabilized with respect to competing crystalline phases. Also knowing from physical metallurgy, we understand that viscosities of eutectic alloys are usually higher than other off-eutectics, which dynamically supported the best glass forming composition of them. As a result, 2Zr51

and 3Zr51 show high GFA compared with 1Zr51, because the alloy compositions are closer to deep eutectic by varying ratios of the three binary units.

4. Conclusion

We utilized an efficient method of proportional mixing of binary eutectics to successfully design three new Zr-Cu-Ni-Al quaternary amorphous alloy compositions. Firstly we obtained a composition $Zr_{51}Cu_{20.7}Ni_{12}Al_{16.3}$ (1Zr51) with a critical maximal size of 3 mm in diameter. Then, through varying the atomic ratios in this composition, a full amorphous $Zr_{51}Cu_{24.22}Ni_{14.06}Al_{10.72}$ (3Zr51) rod sample with a critical maximal diameter of 10 mm was achieved. High GFA of the three alloys resulted from depressing these precipitated phases by varying ratios of the three binary units.

Conflict of Interests

The authors declare that there is no conflict of interests regarding the publication of this paper.

Acknowledgments

The research was supported by the Tianjin Research Program of Application Foundation and Advanced Technology (no. 13JCQNJC02900).

References

- [1] W. L. Johnson, "Bulk glass-forming metallic alloys: science and technology," *MRS Bulletin*, vol. 24, no. 10, pp. 42–56, 1999.
- [2] W. H. Wang, C. Dong, and C. H. Shek, "Bulk metallic glasses," *Materials Science and Engineering: Reports*, vol. 44, no. 2-3, pp. 45–89, 2004.
- [3] W. Chen, Z. Liu, and J. Schroers, "Joining of bulk metallic glasses in air," *Acta Materialia*, vol. 62, pp. 49–57, 2014.
- [4] A. Peker and W. L. Johnson, "A highly processable metallic glass: $Zr_{41.2}Ti_{13.8}Cu_{12.5}Ni_{10.0}Be_{22.5}$," *Applied Physics Letters*, vol. 63, Article ID 2342, 1993.
- [5] A. Inoue, T. Zhang, N. Nishiyama, K. Ohba, and T. Masumoto, "Preparation of 16 mm diameter rod of amorphous $Zr_{65}Al_{7.5}Ni_{10}Cu_{17.5}$ alloy," *Materials Transactions, JIM*, vol. 34, no. 12, pp. 1234–1237, 1993.
- [6] A. Inoue and T. Zhang, "Fabrication of bulk glassy $Zr_{55}Al_{10}Ni_5Cu_{30}$ alloy of 30 mm in diameter by a suction casting method," *Materials Transactions, JIM*, vol. 37, no. 2, pp. 185–187, 1996.
- [7] L. Q. Xing, P. Ochin, M. Harmelin, F. Faudot, J. Bigot, and J. P. Chevalier, "Cast bulk Zr–Ti–Cu–Ni amorphous alloys," *Materials Science and Engineering: A*, vol. 220, no. 1-2, pp. 155–161, 1996.
- [8] Q. K. Jiang, X. D. Wang, X. P. Nie et al., "Zr–(Cu,Ag)–Al bulk metallic glasses," *Acta Materialia*, vol. 56, no. 8, pp. 1785–1796, 2008.
- [9] A. Inoue, J. Saida, M. Matsushita, and T. Sakurai, "Formation of an icosahedral quasicrystalline phase in $Zr_{65}Al_{7.5}Ni_{10}M_{17.5}$ (M = Pd, Au or Pt) alloys," *Materials Transactions, JIM*, vol. 41, no. 2, pp. 362–365, 2000.
- [10] A. Inoue, "Stabilization of metallic supercooled liquid and bulk amorphous alloys," *Acta Materialia*, vol. 48, no. 1, pp. 279–306, 2000.
- [11] J. F. Löffler, "Bulk metallic glasses," *Intermetallics*, vol. 11, no. 6, pp. 529–540, 2003.
- [12] J. Shen, J. Zou, L. Ye et al., "Glass-forming ability and thermal stability of a new bulk metallic glass in the quaternary Zr–Cu–Ni–Al system," *Journal of Non-Crystalline Solids*, vol. 351, no. 30–32, pp. 2519–2523, 2005.
- [13] Z. P. Lu, J. Shen, D. W. Xing, J. F. Sun, and C. T. Liu, "Binary eutectic clusters and glass formation in ideal glass-forming liquids," *Applied Physics Letters*, vol. 89, Article ID 071910, 2006.
- [14] W. Z. Liang, *Glass-forming ability and fracture behavior of NiTiZrAlCuSi alloys [Ph.D. dissertation]*, Harbin Institute of Technology, Harbin, China, 2003.
- [15] Y. J. Yang, D. W. Xing, C. P. Li, S. D. Wei, J. K. Sun, and Q. K. Shen, "A new way of designing bulk metallic glasses in Cu–Ti–Zr–Ni system," *Materials Science and Engineering: A*, vol. 448, no. 1-2, pp. 15–19, 2007.
- [16] D. Wang, H. Tan, and Y. Li, "Multiple maxima of GFA in three adjacent eutectics in Zr–Cu–Al alloy system—a metallographic way to pinpoint the best glass forming alloys," *Acta Materialia*, vol. 53, no. 10, pp. 2969–2979, 2005.
- [17] Y. J. Sun, D. D. Qu, Y. J. Huang et al., "Zr–Cu–Ni–Al bulk metallic glasses with superhigh glass-forming ability," *Acta Materialia*, vol. 57, no. 4, pp. 1290–1299, 2009.
- [18] D. Ma, H. Tan, D. Wang, Y. Li, and E. Ma, "Strategy for pinpointing the best glass-forming alloys," *Applied Physics Letters*, vol. 86, Article ID 191906, 2005.
- [19] Z. P. Lu, D. Ma, C. T. Liu, and Y. A. Chang, "Competitive formation of glasses and glass-matrix composites," *Intermetallics*, vol. 15, no. 3, pp. 253–259, 2007.

Research Article

Nanocrystalline Phase Formation inside Shear Bands of Pd-Cu-Si Metallic Glass

Yang Shao,^{1,2} Guannan Yang,^{1,2} and Kefu Yao^{1,2}

¹ School of Materials Science and Engineering, Tsinghua University, Beijing 100084, China

² Key Laboratory for Advanced Materials Processing Technology, Ministry of Education, Tsinghua University, Beijing 100084, China

Correspondence should be addressed to Yang Shao; shaoyang@tsinghua.edu.cn

Received 21 March 2014; Accepted 23 April 2014; Published 14 May 2014

Academic Editor: Na Chen

Copyright © 2014 Yang Shao et al. This is an open access article distributed under the Creative Commons Attribution License, which permits unrestricted use, distribution, and reproduction in any medium, provided the original work is properly cited.

Pd_{77.5}Cu₆Si_{16.5} metallic glass was prepared by fluxing treatment and water quenching method. To avoid possible artifacts, shear bands were created by indentation after TEM sample preparation. Bright field image, diffraction pattern, and the dark field image of TEM that covered the shear band region were presented. A few nanocrystalline phases were noticed inside the shear bands, which favored the plastic deformation ability and supported the explanation of mechanical deformation-induced crystallization.

1. Introduction

Metallic glasses (MGs) are a kind of advanced engineering materials due to their high strength, high elastic limit, and better corrosion resistance compared to their crystalline counterparts [1]. However, two dilemmas apparently deteriorate MGs' applications as promising structural engineering materials: one is the limited critical size, and the other is the poor plastic deformation ability for most MGs. The plastic carriers of MGs, shear bands, are of two-dimensional defects. Their formation and propagation are fundamentally important for understanding the plastic deformation mechanism in MGs. However, little is known so far and even the structure of shear band is still a mystery. Lots of work has been carried out to investigate the properties of shear bands, including structure dilatation [2, 3], diffusivity [4], and strength [3]. Since the thickness of shear bands is about few tens of nanometers [4], transmission electron microscope (TEM) is often used to study the morphology, nanoscale defects [5, 6], and nanocrystalline phases [7–10] in the shear bands. However, conventional TEM sample preparation methods cannot avoid some artifacts that induced by ion impinging damage or chemical thinning. The artifacts introduced during sample preparation therefore may cover up the original structure of shear bands. The nanocrystalline phase formation during the plastic deformation process has been noticed, but the exact reason of crystalline phase formation is still under debate

[9]. In this paper, to avoid any possible artifact, shear bands were introduced in the Pd-Cu-Si MG after the TEM sample preparation. Nanocrystalline phases are identified within the prepared shear bands, which may provide some hints to understand the different mechanisms of crystalline phase formation.

2. Materials and Methods

The ingot of the nominal Pd_{77.5}Cu₆Si_{16.5} metallic glass was prealloyed by high frequency induction melting the mixtures of high purity Pd (99.5%), Cu (99.99%), and Si (99.99%) under argon pressure in a quartz tube and then purified three times in B₂O₃ fluxing medium under a vacuum of 10⁻² Pa followed by water quenching. A cylindrical sample with 6 mm in diameter was obtained. The as-prepared samples were examined by X-ray diffraction (XRD) technique using a Japan Rigaku D/max-RB XRD spectrometry. The specimens of 2 × 2 × 4 mm³ were cut from the middle part of as-cast Pd_{77.5}Cu₆Si_{16.5} and used for room temperature compression tests on a WDW-50 testing machine at a strain rate of 4 × 10⁻⁴ m·s⁻¹. Samples with a diameter of 3 mm were cut from the ingot for TEM analysis. After mechanical thinning of the sample for TEM examination, the sample was subject to twin-jet electropolishing until a hole appeared. The electropolishing solution is a mixture of 77 vol.% CH₃COOH

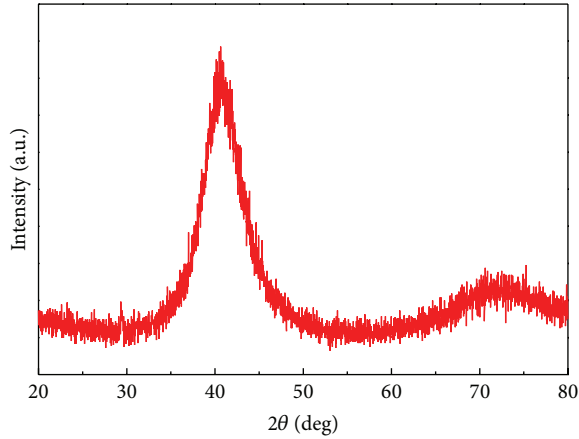


FIGURE 1: X-ray diffraction spectrum of as-prepared $\text{Pd}_{77.5}\text{Cu}_6\text{Si}_{16.5}$ metallic glass. Only two broad peaks could be observed indicating a glassy nature of $\text{Pd}_{77.5}\text{Cu}_6\text{Si}_{16.5}$ metallic glass.

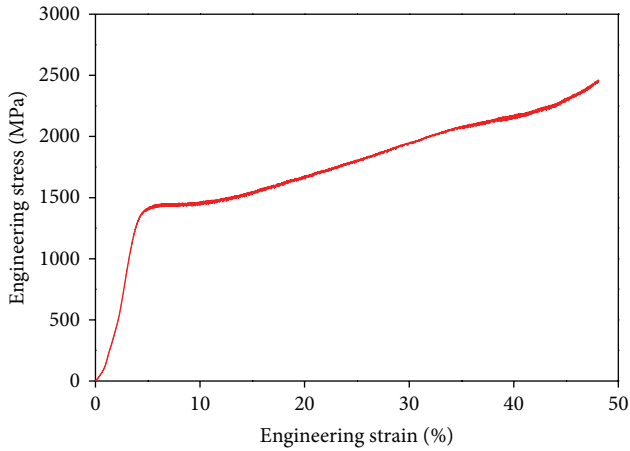


FIGURE 2: Engineering stress-strain curve for $\text{Pd}_{77.5}\text{Cu}_6\text{Si}_{16.5}$ metallic glass.

plus 23 vol.% HClO_4 . To avoid the possible artifacts in the subsequent observation of shear bands, which may arise from preferred thinning by either chemical polishing or ion etching during TEM sample preparation, the shear bands studied in this paper were created after TEM sample preparation by indentation near the transparent part of the sample. By doing so, a few shear bands that are suitable for TEM analysis were obtained. The TEM inspection was performed on an FEI Tecnai F20 G2 operated at 200 kV and integrated with an FEI Eagle 2 K CCD.

3. Results and Discussion

Figure 1 showed the XRD spectrum of the as-prepared $\text{Pd}_{77.5}\text{Cu}_6\text{Si}_{16.5}$ metallic glass. Besides the two broad peaks there, no sharp peak could be detected on the XRD spectrum in the 2-theta range from 20 to 80 degree, indicating a glassy nature of the as-prepared $\text{Pd}_{77.5}\text{Cu}_6\text{Si}_{16.5}$ metallic glass. Figure 2 showed the engineering stress-strain curve of

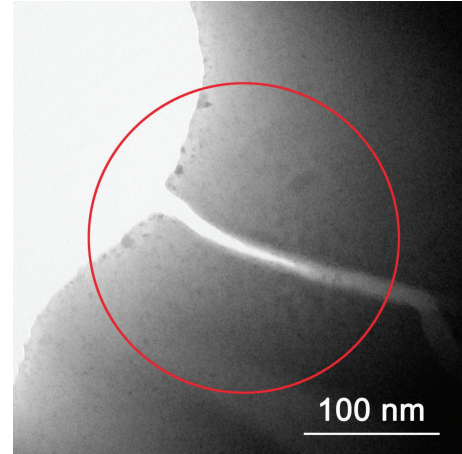


FIGURE 3: TEM bright field image of the region containing a clear shear band. The red circle indicated a region used for later electron diffraction.

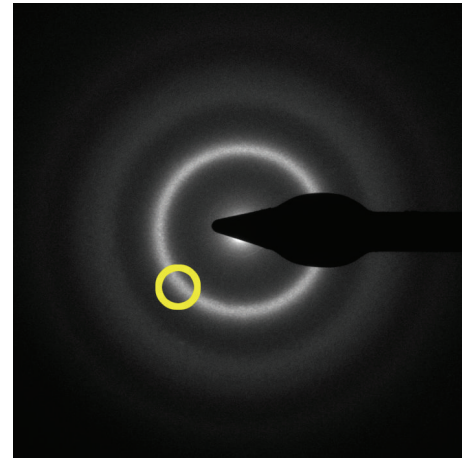


FIGURE 4: Selected area electron diffraction pattern from the region marked with red circle in Figure 2. The two diffuse halos show the glassy nature of as-prepared $\text{Pd}_{77.5}\text{Cu}_6\text{Si}_{16.5}$ metallic glass in microscale. The part of inner halo marked by yellow circle was used for later TEM dark field imaging.

the as-prepared $\text{Pd}_{77.5}\text{Cu}_6\text{Si}_{16.5}$ metallic glass. The yield strength of $\text{Pd}_{77.5}\text{Cu}_6\text{Si}_{16.5}$ was about 1300 MPa, and the engineering strain was up to 40%, showing excellent plastic deformation ability. Figure 3 showed a bright field image of the created shear band in $\text{Pd}_{77.5}\text{Cu}_6\text{Si}_{16.5}$ metallic glass. From Figure 3, a clear shear band with a thickness of 13 nm could be noticed, and a microcrack could also be observed at one end of the shear band. A diffraction pattern that covered the region marked with a red circle in Figure 3 was shown in Figure 4. No clear diffraction spots could be noticed, except two halos in Figure 4, suggesting a glass nature of the as-prepared sample, which was also consistent with our XRD result. By using a part of inner halo ring indicated by a yellow circle in Figure 4, a dark field image of TEM was shown in Figure 5. From the dark field image of TEM in Figure 5, a few bright parts that suggested the existence of nanocrystalline

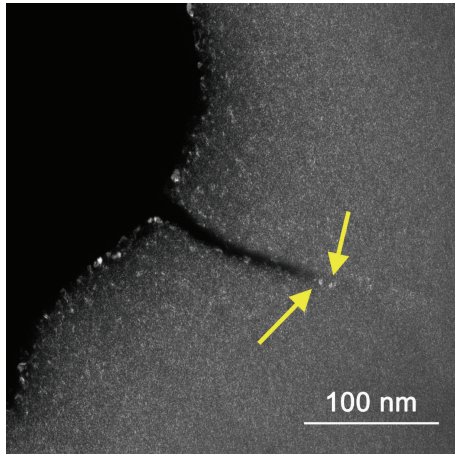


FIGURE 5: TEM dark field image of as-prepared Pd_{77.5}Cu₆Si_{16.5} metallic glass around a shear band. The bright parts indicated by the arrows within the shear band suggest the existence of crystalline phase formation.

phases could be noticed inside the shear band, at the edge of the crack and at the edge of the TEM sample. In addition, clear lattice fringes from high-resolution TEM results were also noticed for the nanocrystalline phases inside shear bands, which were not presented here. The nanocrystalline phase formation may have different originations at different parts in the sample. In this paper, we would like to focus only on the nanocrystalline phases formation inside shear bands.

Although crystalline phases inside shear bands have been reported [7–10] and studied by TEM, improper TEM sample preparation techniques may introduce artifacts, such as nanocrystalline phases, and it was also mentioned recently that some of crystalline phases observed in the deformed region were not because they were deformed but because they were thin [11]. In this paper, since the shear bands were created after TEM sample preparation, the deformed region was off artifacts and the observed crystalline phases were undoubtedly formed during the deformation. To explain the formation of the observed crystalline phases in shear bands, both the thermodynamic and the kinetic factors should be considered. Since the temperature can easily induce the crystallization transformation from MGs, temperature effect was proposed as an apparent reason for the crystallization formation inside shear bands. Although significant temperature rise has been noticed around shear off on some metallic glasses [12], it was also suggested that for a limited shear off, the temperature rise was not that important [13]. For the shear band that we created with only 13 nm in thickness on TEM thin foil sample, the shear off of the shear bands would be very limited and the shear band could be regarded as a cold one, where the thermal effect could be neglected. Another possible reason accounts for the crystalline phase formation is the mechanical deformation-induced crystallization. It was believed that a structure dilatation occurred inside shear bands during the plastic deformation [2]. Compared to the matrix region, such loosely packed regions inside shear bands would increase the mobility of local atoms [4] and would provide more possibility for structure relaxation

and therefore crystalline phase formation. Since the formed crystalline phases might interact with shear bands by local stress relaxation, the crystalline phases would affect the overall mechanical properties of MGs. The existence of crystalline phases inside shear bands was often considered as an indication of having better plasticity in MGs [8, 14, 15]. However, it depends on when the crystalline phases form. If the crystalline phases form instantly while deformation, the local stress around the newly formed crystalline phase would reduce and might not be enough to support further shear band propagation. When the external load further increases, other sites may reach the critical local stress and initial another new shear band. Since the plasticity of metallic glasses is often related to the observed multiple shear bands formation, the overall plasticity would be improved if crystalline phases formed instantly while deformation. If the crystalline phases form a while after the formation of shear bands, they would have little effect on blocking the current shear band. Then the overall plasticity might not be improved, although crystalline phases were noticed. Since the Pd_{77.5}Cu₆Si_{16.5} MG has demonstrated excellent plastic deformation ability, we believed that the crystalline phases we observed were formed instantly as the plastic deformation proceeded. As to the preferred orientation and possible defects of the crystalline phases in the shear bands of Pd_{77.5}Cu₆Si_{16.5} MG, further investigations are still carrying on.

4. Conclusions

In summary, the Pd_{77.5}Cu₆Si_{16.5} metallic glass was prepared and shear bands were created by indentation after TEM sample preparation to avoid possible prefer thinning. The dark field image of TEM showed the existence of nanocrystalline phases formation inside shear bands, where they were mainly induced by mechanical deformation but not by the thermal effect. The excellent plastic deformation ability of Pd_{77.5}Cu₆Si_{16.5} metallic glass suggested that the crystalline phases were formed instantly while deformation and then retarded the shear band propagation.

Conflict of Interests

The authors declare that there is no conflict of interests regarding the publication of this paper.

Acknowledgments

This work was supported by the National Science Foundation of China (Grant no. 51101090), the Beijing Higher Education Young Elite Teacher Project (Grand no. YETP0121), and the Scientific Research Foundation for Returned Scholars, Ministry of Education of China.

References

- [1] M. F. Ashby and A. L. Greer, "Metallic glasses as structural materials," *Scripta Materialia*, vol. 54, no. 3, pp. 321–326, 2006.

- [2] P. E. Donovan and W. M. Stobbs, "The structure of shear bands in metallic glasses," *Acta Metallurgica*, vol. 29, no. 8, pp. 1419–1436, 1981.
- [3] J. Pan, Q. Chen, L. Liu, and Y. Li, "Softening and dilatation in a single shear band," *Acta Materialia*, vol. 59, no. 13, pp. 5146–5158, 2011.
- [4] J. Bokeloh, S. V. Divinski, G. Reglitz, and G. Wilde, "Tracer measurements of atomic diffusion inside shear bands of a bulk metallic glass," *Physical Review Letters*, vol. 107, Article ID 235503, 2011.
- [5] J. Li, Z. L. Wang, and T. C. Hufnagel, "Characterization of nanometer-scale defects in metallic glasses by quantitative high-resolution transmission electron microscopy," *Physical Review B*, vol. 65, no. 14, Article ID 144201, pp. 144201–1442016, 2002.
- [6] J. Li, F. Spaepen, and T. C. Hufnagel, "Nanometre-scale defects in shear bands in a metallic glass," *Philosophical Magazine A*, vol. 82, no. 13, pp. 2623–2630, 2002.
- [7] G. Wilde and H. Rösner, "Nanocrystallization in a shear band: an in situ investigation," *Applied Physics Letters*, vol. 98, no. 25, Article ID 251904, 2011.
- [8] M. Chen, A. Inoue, W. Zhang, and T. Sakurai, "Extraordinary plasticity of ductile bulk metallic glasses," *Physical Review Letters*, vol. 96, no. 24, Article ID 245502, 2006.
- [9] G. Kumar, T. Ohkubo, T. Mukai, and K. Hono, "Plasticity and microstructure of Zr-Cu-Al bulk metallic glasses," *Scripta Materialia*, vol. 57, no. 2, pp. 173–176, 2007.
- [10] K. Wang, T. Fujita, Y. Q. Zeng, N. Nishiyama, A. Inoue, and M. W. Chen, "Micromechanisms of serrated flow in a Ni₅₀Pd₃₀P₂₀ bulk metallic glass with a large compression plasticity," *Acta Materialia*, vol. 56, no. 12, pp. 2834–2842, 2008.
- [11] A. L. Greer, Y. Q. Cheng, and E. Ma, "Shear bands in metallic glasses," *Materials Science and Engineering R*, vol. 74, pp. 71–132, 2013.
- [12] J. J. Lewandowski and A. L. Greer, "Temperature rise at shear bands in metallic glasses," *Nature Materials*, vol. 5, no. 1, pp. 15–18, 2006.
- [13] D. B. Miracle, A. Concustell, Y. Zhang, A. R. Yavari, and A. L. Greer, "Shear bands in metallic glasses: size effects on thermal profiles," *Acta Materialia*, vol. 59, no. 7, pp. 2831–2840, 2011.
- [14] K. Hajlaoui, A. R. Yavari, B. Doisneau et al., "Shear delocalization and crack blunting of a metallic glass containing nanoparticles: in situ deformation in TEM analysis," *Scripta Materialia*, vol. 54, no. 11, pp. 1829–1834, 2006.
- [15] S.-W. Lee, M.-Y. Huh, E. Fleury, and J.-C. Lee, "Crystallization-induced plasticity of Cu-Zr containing bulk amorphous alloys," *Acta Materialia*, vol. 54, no. 2, pp. 349–355, 2006.

Research Article

A Ti/Ti-Based-Metallic-Glass Interpenetrating Phase Composite with Remarkable Mutual Reinforcement Effect

J. Mu,¹ Z. W. Zhu,² H. F. Zhang,² H. W. Zhang,² H. M. Fu,²
H. Li,² A. M. Wang,² and Z. Q. Hu²

¹ Key Laboratory for Anisotropy and Texture of Materials, Northeastern University, Shenyang 110004, China

² Shenyang National Laboratory for Materials Science, Institute of Metal Research, Chinese Academy of Sciences, 72 Wenhua Road, Shenyang 110016, China

Correspondence should be addressed to H. F. Zhang; hفزhang@imr.ac.cn

Received 21 February 2014; Accepted 22 April 2014; Published 14 May 2014

Academic Editor: Limei Xu

Copyright © 2014 J. Mu et al. This is an open access article distributed under the Creative Commons Attribution License, which permits unrestricted use, distribution, and reproduction in any medium, provided the original work is properly cited.

A Ti/Ti-based-metallic-glass interpenetrating phase composite (IPC) was prepared by infiltrating the $\text{Ti}_{34.3}\text{Zr}_{31.5}\text{Ni}_{5.5}\text{Cu}_5\text{Be}_{23.7}$ melt into the porous Ti skeleton. Porous Ti limits the shear band (SB) propagation and promotes the SB multiplication, leading to the improved ductility. Moreover, the interpenetrating phase structure shows a mutual reinforcement effect for both amorphous and crystalline phases, making IPC possess higher strength than that calculated by the models held for the conventional composites. This finding will suggest a new way for preparing composites with high strength and ductility.

Bulk metallic glass composites (BMGCs) have attracted lots of attention due to the combinations of strength and ductility [1–3]. The reinforcement is usually in the shape of particles [4–6], fibers [7, 8], and so forth. It is classified into the two types of ductile and brittle one by the nature. Recently, ductile crystalline inclusions have been proven to more effectively improve the plasticity of the composites [9–18]. For example, Zr- or Ti-based Be-bearing BMGCs containing body-centered cubic (b.c.c.) dendrites exhibit more than 10% plastic strain under tension as well as high processability, which causes lots of interests worldwide [9–13]. The introduction of high volume fraction dendrites with the low strength indeed improves the ductility but apparently reduces the strength of materials, which limits their practical utility to some extent. It is challenging to prepare the BMGC with high strength and plasticity.

In this letter, an idea of interpenetrating phase composite (IPC) [19–21] was applied, which is prepared by infiltrating the melt into the prefabricated porous skeleton, to overcome this aforementioned issue. Generally speaking, the skeleton is fabricated by powder consolidation so that it is easy to achieve the microstructure as desired. The volume fraction and pore size can be controlled. Accordingly, in the IPCs, each

individual phase continuously extends in a 3D space to form a completely homogeneously interconnected network. Each amorphous unit in a nano- or microscale will present a strong size effect [22, 23], which leads to the IPC possessing higher strength. Meanwhile, good plasticity is obtained through the propagation limitation and multiplication of shear bands by the well-connected crystalline phase with a considerable volume fraction. As a result, the IPC containing amorphous phase will show high strength and ductility. Herein, we present a Ti/Ti-based-metallic-glass IPC, which exhibits the strength as high as 1740 MPa and the ductility of ~10%.

Master ingots with nominal composition of $\text{Ti}_{34.3}\text{Zr}_{31.5}\text{Ni}_{5.5}\text{Cu}_5\text{Be}_{23.7}$ (in atomic percentage) [24] were prepared by arc melting the mixture of the element metals in a Ti-getter high-purity argon atmosphere. Titanium skeleton (purity ≥ 99.9 wt.%) with a porosity of ~60% and pore size of 30~300 μm was used as the infiltration skeleton. The composites were prepared by pressure assisted infiltrating the $\text{Ti}_{34.3}\text{Zr}_{31.5}\text{Ni}_{5.5}\text{Cu}_5\text{Be}_{23.7}$ melt into the porous Ti skeleton at 1123 K. The pressure and time in the infiltrating process were about 1 MPa and 5 min, respectively. The as-prepared samples were characterized with X-ray diffraction (XRD, Philips PW1050, Cu-K α), scanning

electron microscope (SEM, Hitachi S3400N) coupled with energy dispersive spectrometer (EDS, Oxford), transmission electron microscope (TEM, JEOL 2010, 200 kV), and differential scanning calorimeter (DSC, Netzsch DSC 204 F). DSC measurements were performed in a flowing argon atmosphere at a heating rate of 40 K/min. Compression tests were conducted in an Instron 5582 universal testing machine at a strain rate of $5 \times 10^{-4} \text{ s}^{-1}$ at room temperature. Fractured samples were observed using SEM and TEM.

Figure 1(a) shows the XRD patterns of the as-prepared composite. For comparison, the XRD patterns of porous Ti skeleton used in the present work are also displayed in Figure 1(a). It can be seen that the XRD patterns of the composite are comprised of the apparent Bragg peaks, some of which are identical to those of the porous Ti. It indicates that the porous Ti is retained in the composite, which is indexed as α -Ti. Besides α -Ti, the other weak peaks are probably identified as β -Ti, of which the intensity shows that its volume fraction is quite low. Whether the amorphous phase forms or not is difficult to be recognized from the XRD patterns in Figure 1(a), because the Bragg peaks corresponding to the crystalline phases are very strong.

The existence of amorphous phase in the as-prepared sample is demonstrated by DSC measurements, as shown in Figure 1(b). DSC curves of the composite exhibit an obvious glass transition and crystallization. The specimens cut from the top and bottom of the as-prepared samples were both examined. In comparison with the DSC curve of monolithic BMG, it is found out that the composite has similar thermal characteristic temperatures as those of monolithic BMG. It is implied that the composition of the amorphous matrix in this composite is not changed largely, which will not ruin the glass forming ability of $\text{Ti}_{34.3}\text{Zr}_{31.5}\text{Ni}_{5.5}\text{Cu}_5\text{Be}_{23.7}$ (at.%) alloy. [24] That is to say, high glass forming ability of the master alloy will ensure that the composite may be prepared in large sizes. In the present work, the sample of $10 \times 40 \times 60$ mm was prepared (not shown here).

The phase distribution morphology of the as-prepared composite was observed, as shown in Figures 1(c) and 1(d). From the SEM images in Figure 1(c), it can be found out that all the pores of Ti skeleton are filled with the Ti-based metallic glass. No visible void can be seen on the interface. Careful examination of the interface between α -Ti and the amorphous phases shows the presence of a continuous transition layer with a thickness of $\sim 8 \mu\text{m}$, as shown in Figure 1(d). In the amorphous phase, some dendrites with the size $< 5 \mu\text{m}$ precipitated, as marked by the ellipses in Figure 1(d). The EDS analysis indicates that they have the similar composition, which is mainly composed of Ti and Zr, of which the contents are 85.9 at.% and 12.6 at.%, respectively. Zr is considered as an element stabilizing β -Ti solution [25]. Accordingly, it is probable that the transition layer and the precipitated dendrites should correspond to β -Ti as indicated by XRD measurements (Figure 1(a)), which is further clarified by TEM observations. Figure 1(e) shows the bright field image of TEM for the composite, clearly showing that the dendrite is embedded in the featherless matrix. The corresponding selected area electron diffraction (SAED) patterns are inset

with Figure 1(e), illustrating that the amorphous and body-centered cubic (b.c.c.) phase are for the matrix and dendrite, respectively. The interface between both the phases is shown in high resolution in Figure 1(f). It confirms that there are not any reaction products that are observed and both the phases are atomically bonded.

Mechanical properties of the as-prepared composite were measured by quasistatic compression tests. The specimens of $4 \times 4 \times 8$ mm were used. For a comparison, the compressive stress-strain curves of the porous Ti and monolithic BMG were also displayed in Figure 2(a). The porous Ti exhibits an extremely low strength and hardly fails under compressive loading. On the contrary, the monolithic BMG fractured without any plastic deformation under loading. The fracture strength is as high as about 1830 MPa. It is clear to show that the composite possesses the advantages of both materials as expected, including high strength and considerable plasticity. The yield strength, plasticity, and fracture strength are approximately 1400 MPa, 10%, and 1740 MPa for the present composite, respectively.

As reported by the previous works [6, 7, 26], the yield strength of BMGCs containing the particles and fibers of the relatively low volume fraction (i.e., $< 30\%$) still follows the rule of mixture (ROM), which is expressed as follows:

$$\sigma^c = f_\alpha \sigma^\alpha + f_\beta \sigma^\beta, \quad (1)$$

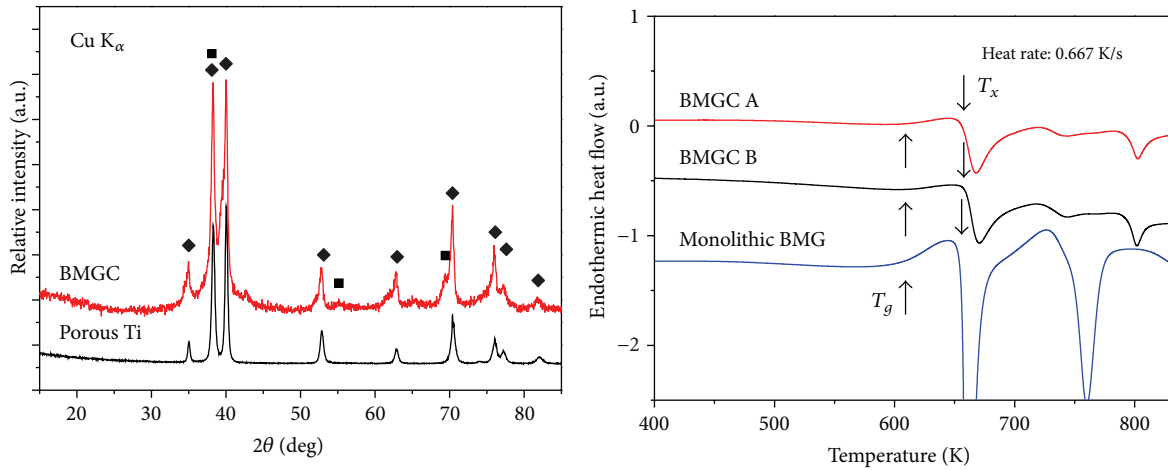
where f and σ are the volume fraction and the yield strength of the constituent phases and subscript/superscript α and β refer to the pure titanium and the BMG in the present study, respectively.

For the volume fraction of the crystalline phase more than 50% of the load-bearing model is applied to calculate the yield strength of the composite as follows [27]:

$$\sigma^c = (1 + 0.5 f_\beta) \sigma^\alpha. \quad (2)$$

Suppose that the amorphous/crystalline IPCs are the same as the conventional BMGCs and the strength is modeled as a function of volume fraction for Ti/Ti-based-metallic-glass IPCs, as shown in Figure 2(b). The mechanical parameters of the constituent phases are listed in Table 1 [24, 25]. Between those two cases, the percolation theory is applied [26, 28] as schematically illustrated by the solid line in Figure 2(b).

Apparently, it is easy to find out that the yield strength of the current composite is higher than the value calculated by about 30%, as shown in Figure 2(b). That is to say, each phase in the present composites yields at the higher stress under loading. It is believed that the enhancement effect arises from the present interpenetrating phase structure. As aforementioned, the composite is made by infiltrating Ti-based metallic melt into the porous Ti skeleton so that each phase can exhibit a 3D network structure (Figure 1(c)). Microstructurally, each local unit of one phase is surrounded by the units belonging to the other phases. A sleeve-like confinement may mutually take place for each other under loading [20, 21], which makes the phases in the composites more difficult to plastically deform. It is apparently in favor of the enhancement of the yield strength for the present



◆ α -Ti
 ■ β -Ti

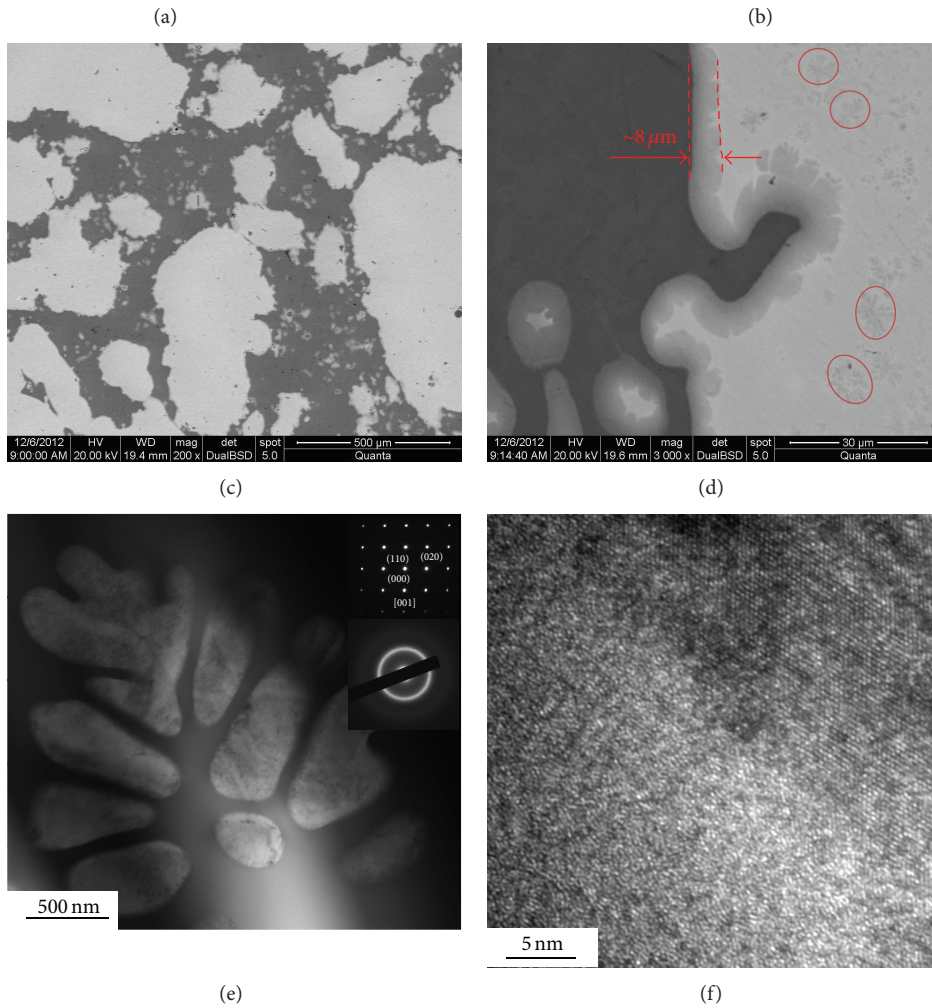


FIGURE 1: Structural characterizations of Ti/Ti-based-metallic-glass IPC. (a) XRD patterns of the composites and Ti skeleton. (b) DSC curves of the composites and monolithic BMG. (c) and (d) SEM micrographs. (e) and (f) TEM micrographs of IPC.

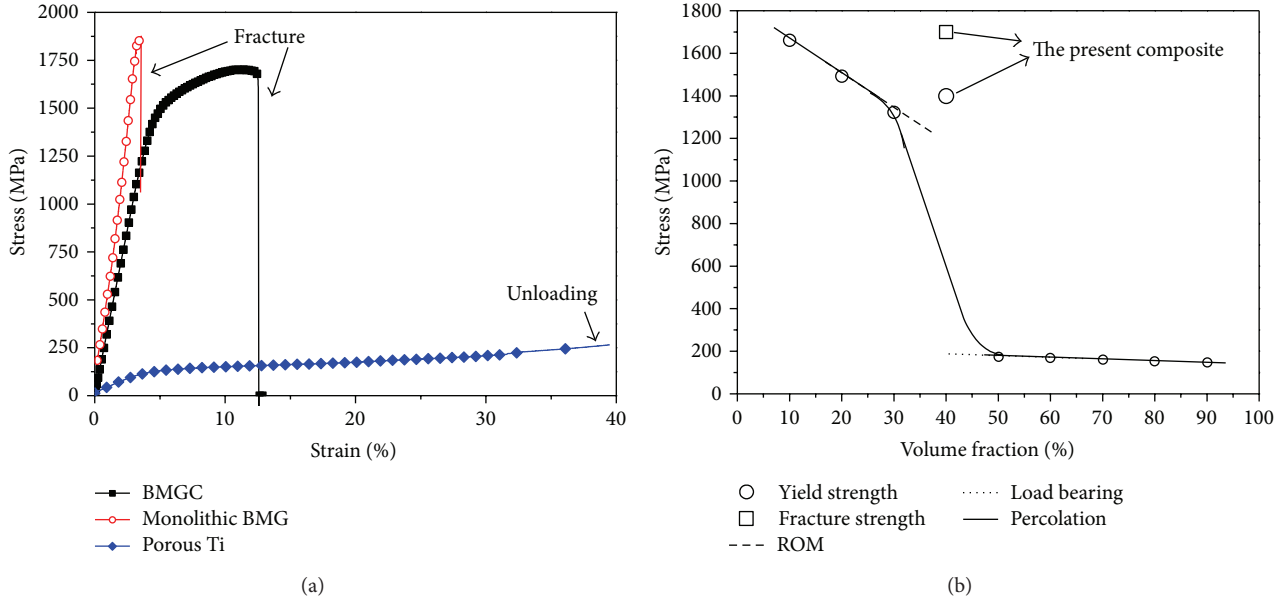


FIGURE 2: (a) Stress-strain curves of the monolithic BMG, porous Ti, and IPC and (b) comparison of experimental and calculated values of yield and fracture strength as a function of volume fraction for IPC.

TABLE 1: Density (ρ), Young modulus (E), shear modulus (G), yield strength (σ_y), and fracture strength (σ_f) of α -Ti and monolithic BMG.

	ρ (g/cm ³)	E (GPa)	G (GPa)	σ_y (MPa)	σ_f (MPa)
α -Ti	4.51	115	44	140*	235*
BMG	5.54	97.8	36.1	1830	1830

Note. *The data are measured in tension [25].

composite. On the other hand, the size effect of glassy phase should be taken into account. Different from the composites containing the reinforcement particles and fibers where the glassy phase serves as the matrix, the glassy phase is one constituent in the present composite which is hard to be defined as the matrix or the reinforcement. And the local glassy phase units have the size of less than 300 μm , some of which are on a nano- or microscale. Recent studies show that metallic glasses have a strong size effect on the strength [23]. The yield strength of Zr-Ti-Co-Be metallic glass reaches 2.25 GPa when the specimen size reduces to 100 nm [23]. From this view of aspect, the confined units of the smaller size will produce the stronger enhancement effect. These results show the presence of remarkable mutual reinforcement effect for the constituent phases in the IPC, which results in the higher strength as shown in Figure 2(b).

The interpenetrating structure simultaneously improves the plasticity. As pointed in the previous study, the introduction of ductile phase into the BMG matrix tunes the stress state in the materials, [15] which inhibits the rapid propagation of shear bands and produces the multiple shear bands. A similar mechanism takes place in the present composite. The lateral surface of the fractured specimens was observed by SEM, as shown in Figure 3(a). Multiple shear bands are clearly seen in the glassy phase. It is of no doubt that the plastic deformation firstly occurs in Ti skeleton due to its relatively low yield strength. Abundant slip bands can be

seen in the Ti skeleton as shown in the inset of Figure 3(a). The transition layer of β -Ti solution is good for the progressive deformation because it is harder than the pure Ti and softer than BMG. It will harmonize the deformation behaviors of local Ti and amorphous units. It is confirmed by the number density of slip bands or shear bands reducing from Ti skeleton to the glassy phase in the inset of Figure 3(a). Once the shear band initiates, the propagation will be inhibited by the crystalline phases. Figure 3(b) shows the dendrite arresting the shear band. This behavior makes the specimens avoid the sudden fracture due to the rapid propagation of shear bands. Shear band multiplication distributes the plastic strain, improving the plasticity.

To conclude, the present Ti/Ti-based-metallic-glass IPC exhibits advantageous properties. The sleeve-like confinement effect and size effect presented by the current continuous structure in the 3D space contribute to not only high plasticity but also high strength. It is implied that the crystalline/amorphous IPC will be served as a new way of producing BMGCs with good plasticity combined with high strength, which will promote the practical utility of BMGCs.

Conflict of Interests

The authors declare that there is no conflict of interests regarding the publication of this paper.

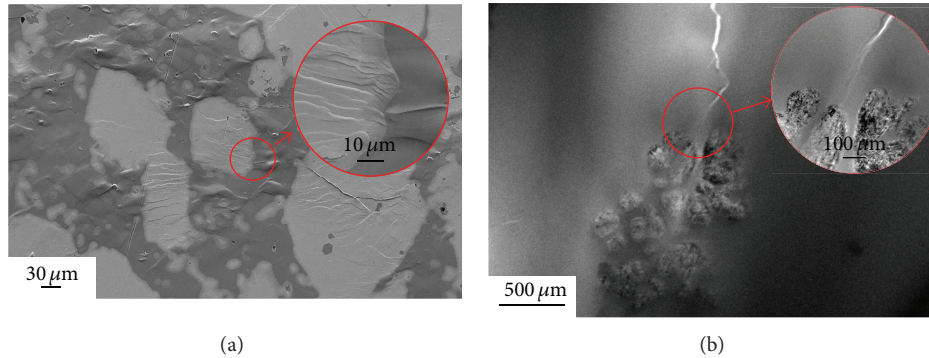


FIGURE 3: (a) SEM micrographs of the lateral surface of fractured sample showing that the crystalline phase restrains the shear band motion and gives rise to multiple shear bands in the glassy phase; (b) TEM micrographs of deformed samples showing that the precipitated crystalline phase inhibits the microcrack propagation.

Acknowledgments

The authors acknowledge the financial support from the One Hundred Person Project of the Chinese Academy of Sciences, National Basic Research Program of China (no. 2011CB606301), and the National Natural Science Foundation of China (nos. 51001097 and 51301034).

References

- [1] H. Choi-Yim, W. L. Johnson, R. D. Conner, R. B. Dandliker, and W. L. Johnson, "Bulk metallic glass matrix composites," *Applied Physics Letters*, vol. 71, pp. 3808–3810, 1997.
- [2] J. Eckert, J. Das, S. Pauly, and C. Duhamel, "Mechanical properties of bulk metallic glasses and composites," *Journal of Materials Research*, vol. 22, no. 2, pp. 285–301, 2007.
- [3] T. C. Hufnagel, C. Fan, R. T. Ott, J. Li, and S. Brennan, "Controlling shear band behavior in metallic glasses through microstructural design," *Intermetallics*, vol. 10, no. 11-12, pp. 1163–1166, 2002.
- [4] F. Szuets, C. P. Kim, and W. L. Johnson, "Mechanical properties of $Zr_{56.2}Ti_{13.8}Nb_{5.0}Cu_{6.9}Ni_{5.6}Be_{12.5}$ ductile phase reinforced bulk metallic glass composite," *Acta Materialia*, vol. 49, no. 9, pp. 1507–1513, 2001.
- [5] H. Kato, T. Hirano, A. Matsuo, Y. Kawamura, and A. Inoue, "High strength and good ductility of $Zr_{55}Al_{10}Ni_5Cu_{30}$ bulk glass containing ZRC particles," *Scripta Materialia*, vol. 43, no. 6, pp. 503–507, 2000.
- [6] H. Choi-Yim, R. Busch, U. Köster, and W. L. Johnson, "Synthesis and characterization of particulate reinforced $Zr_{57}Nb_5Al_{10}Cu_{15.4}Ni_{12.6}$ bulk metallic glass composites," *Acta Materialia*, vol. 47, no. 8, pp. 2455–2462, 1999.
- [7] R. D. Conner, R. B. Dandliker, and W. L. Johnson, "Mechanical properties of tungsten and steel fiber reinforced $Zr_{41.25}Ti_{13.75}Cu_{12.5}Ni_{10}Be_{22.5}$ metallic glass matrix composites," *Acta Materialia*, vol. 46, no. 17, pp. 6089–6102, 1998.
- [8] K. Q. Qiu, A. M. Wang, H. F. Zhang, B. Z. Ding, and Z. Q. Hu, "Mechanical properties of tungsten fiber reinforced ZrAlNiCuSi metallic glass matrix composite," *Intermetallics*, vol. 10, no. 11-12, pp. 1283–1288, 2002.
- [9] D. C. Hofmann, J.-Y. Suh, A. Wiest et al., "Designing metallic glass matrix composites with high toughness and tensile ductility," *Nature*, vol. 451, no. 7182, pp. 1085–1089, 2008.
- [10] D. C. Hofmann, J.-Y. Suh, A. Wiest, M.-L. Lind, M. D. Demetriou, and W. L. Johnson, "Development of tough, low-density titanium-based bulk metallic glass matrix composites with tensile ductility," *Proceedings of the National Academy of Sciences of the United States of America*, vol. 105, no. 51, pp. 20136–20140, 2008.
- [11] C. P. Kim, Y. S. Oh, S. Lee, and N. J. Kim, "Realization of high tensile ductility in a bulk metallic glass composite by the utilization of deformation-induced martensitic transformation," *Scripta Materialia*, vol. 65, no. 4, pp. 304–307, 2011.
- [12] J. W. Qiao, S. Wang, Y. Zhang, P. K. Liaw, and G. L. Chen, "Large plasticity and tensile necking of Zr-based bulk-metallic-glass-matrix composites synthesized by the Bridgman solidification," *Applied Physics Letters*, vol. 94, no. 15, 2009.
- [13] G. Chen, J. L. Cheng, and C. T. Liu, "Large-sized Zr-based bulk-metallic-glass composite with enhanced tensile properties," *Intermetallics*, vol. 28, pp. 25–33, 2012.
- [14] U. Kühn, J. Eckert, N. Mattern, and L. Schultz, "ZrNbCuNiAl bulk metallic glass matrix composites containing dendritic bcc phase precipitates," *Applied Physics Letters*, vol. 80, no. 14, pp. 2478–2480, 2002.
- [15] Z. Zhu, H. Zhang, Z. Hu, W. Zhang, and A. Inoue, "T-particulate reinforced Zr-based bulk metallic glass matrix composite with tensile plasticity," *Scripta Materialia*, vol. 62, no. 5, pp. 278–281, 2010.
- [16] C. Fan, R. T. Ott, and T. C. Hufnagel, "Metallic glass matrix composite with precipitated ductile reinforcement," *Applied Physics Letters*, vol. 81, no. 6, pp. 1020–1022, 2002.
- [17] Y. Wu, H. Wang, H. H. Wu et al., "Formation of Cu-Zr-Al bulk metallic glass composites with improved tensile properties," *Acta Materialia*, vol. 59, no. 8, pp. 2928–2936, 2011.
- [18] M. L. Lee, Y. Li, and C. A. Schuh, "Effect of a controlled volume fraction of dendritic phases on tensile and compressive ductility in La-based metallic glass matrix composites," *Acta Materialia*, vol. 52, no. 14, pp. 4121–4131, 2004.
- [19] D. R. Clarke, "Interpenetrating phase composites," *Journal of the American Ceramic Society*, vol. 75, no. 4, pp. 739–759, 1992.
- [20] H. F. Zhang, A. M. Wang, H. Li et al., "Quasi-static compressive property of metallic glass/porous tungsten bi-continuous phase composite," *Journal of Materials Research*, vol. 21, no. 6, pp. 1351–1354, 2006.
- [21] Y. Sun, H. F. Zhang, A. M. Wang et al., "Mg-based metallic glass/titanium interpenetrating phase composite with high

- mechanical performance," *Applied Physics Letters*, vol. 95, no. 17, pp. 171910–171913, 2009.
- [22] C. J. Lee, J. C. Huang, and T. G. Nieh, "Sample size effect and microcompression of $Mg_{65}Cu_{25}Gd_{10}$ metallic glass," *Applied Physics Letters*, vol. 91, no. 16, 2007.
- [23] D. Jang and J. R. Greer, "Transition from a strong-yet-brittle to a stronger-and-ductile state by size reduction of metallic glasses," *Nature Materials*, vol. 9, pp. 215–219, 2010.
- [24] M. Q. Tang, H. F. Zhang, Z. W. Zhu et al., "TiZr-base bulk metallic glass with over 50 mm in diameter," *Journal of Materials Science & Technology*, vol. 26, no. 6, pp. 481–486, 2010.
- [25] C. Leyens and M. Peters, *Titanium and Titanium Alloys*, Wiley Online Library, 2003.
- [26] S. Pauly, G. Liu, G. Wang et al., "Modeling deformation behavior of Cu-Zr-Al bulk metallic glass matrix composites," *Applied Physics Letters*, vol. 95, no. 10, pp. 101906–101906-3, 2009.
- [27] V. C. Nardone and K. M. Prewo, "On the strength of discontinuous silicon carbide reinforced aluminum composites," *Scripta Metallurgica*, vol. 20, no. 1, pp. 43–48, 1986.
- [28] X. L. Fu, Y. Li, and C. A. Schuh, "Mechanical properties of metallic glass matrix composites: effects of reinforcement character and connectivity," *Scripta Materialia*, vol. 56, no. 7, pp. 617–620, 2007.

Research Article

Surface Crystallization in Mg-Based Bulk Metallic Glass during Copper Mold Casting

Xin Wang

School of Material Science and Engineering, Hebei University of Technology, Dingzigu Road, Hongqiao District, Tianjin 300130, China

Correspondence should be addressed to Xin Wang; ahaxin@126.com

Received 21 March 2014; Accepted 18 April 2014; Published 6 May 2014

Academic Editor: Yang Shao

Copyright © 2014 Xin Wang. This is an open access article distributed under the Creative Commons Attribution License, which permits unrestricted use, distribution, and reproduction in any medium, provided the original work is properly cited.

The localized crystallization of $\text{Mg}_{54}\text{Cu}_{28}\text{Ag}_7\text{Y}_{11}$ bulk metallic glass (BMG) in the injection casting process using a copper mold was investigated. It has been found that several crystalline phases were formed close to the as-cast surface but did not exist in the internal part of the BMG plate. It is abnormal that the as-cast surface is partially crystallized with higher cooling rate than that of inside. Overheating of the melt and nucleation induced by the surface of copper mold play key roles in the abnormal crystallization. It is suggested that the function of copper mold to trigger heterogeneous nucleation cannot be totally ignored, although it provides the high cooling rate for the glass formation during casting.

1. Introduction

Bulk metallic glass (BMG) has attracted much attention since the rapid cooling solidification technology was developed which mainly includes melt quenching, fluxing, and copper mold casting [1–4]. The unique structure of metallic glass (MG) formed by rapid cooling solidification endows this new comer of metal materials many special properties such as good compression ductility, high corrosion resistance, good wear resistance, and special functional properties [5–14]. In general, BMG is fabricated by quenching the melt without incurring crystallization. Therefore, the forming of MG is determined by the inherent glass forming ability (GFA) of the alloy itself and the preparation conditions. Meanwhile, the GFA of one alloy is the major factor to control the thermal stability of the glass forming liquid. The other factor, which is related to the preparation technologies, also plays an important role to obtain full amorphous structure frozen from the melt.

Mg-based BMG is one-kind lightweight amorphous alloy, few in amount, which possesses both good GFA and low density. Inoue et al. [15] firstly discovered the $\text{Mg}_{65}\text{Cu}_{25}\text{Y}_{10}$ BMG in 1991. Next, Park et al. [16] investigated the effect of Ag substitution for Cu and improved the critical diameter (D_c) for amorphous phase formation from 4 mm to 6 mm. Ma et al.

[17, 18] optimized the composition of Mg-Cu-Y ternary alloy and Mg-Cu-Ag-Y quaternary alloy, improving the D_c values to 9 mm and 16 mm, respectively. Up to date, this class of BMG can be made into 27 mm [19] and can be significantly toughened by ex situ addition of some second phases [20, 21]. Therefore, Mg-based BMG and composites have been regarded as promising materials for engineering application. It is necessary to investigate the processing properties of this BMG alloy system.

In the present work, $\text{Mg}_{54}\text{Cu}_{28}\text{Ag}_7\text{Y}_{11}$ alloy [18] was selected as the experimental material to investigate the casting formability of typical Mg-based BMG. The crystallization related to the cast technology aspect will be discussed.

2. Experimental

The raw materials with purity better than 99.9% were used to fabricate the BMG alloy. An intermediate alloy with the nominal composition $\text{Cu}_{28}\text{Ag}_7\text{Y}_{11}$ was firstly prepared by arc melting method under a Ti-gettered argon atmosphere. This intermediate alloy was then melted with Mg pieces by induction melting under inert atmosphere to obtain a master alloy with the nominal composition $\text{Mg}_{54}\text{Cu}_{28}\text{Ag}_7\text{Y}_{11}$. Subsequently, the master alloy was then remelted in the quartz

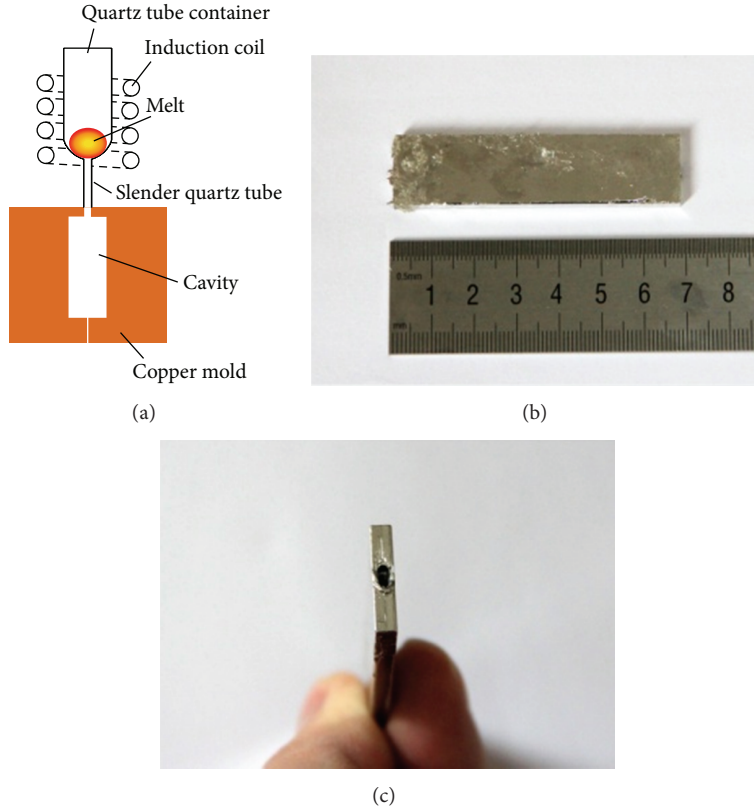


FIGURE 1: (a) Schematic diagram of the applied injection casting, (b) image of the BMG plate, and (c) top view of the plate.

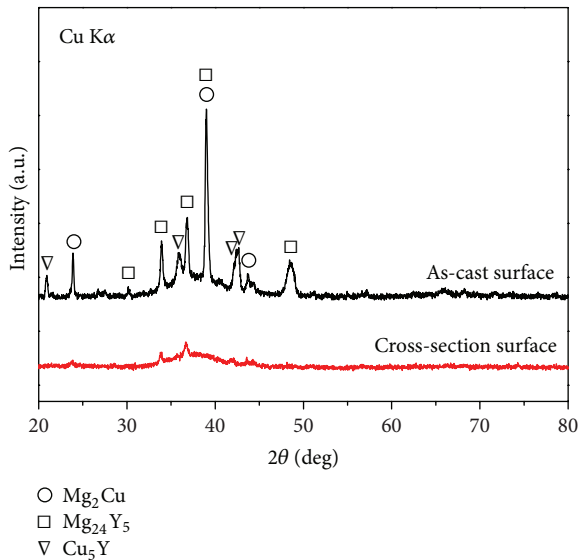


FIGURE 2: XRD spectra of the $Mg_{54}Cu_{28}Ag_7Y_{11}$ plate for different parts.

tubes using induction melting and injected into the copper mold which had an internal plate-shaped cavity of about $3 \times 14 \times 70$ mm in size. The applied injection casting method was optimized by Xie et al. [22] as shown in Figure 1(a). A slender quartz tube was placed between the quartz tube

(melt container) and the mold to keep gas impermeability for improving the mold-filling capacity.

The as-cast BMG sample was examined by X-ray diffraction (XRD) analysis using Rigaku D/max-RB XRD spectrometry with $Cu\ K\alpha$ radiation. The thermal stability of the as-cast BMG sample was measured by differential scanning calorimeter (DSC, TA Instruments) at a constant heating rate of 20 K/min. The surface morphology was investigated by a LEO1530 scanning electron microscope (SEM) with a field emission gun. The composition of the BMG samples was examined by energy dispersive X-ray spectroscopy (EDS).

3. Results and Discussion

Figure 1 shows the pictures of one cast plate together with the schematic diagram of the applied injection casting. The as-cast plate has a perfect shape which completely matches the cavity size of the copper mold as shown in Figures 1(b) and 1(c). The good mold-filling capacity is attributed to the following two aspects: the good gas impermeability and a higher cast temperature of the melt. The good gas impermeability is favorable for improving the pressure of the melt during filling in the mold. Overheating is beneficial for improving the fluidity of the melt. These two aspects collaboratively work, resulting in significant improvement of mold-filling capacity.

Figure 2 shows the XRD spectra of the as-cast surface and the cross-section surface of the $Mg_{54}Cu_{28}Ag_7Y_{11}$ alloy plate.

It was found that the spectrum of the as-cast surface has many sharp peaks corresponding to the crystalline phases such as Mg_2Cu , $Mg_{24}Y_5$ and Cu_5Y . However, for the cross-section, the intensities of the crystalline phase peaks are much lower than that of the as-cast surface. It was demonstrated that the amount of crystalline phase in the cross-section surface is smaller than that of the as-cast surface. Moreover, one typical amorphous structure feature, the hump-like diffuse scattering peak, can be identified as existing on the spectrum of the cross-section surface. It is then suggested that the plate contains certain amount of amorphous phase. As we speculated, the crystalline phases might be precipitated in the as-cast surface in contact with the copper mold.

The as-cast sample, which has been examined by XRD in Figure 2, was grinded using sandpaper and hereafter reexamined to confirm whether the crystallization partially occurs on the surface. After wearing off ~ 0.1 mm and ~ 0.2 mm from the as-cast surface, the sample was rescanned by XRD, respectively. Figure 3 displays the XRD spectra of the sample with different wear depths. It shows that the intensities of the crystalline phase peaks are decreased with the increased wear depth. Moreover, the sample is found to be composed of full amorphous structure after wearing off ~ 0.2 mm. The inset of Figure 3 shows the DSC curve of the sample after wearing. It possesses a typical glass transition followed by an obvious crystallization process which is consistent with the result in the earlier work [18]. It is demonstrated again that the centre part of the as-cast plate possesses a full amorphous structure.

Figure 4 shows a typical backscattered electron image of the sample after wearing off ~ 0.1 mm in depth. It is clearly observed that some phases, with simple geometric shapes such as triangle, quadrilateral, and hexagon, are existing on the worn surface which is near the as-cast surface. A further examination on these polygon phases by EDX proved that they are all Cu-rich and Y-rich. The ratio of Cu and Y in atom is less than 6 : 1. It is considered that, by combining this result with the XRD spectra shown in Figure 2, this phase may be Cu_5Y , a common compound in ternary Mg-Cu-Y alloys. The investigation result shown in Figure 4 agrees well with the discovery in a very recent work by Mezbahul-Islam and Medraj [23]. They reported on the phase formation in the ternary Mg-Cu-Y system, revealing that the metallographic shapes of the phases with Cu-rich and Y-rich have small plane features as well as simple geometric shapes.

For copper mold casting, it has been reported that the cooling rate is decreased with the increased diameter size. In other words, the center of a rod or plate should have relatively lower cooling rates which negatively affect the glass forming. Therefore, the crystallization is mostly identified in the center region [24, 25]. However, the crystallization in the present work is quite different: the major crystalline phases are all segregation on the as-cast surface where the cooling rate is relatively higher. It is thus suggested that the copper mold does not completely play a single role to supply the high cooling rate for glass formation.

The possible reason of the abnormal crystallization may be attributed to the two following aspects. The first one is that the GFA of the $Mg_{54}Cu_{28}Ag_7Y_{11}$ alloy is decreased by some preparation technologies such as the cast temperature

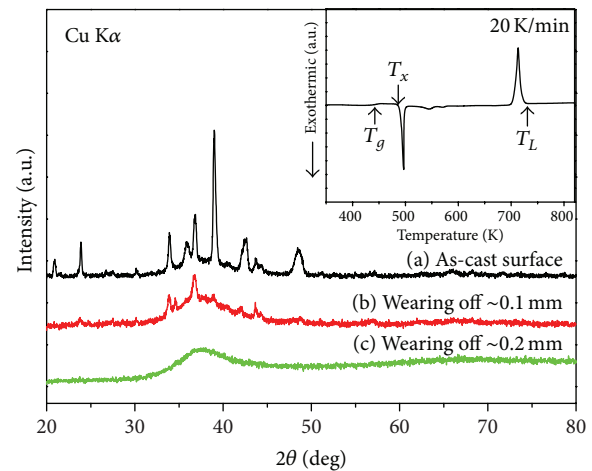


FIGURE 3: XRD spectra of the $Mg_{54}Cu_{28}Ag_7Y_{11}$ plate with different surface treatments. The inset is the DSC curve of the sample after wearing off the crystalline surface.

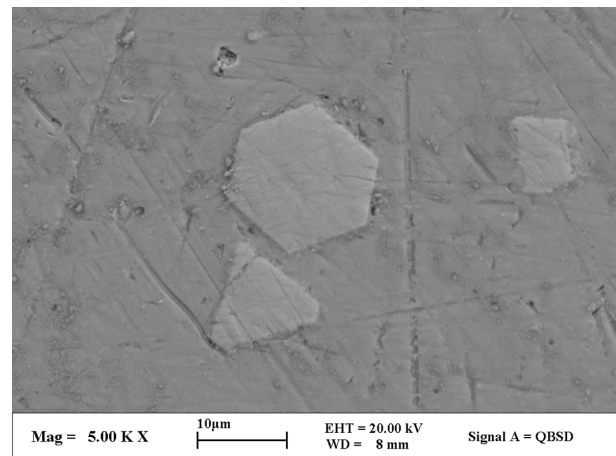


FIGURE 4: Typical BSE image of some crystalline phases near the as-cast surface.

and the use of quartz tube. It is known that overheating of the melt significantly affects the GFA of BMG [26]. In this work, a higher cast temperature together with a high Ar pressure of $\sim 10^5$ Pa was applied to improve the fluidity of the melt to fill the mold. Moreover, in the $Mg_{54}Cu_{28}Ag_7Y_{11}$ alloy, the melt point and boiling point of Mg are both low; thus the Mg atoms in the overheating melt are energetic and active. It is then become harder that the atoms should be frozen into an amorphous solid. Thus, the GFA of the $Mg_{54}Cu_{28}Ag_7Y_{11}$ alloy may be decreased by the high casting temperature. In addition, the quartz tube can react with Mg melt, resulting in the reduction of Mg content. Therefore, the actual composition of the BMG plate may be changed deviating from the nominal composition which has the best GFA in this quaternary alloy system. The second aspect is related to the copper mold. In our opinion, the copper mold not only provides the high cooling rate during casting, but

also supplies many favorable sites for heterogeneous nucleation. These both aspects mentioned above might jointly work during the injection casting process, resulting in the apparently abnormal surface crystallization.

4. Conclusions

In the present work, the $Mg_{54}Cu_{28}Ag_7Y_{11}$ bulk metallic glass plate was obtained by an injection casting method using copper mold. It has been found that several crystalline phases were formed close to the as-cast surface but did not exist in the internal part of the plate. The surface crystallization is attributed to the overheating of the melt and nucleation induced by the surface of copper mold. It is demonstrated that the function of copper mold to trigger heterogeneous nucleation cannot be totally ignored, although it provides the high cooling rate for glass formation during the casting.

Conflict of Interests

The author declares that there is no conflict of interests regarding the publication of this paper.

References

- [1] A. L. Greer, "Metallic glasses," *Science*, vol. 267, no. 5206, pp. 1947–1953, 1995.
- [2] H. W. Kui, A. L. Greer, and D. Turnbull, "Formation of bulk metallic glass by fluxing," *Applied Physics Letters*, vol. 45, no. 6, pp. 615–616, 1984.
- [3] W. Klement, R. H. Willens, and P. Duwez, "Non-crystalline structure in solidified gold-silicon alloys," *Nature*, vol. 187, no. 4740, pp. 869–870, 1960.
- [4] A. Inoue, T. Zhang, and T. Masumoto, "Production of amorphous cylinder and sheet of $La_{55}Al_{25}Ni_{20}$ alloy by a metallic mold casting method," *Materials Transactions JIM*, vol. 31, no. 5, pp. 425–428, 1990.
- [5] K. F. Yao, F. Ruan, Y. Q. Yang, and N. Chen, "Superductile bulk metallic glass," *Applied Physics Letters*, vol. 88, no. 12, Article ID 122106, 2006.
- [6] K. F. Yao and C. Q. Zhang, "Fe-based bulk metallic glass with high plasticity," *Applied Physics Letters*, vol. 90, no. 6, Article ID 061901, 2007.
- [7] X. Wang, Y. Shao, and K. F. Yao, "Chemical composition dependence of atomic oxygen erosion resistance in Cu-rich bulk metallic glasses," *Chinese Science Bulletin*, vol. 57, no. 36, pp. 4801–4804, 2012.
- [8] C. A. Schuh, T. C. Hufnagel, and U. Ramamurty, "Mechanical behavior of amorphous alloys," *Acta Materialia*, vol. 55, no. 12, pp. 4067–4109, 2007.
- [9] A. L. Greer, K. L. Rutherford, and I. M. Hutchings, "Wear resistance of amorphous alloys and related materials," *International Materials Reviews*, vol. 47, no. 2, pp. 87–112, 2002.
- [10] N. Chen, R. Frank, N. Asao et al., "Formation and properties of Au-based nanograined metallic glasses," *Acta Materialia*, vol. 59, no. 16, pp. 6433–6440, 2011.
- [11] S. J. Pang, T. Zhang, K. Asami, and A. Inoue, "Synthesis of Fe-Cr-Mo-C-B-P bulk metallic glasses with high corrosion resistance," *Acta Materialia*, vol. 50, no. 3, pp. 489–497, 2002.
- [12] P. Gong, K. F. Yao, and Y. Shao, "Lightweight Ti-Zr-Be-Al bulk metallic glasses with improved glass-forming ability and compressive plasticity," *Journal of Non-Crystalline Solids*, vol. 358, pp. 2620–2625, 2012.
- [13] P. Gong, K. F. Yao, and Y. Shao, "Effects of Fe addition on glass-forming ability and mechanical properties of Ti-Zr-Be bulk metallic glass," *Journal of Alloys and Compounds*, vol. 536, pp. 26–29, 2012.
- [14] X. Wang, Y. Shao, P. Gong, and K. F. Yao, "Effect of thermal cycling on the mechanical properties of $Zr_{41}Ti_{14}Cu_{12.5}Ni_{10}Be_{22.5}$ alloy," *Science China-Physics Mechanics & Astronomy*, vol. 55, no. 12, pp. 2357–2361, 2012.
- [15] A. Inoue, A. Kato, T. Zhang, S. G. Kim, and T. Masumoto, "Mg-Cu-Y amorphous alloys with high mechanical strengths produced by a metallic mold casting method," *Materials Transactions JIM*, vol. 32, no. 7, pp. 609–616, 1991.
- [16] E. S. Park, H. G. Kang, W. T. Kim, and D. H. Kim, "Effect of Ag addition on the glass-forming ability of Mg-Cu-Y metallic glass alloys," *Journal of Non-Crystalline Solids*, vol. 279, no. 2-3, pp. 154–160, 2001.
- [17] H. Ma, Q. Zheng, J. Xu, Y. Li, and E. Ma, "Doubling the critical size for bulk metallic glass formation in the Mg-Cu-Y ternary system," *Journal of Materials Research*, vol. 20, no. 9, pp. 2252–2255, 2005.
- [18] H. Ma, L. L. Shi, J. Xu, Y. Li, and E. Ma, "Discovering inch-diameter metallic glasses in three-dimensional composition space," *Applied Physics Letters*, vol. 87, no. 18, Article ID 181915, pp. 1–3, 2005.
- [19] Q. Zheng, J. Xu, and E. Ma, "High glass-forming ability correlated with fragility of Mg-Cu(Ag)-Gd alloys," *Journal of Applied Physics*, vol. 102, no. 11, Article ID 113519, 2007.
- [20] J. S. C. Jang, S. R. Jian, T. H. Li, J. C. Huang, C. Y. A. Tsao, and C. T. Liu, "Structural and mechanical characterizations of ductile Fe particles-reinforced Mg-based bulk metallic glass composites," *Journal of Alloys and Compounds*, vol. 485, no. 1-2, pp. 290–294, 2009.
- [21] J. S. C. Jang, Y. S. Chang, T. H. Li, P. J. Hsieh, J. C. Huang, and C. Y. A. Tsao, "Plasticity enhancement of $Mg_{58}Cu_{28.5}Gd_{11}Ag_{2.5}$ based bulk metallic glass composites dispersion strengthened by Ti particles," *Journal of Alloys and Compounds*, vol. 504, no. 1, pp. S102–S105, 2010.
- [22] K. F. Xie, K. F. Yao, T. Y. Huang, and W. G. Liu, "A convenient and controllable induction melt-injection casting device under high vacuum," CN ZL200920110116.5, 2009.
- [23] M. Mezbahul-Islam and M. Medraj, "Phase equilibrium in Mg-Cu-Y," *Scientific Reports*, vol. 3, p. 3033, 2013.
- [24] A. Gebert, U. Wolff, A. John, and J. Eckert, "Corrosion behaviour of $Mg_{65}Y_{10}Cu_{25}$ metallic glass," *Scripta Materialia*, vol. 43, no. 3, pp. 279–283, 2000.
- [25] P. Gong, X. Wang, Y. Shao, N. Chen, X. Liu, and K. F. Yao, "A Ti-Zr-Be-Fe-Cu bulk metallic glass with superior glass-forming ability and high specific strength," *Intermetallics*, vol. 43, pp. 177–181, 2013.
- [26] K. F. Xie, K. F. Yao, and T. Y. Huang, "Influence of the melting temperature on the fabrication of a Ti-Cu-Zr-Ni-Sn bulk metallic glass," *Materials Science Forum*, vol. 688, pp. 413–418, 2011.

Research Article

A Centimeter-Sized Quaternary Ti-Zr-Be-Ag Bulk Metallic Glass

S. F. Zhao, Y. Shao, P. Gong, and K. F. Yao

School of Materials Science and Engineering, Tsinghua University, Beijing 100084, China

Correspondence should be addressed to K. F. Yao; kfyao@tsinghua.edu.cn

Received 17 March 2014; Accepted 11 April 2014; Published 28 April 2014

Academic Editor: Na Chen

Copyright © 2014 S. F. Zhao et al. This is an open access article distributed under the Creative Commons Attribution License, which permits unrestricted use, distribution, and reproduction in any medium, provided the original work is properly cited.

A novel centimeter-sized Ti-based bulk metallic glass (BMG) was developed by the addition of Ag in the ternary $\text{Ti}_{41}\text{Zr}_{25}\text{Be}_{34}$ glassy alloy. By replacing Be with Ag, the glass forming ability (GFA), the yield strength, and the supercooled liquid temperature of the quaternary $\text{Ti}_{41}\text{Zr}_{25}\text{Be}_{34-x}\text{Ag}_x$ ($x = 2, 4, 6, 8$ at.%) glassy alloys have been obviously enhanced. Among the developed Ti-Zr-Be-Ag alloy systems, the $\text{Ti}_{41}\text{Zr}_{25}\text{Be}_{28}\text{Ag}_6$ alloy possesses the largest critical diameter (D_{\max}) of 10 mm, while the yield strength is also enhanced to 1961 MPa, which is much larger than that of $\text{Ti}_{41}\text{Zr}_{25}\text{Be}_{34}$ (1755 MPa) alloy. The experimental results show that Ag is an effective element for improving the GFA and the yield strength of Ti-Zr-Be glassy alloy.

1. Introduction

Ti-based BMGs have been under intense investigation for many years, owing to their excellent properties, such as low density, high strength, high specific strength, low elastic modulus, and strong corrosion resistance [1–4]. Moreover, the low cost makes the Ti-based BMGs a profound application prospect. Up to date, a number of Ti-based BMGs have been synthesized by the copper mold casting method [5–7]. However, compared with other alloy systems, the GFA of most Ti-based BMGs is relatively low [8, 9]. Therefore, it should be of scientific and technological interest to develop Ti-based BMGs with large GFA, together with good mechanical properties. Furthermore, introducing new elements, or so-called “alloying,” is proved to be an effective method to improve the GFA of alloys [8, 9], which makes the developing of Ti-based BMGs with better GFA and less components more challenging.

It is known that $\text{Ti}_{41}\text{Zr}_{25}\text{Be}_{34}$ ternary BMG possesses a critical size of 5 mm which is larger than other Ti-Zr-Be ternary alloys [6, 10]. In the previous work, it shows that its GFA and mechanical properties could be improved through alloying with suitable elements [11, 12]. In this paper, Ag element has been selected as an addition element in the Ti-Zr-Be alloy system. By replacing Be with Ag, a series of BMGs with the composition of $\text{Ti}_{41}\text{Zr}_{25}\text{Be}_{34-x}\text{Ag}_x$ ($x = 2, 4, 6, 8$), which have improved GFA and mechanical properties, have been obtained.

2. Experimental Procedure

The master alloy ingots with nominal compositions of $\text{Ti}_{41}\text{Zr}_{25}\text{Be}_{34-x}\text{Ag}_x$ ($x = 2, 4, 6, 8$ at.%) were prepared by arc-melting the mixtures of high-purity Ti, Zr, Be, and Ag metals in a Ti-gettered high-purity Ar atmosphere. The purity of Be and Ag metals is over 99.99% in weight, while that of Ti and Zr metals is 99.4% and 99.7% in weight, respectively. Each ingot was flipped and remelted four times to ensure the homogeneity. Cylindrical rods with different diameters were prepared by copper mold casting method.

The structure of the as-prepared samples was examined by X-ray diffraction (XRD) using $\text{Cu K}\alpha$ radiation. The thermal stability of the glassy samples was evaluated by differential scanning calorimeter (DSC) at a heating rate of 20 K/min. Compression tests were carried out on a WDW-100 testing machine under a strain rate of $4.2 \times 10^{-4} \text{ s}^{-1}$. The test samples were cut out from the as-cast $\Phi 2$ mm rods with gage aspect ratio of 2:1. For the compression tests, at least 3 samples of each glassy alloy were tested. The density ρ of each glassy alloy was measured by Archimedes' principle in the deionized water.

3. Results

Figure 1 presents X-ray diffraction spectra of the as-cast $\text{Ti}_{41}\text{Zr}_{25}\text{Be}_{34-x}\text{Ag}_x$ BMG samples ($x = 2, 4, 6, 8$ at.%) with the critical diameters. The typical broad halo patterns for

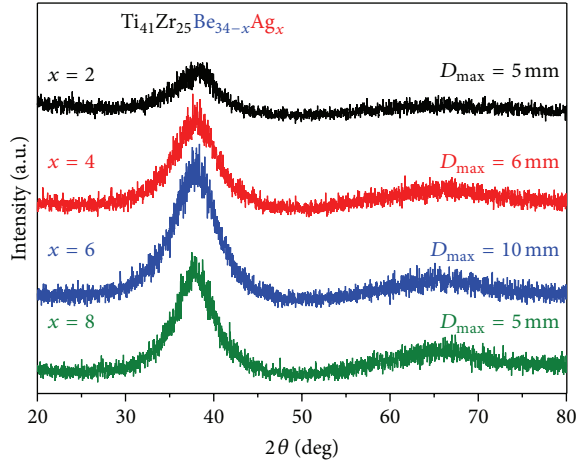


FIGURE 1: XRD patterns for the $\text{Ti}_{41}\text{Zr}_{25}\text{Be}_{34-x}\text{Ag}_x$ ($x = 2, 4, 6, 8$ at.%) glassy alloy system with their critical diameters.

the amorphous phases were observed in each XRD spectrum, and no sharp diffraction peaks corresponding to the crystalline phases could be observed. Figure 1 indicates that, with the proper addition of Ag, the GFA of the $\text{Ti}_{41}\text{Zr}_{25}\text{Be}_{34}$ alloy has been obviously improved. Meanwhile, the optimized addition content of Ag is about 6 at.%, since its critical diameter for forming fully amorphous structure is 10 mm. As the content of Ag increased to 8 at.%, the critical diameter of the $\text{Ti}_{41}\text{Zr}_{25}\text{Be}_{26}\text{Ag}_8$ alloy returns to 5 mm, which is the same as that of $\text{Ti}_{41}\text{Zr}_{25}\text{Be}_{34}$ alloy [6]. The experimental results indicate that Ag is an effective alloying element for improving the GFA of Ti-Zr-Be alloys. In present work, a new centimeter scale quaternary BMG with the nominal composition $\text{Ti}_{41}\text{Zr}_{25}\text{Be}_{28}\text{Ag}_6$ has been developed. According to some reported results [13, 14], this is the second quaternary centimeter-diameter Ti-based BMG.

Figure 2 shows the DSC curves of the sample cut out from the as-cast fully glassy $\text{Ti}_{41}\text{Zr}_{25}\text{Be}_{34-x}\text{Ag}_x$ ($x = 2, 4, 6, 8$ at.%) rods with a diameter of 2 mm. Thermodynamic parameters were measured from the DSC scans, while the glass transition temperature T_g , initial crystallization temperature T_x , and liquidus temperature T_l were marked with arrows in Figure 2. In addition, for evaluating the GFA of the $\text{Ti}_{41}\text{Zr}_{25}\text{Be}_{34-x}\text{Ag}_x$ alloys, the supercooled liquid region ΔT_x (defined as $T_x - T_g$), γ parameter (defined as $T_x/(T_g + T_l)$), and reduced glass transition temperature T_{rg} (defined as T_g/T_l) [15] were calculated as listed in Table 1.

From Figure 2, it can be found that, with the addition of Ag, T_g decreases from 607 K for $\text{Ti}_{41}\text{Zr}_{25}\text{Be}_{34}$ [6] alloy to 589 K for $\text{Ti}_{41}\text{Zr}_{25}\text{Be}_{30}\text{Ag}_2$ and $\text{Ti}_{41}\text{Zr}_{25}\text{Be}_{30}\text{Ag}_4$ alloy and then slightly increases to 597 K for $\text{Ti}_{41}\text{Zr}_{25}\text{Be}_{28}\text{Ag}_6$ alloy and 593 K for $\text{Ti}_{41}\text{Zr}_{25}\text{Be}_{26}\text{Ag}_8$ alloy, respectively. T_x increases from 656 K for $\text{Ti}_{41}\text{Zr}_{25}\text{Be}_{34}$ [6] alloy to 670 K for $\text{Ti}_{41}\text{Zr}_{25}\text{Be}_{28}\text{Ag}_6$ alloy and then decreases to 654 K for $\text{Ti}_{41}\text{Zr}_{25}\text{Be}_{26}\text{Ag}_8$ alloy. It should be noted that, with Ag addition, the value of ΔT_x has been obviously enlarged; especially, $\text{Ti}_{41}\text{Zr}_{25}\text{Be}_{30}\text{Ag}_4$ glass alloy has the largest supercooled liquid region of 81 K in the Ti-Zr-Be-Ag alloy system. ΔT_x

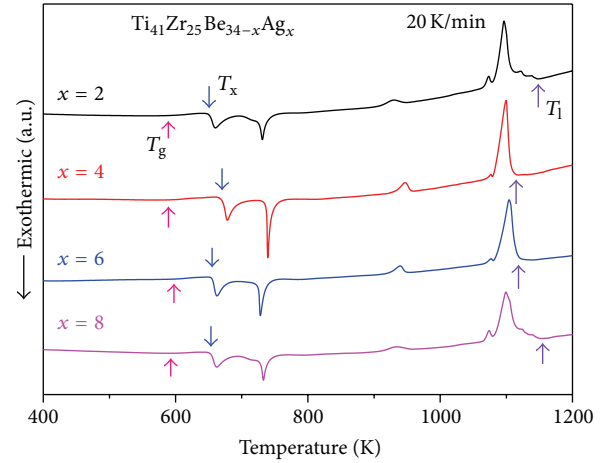


FIGURE 2: DSC curves of the $\text{Ti}_{41}\text{Zr}_{25}\text{Be}_{34-x}\text{Ag}_x$ ($x = 2, 4, 6, 8$ at.%) glassy alloys.

is considered as a measure to evaluate the thermal stability related to supercooled liquid stability against crystallization [16]; thus Ag addition can effectively improve the thermal stability of the Ti-Zr-Be-Ag glassy alloy. Moreover, the variation tendency of T_{rg} and γ with the Ag content in the alloy is roughly the same. The value of T_{rg} for $\text{Ti}_{41}\text{Zr}_{25}\text{Be}_{28}\text{Ag}_6$ alloy is the largest among all the Ti-Zr-Be-Ag alloys, and $\text{Ti}_{41}\text{Zr}_{25}\text{Be}_{30}\text{Ag}_4$ alloy possesses the largest γ value and the lowest T_l value. It is suggested that these two alloys may possess relatively good GFA [16], which is in accordance with the experimental results.

Figure 3 shows the compressive stress-strain curves of $\text{Ti}_{41}\text{Zr}_{25}\text{Be}_{34-x}\text{Ag}_x$ ($x = 2, 4, 6, 8$ at.%) at room temperature. The yield strength $\sigma_{0.2}$, the maximum compression stress σ_{max} , and the plastic strain ϵ_p of the $\text{Ti}_{41}\text{Zr}_{25}\text{Be}_{34-x}\text{Ag}_x$ BMGs were listed in Table 2. In the present work, the addition of Ag enhances the density of Ti-Zr-Be alloy, while the value of the specific strength (defined as yield strength/density) of $\text{Ti}_{41}\text{Zr}_{25}\text{Be}_{34-x}\text{Ag}_x$ ($x = 2, 4, 5, 6, 8$) BMGs does not change a lot. According to the reported results, the Ag-free alloy exhibits a yield strength $\sigma_{0.2}$ of 1755 MPa, a maximum compressive strength σ_{max} of 1914 MPa, and a plastic strain ϵ_p of 2.9% [6]. As shown in Figure 3, Ag addition can greatly increase the yield strength of the BMGs.

For the glassy alloy with optimum Ag content of 6 at.%, the yield strength $\sigma_{0.2}$ is 1964 MPa, while with 8 at.% of Ag, the maximum compression stress σ_{max} and plastic strain ϵ_p are 2054 MPa and 4.8%, respectively. The present results indicate that Ag addition could effectively improve the mechanical properties of Ti-Zr-Be glassy alloys.

It shows that, among the quaternary Ti-Zr-Be-Ag alloy system, $\text{Ti}_{41}\text{Zr}_{25}\text{Be}_{28}\text{Ag}_6$ glassy alloy possesses not only the largest GFA, but also high strength and good compressive plastic strain.

4. Discussion

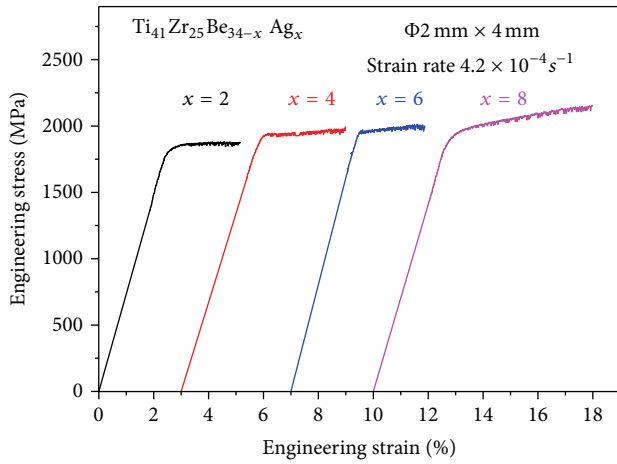
It is known that the mixing enthalpies ΔH_{mix} between Ti-Ag, Ti-Zr, Zr-Ag, Ti-Be, Ag-Be, and Zr-Be are -2 kJ/mol,

TABLE 1: Thermal parameters of $\text{Ti}_{41}\text{Zr}_{25}\text{Be}_{34-x}\text{Ag}_x$ ($x = 2, 4, 6, 8$ at.%) BMGs. The error of the temperature values is ± 1 K.

Composition (at.%)	T_g (K)	T_x (K)	ΔT_x (K)	T_l (K)	$T_{rg} = T_g/T_l$	γ	D_{\max} (mm)
$\text{Ti}_{41}\text{Zr}_{25}\text{Be}_{34}$ [6]	607	656	49	1123	0.5405	0.3792	$\Phi 5$
$\text{Ti}_{41}\text{Zr}_{25}\text{Be}_{32}\text{Ag}_2$	589	651	62	1148	0.5131	0.3748	$\Phi 5$
$\text{Ti}_{41}\text{Zr}_{25}\text{Be}_{30}\text{Ag}_4$	589	670	81	1107	0.5321	0.3950	$\Phi 6$
$\text{Ti}_{41}\text{Zr}_{25}\text{Be}_{28}\text{Ag}_6$	597	655	58	1118	0.5340	0.3819	$\Phi 10$
$\text{Ti}_{41}\text{Zr}_{25}\text{Be}_{26}\text{Ag}_8$	593	654	61	1153	0.5143	0.3746	$\Phi 5$

TABLE 2: Densities and mechanical properties of $\text{Ti}_{41}\text{Zr}_{25}\text{Be}_{34-x}\text{Ag}_x$ ($x = 2, 4, 6, 8$ at.%) BMGs.

Composition (at.%)	Density (g/cm^3)	$\sigma_{0.2}$ (MPa)	σ_{\max} (MPa)	ϵ_p (%)	Specific strength (Nm/Kg)
$\text{Ti}_{41}\text{Zr}_{25}\text{Be}_{34}$ [6]	4.76	1755	1914	2.9 ± 0.1	3.69×10^5
$\text{Ti}_{41}\text{Zr}_{25}\text{Be}_{32}\text{Ag}_2$	5.01	1808	1882	2.4 ± 0.1	3.61×10^5
$\text{Ti}_{41}\text{Zr}_{25}\text{Be}_{30}\text{Ag}_4$	5.13	1931	1995	2.9 ± 0.1	3.76×10^5
$\text{Ti}_{41}\text{Zr}_{25}\text{Be}_{28}\text{Ag}_6$	5.27	1961	2013	2.3 ± 0.1	3.73×10^5
$\text{Ti}_{41}\text{Zr}_{25}\text{Be}_{26}\text{Ag}_8$	5.42	1946	2054	4.8 ± 0.1	3.59×10^5

FIGURE 3: Compressive stress-strain curves at room temperature for $\text{Ti}_{41}\text{Zr}_{25}\text{Be}_{34-x}\text{Ag}_x$ ($x = 2, 4, 6, 8$ at.%) glassy samples.

0 kJ/mol, -20 kJ/mol, -30 kJ/mol, 2 kJ/mol, and -43 kJ/mol, respectively [17]. Thus, in the Ti-Zr-Be-Ag alloy system, the strong chemical short-range order clusters or medium-range order clusters would be expected [18], which may restrain the diffusion of the atoms, and could suppress crystallization during the solidification. Meanwhile, the addition of Ag increases the number of the components in the alloy, which could generate more types of local ordering clusters and stabilize the liquid phase [18].

In addition, the electronegativity difference Δx and the atomic size difference parameter δ , the two parameters that related to the GFA of the glassy alloy, have been applied to evaluate the effect of Ag addition on the GFA of Ti-Zr-Be glassy alloy [19]. δ is defined as $\delta = \sqrt{\sum_{i=1}^n c_i(1 - r_i/\bar{r})}$, Δx is defined as $\Delta x = \sqrt{\sum_{i=1}^n c_i \times (x_i - \bar{x})^2}$, where $\bar{r} = \sum_{i=1}^N c_i r_i$, $\bar{x} = \sum_{i=1}^N c_i x_i$, c_i is the atomic fraction, r_i and x_i are atomic radius and electronegativity of i th element, and N is the number

of alloying elements [20, 21]. Δx and δ of Ti-Zr-Be-Ag glassy alloys were calculated and summarized in Figure 4.

According to the Hume-Rothery rules and Inoue's three empirical rules [20, 21], the alloys with larger value of δ and Δx could form amorphous phase readily. As shown in Figure 4, because Ag possesses larger Pauling electronegativity (1.91) than Ti (1.54), Zr (1.33), and Be (1.57), the addition of Ag would increase the value of Δx in the Ti-Zr-Be alloys, which effectively enhance the GFA. However, the value of δ would decrease as the content of Ag increase, which is not beneficial to improve the GFA [22]. When the content of Ag is relatively low, the beneficial effect of Δx dominates the alloying effect on GFA. So the critical size increases with Ag content and reached the maximum value of 10 mm at 6 at.%. When increasing Ag content again, the effect from δ would significantly reduce the beneficial effect from Δx , resulting in the decrease of GFA. Similar effects have also been observed in Ti-Zr-Be-Al [8] and Ti-Zr-Be-Fe [6] quaternary BMGs, too. Due to the efforts of these two factors, there would exist an optimized Ag content in the Ti-Zr-Be alloy system, which is 6 at.%.

5. Conclusion

In summary, Ag addition could significantly improve the GFA, thermal stability, and mechanical properties of the Ti-Zr-Be glassy alloys. By replacing Be with Ag, it has been found that the developed $\text{Ti}_{41}\text{Zr}_{25}\text{Be}_{28}\text{Ag}_6$ alloy possesses much better GFA; the critical diameter of the quaternary BMG has been increased to 10 mm, while that of ternary $\text{Ti}_{41}\text{Zr}_{25}\text{Be}_{34}$ [6] alloy is only 5 mm. This alloy also exhibits a yield strength of 1961 MPa, 10% higher than that of $\text{Ti}_{41}\text{Zr}_{25}\text{Be}_{34}$ BMG [6]. Furthermore, The Ti-Zr-Be-Ag glassy alloys have a wider supercooled liquid temperature range than that of the $\text{Ti}_{41}\text{Zr}_{25}\text{Be}_{34}$ glassy alloys, indicating a higher thermal stability of the glassy alloys. The enhanced GFA is supposed to be related to the improved atomic packing efficiency and high electronegativity difference, which can retard the atomic diffusion due to the addition of Ag.

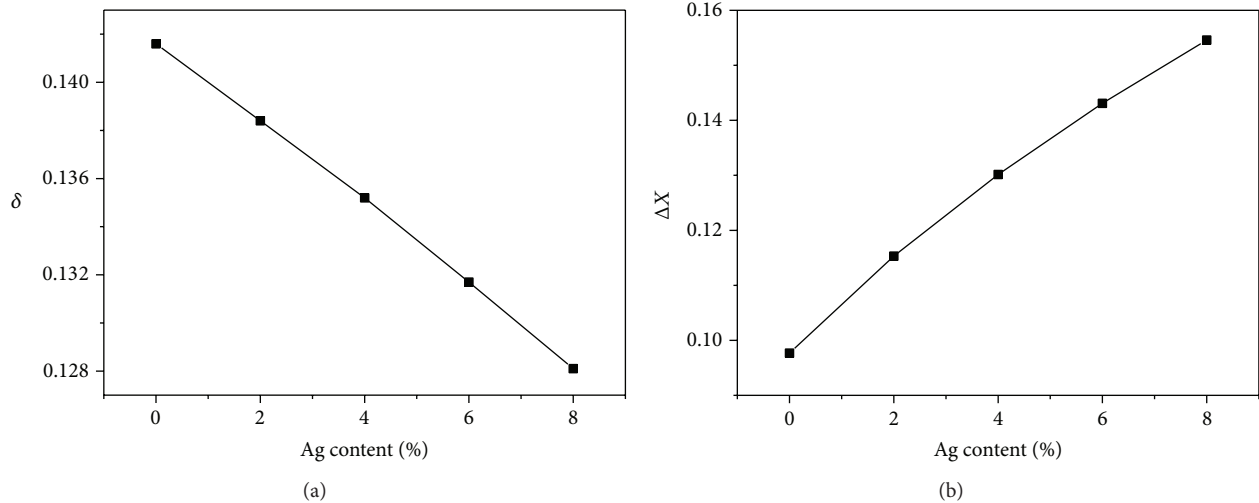


FIGURE 4: The atomic size parameter δ (a) and the electronegativity difference Δx (b) of $\text{Ti}_{41}\text{Zr}_{25}\text{Be}_{34-x}\text{Ag}_x$ ($x = 2, 4, 6, 8$ at.%) glassy alloys.

Conflict of Interests

The authors declare that there is no conflict of interests regarding the publication of this paper.

References

- [1] A. L. Greer, "Confusion by design," *Nature*, vol. 366, no. 6453, pp. 303–304, 1993.
- [2] K. F. Yao, F. Ruan, Y. Q. Yang, and N. Chen, "Superductile bulk metallic glass," *Applied Physics Letters*, vol. 88, no. 12, Article ID 122106, 2006.
- [3] K. F. Xie, K. F. Yao, and T. Y. Huang, "Preparation of $(\text{Ti}_{0.45}\text{Cu}_{0.378}\text{Zr}_{0.10}\text{Ni}_{0.072})_{100-x}\text{Sn}_x$ bulk metallic glasses," *Journal of Alloys and Compounds*, vol. 504, no. 1, pp. S22–S26, 2010.
- [4] D. E. Polk, A. Calka, and B. C. Giessen, "The preparation and thermal and mechanical properties of new titanium rich metallic glasses," *Acta Metallurgica*, vol. 26, no. 7, pp. 1097–1103, 1978.
- [5] Y. C. Kim, W. T. Kim, and D. H. Kim, "A development of Ti-based bulk metallic glass," *Materials Science and Engineering A*, vol. 375–377, no. 1-2, pp. 127–135, 2004.
- [6] P. Gong, K. Yao, and Y. Shao, "Effects of Fe addition on glass-forming ability and mechanical properties of Ti-Zr-Be bulk metallic glass," *Journal of Alloys and Compounds*, vol. 536, pp. 26–29, 2012.
- [7] P. Gong, K. F. Yao, X. Wang, and Y. Shao, "Centimeter-sized Ti-based bulk metallic glass with high specific strength," *Progress in Natural Science: Materials International*, vol. 22, pp. 401–406, 2012.
- [8] P. Gong, K. Yao, and Y. Shao, "Lightweight Ti-Zr-Be-Al bulk metallic glasses with improved glass-forming ability and compressive plasticity," *Journal of Non-Crystalline Solids*, vol. 358, pp. 2620–2625, 2012.
- [9] M. F. Ashby and A. L. Greer, "Metallic glasses as structural materials," *Scripta Materialia*, vol. 54, no. 3, pp. 321–326, 2006.
- [10] Y. Zhang, W. G. Zhang, J. P. Lin, G. J. Hao, G. L. Chen, and P. K. Liaw, "Glass-forming ability and competitive crystalline phases for lightweight Ti-Be-based alloys," *Metallurgical and Materials Transactions A*, vol. 41, no. 7, pp. 1670–1676, 2010.
- [11] Y. Zhang, J. Chen, G. L. Chen, and X. J. Liu, "Glass formation mechanism of minor yttrium addition in CuZrAl alloys," *Applied Physics Letters*, vol. 89, no. 13, Article ID 131904, 2006.
- [12] Z. B. Jiao, H. X. Li, J. E. Gao, Y. Wu, and Z. P. Lu, "Effects of alloying elements on glass formation, mechanical and soft-magnetic properties of Fe-based metallic glasses," *Intermetallics*, vol. 19, no. 10, pp. 1502–1508, 2011.
- [13] P. Gong, K. Yao, and H. Ding, "Centimeter-sized Ti-based quaternary bulk metallic glass prepared by water Quenching," *International Journal of Modern Physics B*, vol. 27, no. 18, 2013.
- [14] P. Gong, K. Yao, X. Wang, and Y. A. Shao, "A new centimeter-sized Ti-based quaternary bulk metallic glass with good mechanical properties," *Advanced Engineering Materials*, vol. 15, pp. 691–696, 2013.
- [15] Z. P. Lu and C. T. Liu, "A new glass-forming ability criterion for bulk metallic glasses," *Acta Materialia*, vol. 50, no. 13, pp. 3501–3512, 2002.
- [16] Z. P. Lu, Y. Li, and S. C. Ng, "Reduced glass transition temperature and glass forming ability of bulk glass forming alloys," *Journal of Non-Crystalline Solids*, vol. 270, no. 1–3, pp. 103–114, 2000.
- [17] A. Takeuchi and A. Inoue, "Classification of bulk metallic glasses by atomic size difference, heat of mixing and period of constituent elements and its application to characterization of the main alloying element," *Materials Transactions*, vol. 46, no. 12, pp. 2817–2829, 2005.
- [18] G. Chen, X. Hui, S. Fan, H. Kou, and K. Yao, "Concept of chemical short range order domain and the glass forming ability in multicomponent liquid," *Intermetallics*, vol. 10, no. 11-12, pp. 1221–1232, 2002.
- [19] O. N. Senkov and D. B. Miracle, "Effect of the atomic size distribution on glass forming ability of amorphous metallic alloys," *Materials Research Bulletin*, vol. 36, no. 12, pp. 2183–2198, 2001.
- [20] A. Takeuchi and A. Inoue, "Quantitative evaluation of critical cooling rate for metallic glasses," *Materials Science and Engineering A*, vol. 304–306, no. 1-2, pp. 446–451, 2001.

- [21] S. Fang, X. Xiao, L. Xia, W. Li, and Y. Dong, "Relationship between the widths of supercooled liquid regions and bond parameters of Mg-based bulk metallic glasses," *Journal of Non-Crystalline Solids*, vol. 321, no. 1-2, pp. 120–125, 2003.
- [22] A. Inoue and A. Takeuchi, "Recent development and application products of bulk glassy alloys," *Acta Materialia*, vol. 59, no. 6, pp. 2243–2267, 2011.

Research Article

Enzyme-Free Electrochemical Glucose Sensors Prepared by Dealloying Pd-Ni-P Metallic Glasses

Yuqiao Zeng,¹ Hua Xiang,¹ Chunlei Yang,¹ Shengchen Yang,¹ Luyang Chen,² Mingwei Chen,² Akihisa Inoue,² Xuhai Zhang,¹ and Jianqing Jiang¹

¹ Jiangsu Key Laboratory of Advanced Metallic Materials, School of Materials Science and Engineering, Southeast University, Nanjing 211189, China

² Institute for Materials Research, Tohoku University, Sendai 980-8577, Japan

Correspondence should be addressed to Yuqiao Zeng; zyuqiao@hotmail.com

Received 21 February 2014; Revised 7 March 2014; Accepted 10 March 2014; Published 15 April 2014

Academic Editor: Na Chen

Copyright © 2014 Yuqiao Zeng et al. This is an open access article distributed under the Creative Commons Attribution License, which permits unrestricted use, distribution, and reproduction in any medium, provided the original work is properly cited.

We report the formation of enzyme-free electrochemical glucose sensors by electrochemical dealloying palladium-containing Pd-Ni-P metallic glasses. When metallic glasses with different Pd contents are used as the dealloying precursor alloys, palladium-based nanoporous metals with different ligament and pore sizes can be obtained. The chemical compositions of the nanoporous metals also vary according to the different precursor compositions. All the as-obtained nanoporous metals exhibit electrochemical catalytic activity towards the oxidation of d-glucose, indicating that the nanoporous metals prepared by dealloying the Pd-Ni-P metallic glasses are promising materials for enzyme-free electrochemical glucose sensor.

1. Introduction

Dealloying (chemical or electrochemical) is a simple and effective way to prepare well-defined nanoporous metals (NPMs) that are regarded as one of the most promising new materials for functional applications in nanotechnology [1–5]. Since the nanoporosity is formed by a self-assembly process through surface diffusion instead of excavating one phase from a pre-separated multiphase system, the dealloying precursors should be homogenous with no phase separation prior to dealloying [5]. Usually, crystalline intermetallic compounds or solid solution alloys are used as the dealloying precursors. Recently, there are some attempts to synthesize NPMs by dealloying metallic glasses. For example, using Pd₃₀Ni₅₀P₂₀ metallic glass as a dealloying starting alloy, Yu et al. succeeded in fabricating pure NPPd which exhibited high catalytic activity towards the oxidation of formic acid [6], indicating that metallic glass is a new suitable system to form useful NPMs.

In this study, we report the formation of Pd-based NPMs which exhibit high catalytic activity towards the electrochemical oxidation of glucose. Enzyme-free electrochemical glucose sensors are based on the utilization of nonenzymatic

catalyzer for the conversion of the target analytes into electrochemically detectable products. Due to the simple assembling and high sensitivity, the enzyme-free electrochemical glucose sensors have attracted considerable interest in the field of both industrial applications and theoretical applications. NPMs, such as NPd and NPPt with a bicontinuous network structure and a tunable feature dimension, have proven to be very active in the oxidation of glucose, making them ideal glucose sensing material [7–9]. In this study, NPPd enzyme-free electrochemical glucose sensors with high catalytic activity are successfully prepared by dealloying Pd_xNi_{80-x}P₂₀ metallic glasses.

2. Experimental

The Pd_xNi_{80-x}P₂₀ ($x = 10, 20, 40$) mother alloys were prepared by melting the mixture of pure Pd (purity, 99.9 wt%) and Ni (purity, 99.95 wt%) elements with prealloyed Ni-P ingots in vacuum fused silica tubes, followed by B₂O₃ flux treatment. From the mother alloys, glassy ribbons with a thickness of about 0.02 mm and a width of about 2 mm were fabricated by single-roller melt-spinning technique at

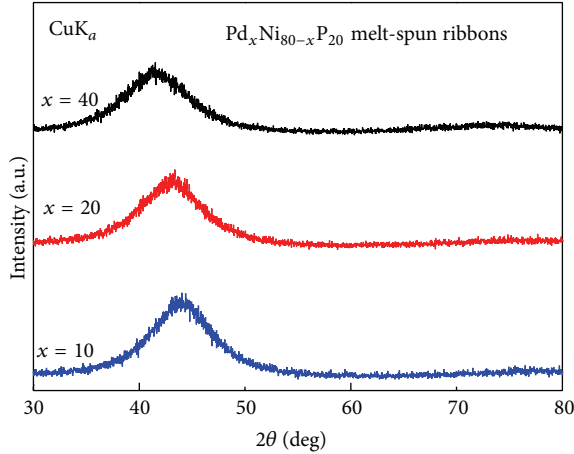


FIGURE 1: XRD patterns of the $\text{Pd}_x\text{Ni}_{80-x}\text{P}_{20}$ ($x = 10, 20, 40$) ribbon samples.

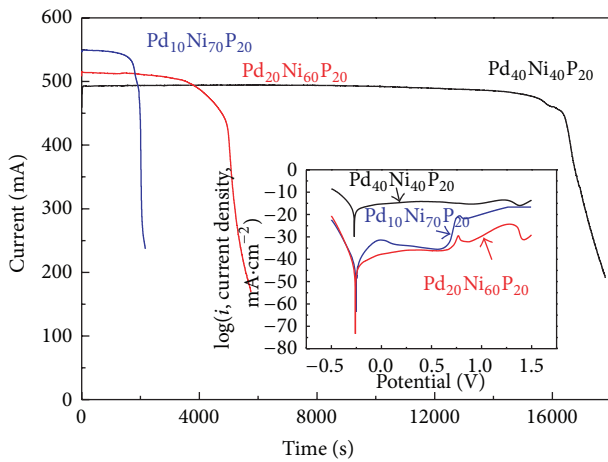


FIGURE 2: Chronoamperometric (current density versus time) curves for the potentiostatic dealloying of the $\text{Pd}_x\text{Ni}_{80-x}\text{P}_{20}$ metallic glasses in $0.8\text{ M H}_2\text{SO}_4 + 0.2\text{ M H}_3\text{PO}_4$ solution at 0.80 V and the inset is the polarization curves of $\text{Pd}_x\text{Ni}_{80-x}\text{P}_{20}$ metallic glasses in $0.8\text{ M H}_2\text{SO}_4 + 0.2\text{ M H}_3\text{PO}_4$.

a copper wheel velocity of about 40 ms^{-1} . The amorphous structure of the as-prepared ribbons was confirmed by X-ray diffraction (XRD). With the aim of clarifying the proper dealloying potential range, the potentiodynamic polarization test was performed on the $\text{Pd}_x\text{Ni}_{80-x}\text{P}_{20}$ glassy ribbon in $0.8\text{ M H}_2\text{SO}_4 + 0.2\text{ M H}_3\text{PO}_4$ solution and 0.80 V (versus SCE) was chosen as the dealloying potential. The NPMs were then fabricated by potentiostatically (0.80 V versus SCE) etching the $\text{Pd}_x\text{Ni}_{80-x}\text{P}_{20}$ metallic glasses in a $0.8\text{ M H}_2\text{SO}_4 + 0.2\text{ M H}_3\text{PO}_4$ mixed electrolyte. The dealloying process was carried out by using a classical three-electrode setup (ZF-10) with a saturated calomel reference electrode (SCE), a Pt counter electrode, and a $\text{Pd}_x\text{Ni}_{80-x}\text{P}_{20}$ working electrode. The samples prepared by dealloying $\text{Pd}_{10}\text{Ni}_{70}\text{P}_{20}$, $\text{Pd}_{20}\text{Ni}_{60}\text{P}_{20}$ and $\text{Pd}_{40}\text{Ni}_{40}\text{P}_{20}$ glasses are named as NPM 1#, NPM 2#, and NPM 3#, respectively, in the following description. The morphology of the NPMs was observed

by scanning electron microscopy (SEM) and the chemical compositions were identified by an energy dispersive X-ray spectrometer (EDS). The catalytic properties of the Pd-based NPMs towards the oxidation of d-glucose were evaluated by cyclic voltammetry (CV) measurements in a CHI-760D electrochemical workstation, where the NPMs were used as the working electrode, a Pt foil was used as a counter electrode, and an SCE was used as the reference electrode. All the aqueous solutions used in the CV test were prepared with triply distilled water and deoxygenated by bubbling high purity N_2 for half an hour.

3. Results and Discussion

The XRD patterns of the $\text{Pd}_x\text{Ni}_{80-x}\text{P}_{20}$ ($x = 10, 20, \text{ and } 40$) ribbons in Figure 1 show only a broad diffraction maximum without any observable crystalline peaks, demonstrating the formation of a homogenous amorphous structure in all the dealloying precursors.

With the aim of finding out a proper dealloying potential for the three glasses with different Pd content, the potentiodynamic polarization test is performed on $\text{Pd}_x\text{Ni}_{80-x}\text{P}_{20}$ ribbon in $0.8\text{ M H}_2\text{SO}_4$ and $0.2\text{ M H}_3\text{PO}_4$ solutions and the results are shown in the inset of Figure 2; all the $\text{Pd}_x\text{Ni}_{80-x}\text{P}_{20}$ ribbons firstly experience a spontaneous passivation in the anodic region (about 0 to 0.70 V), where dealloying can hardly occur due to the extremely low current density. A rapid current density rise appears at about $0.75\text{--}0.80\text{ V}$ and the current ‘‘apex nasi’’ (critical dealloying potential) increases with the Pd content in $\text{Pd}_x\text{Ni}_{80-x}\text{P}_{20}$. This result may be attributed to the difference in potential required to dissolve Ni and Pd components in their pure form. According to the theoretical computation [5] and practical experiments [10], the bulk critical dealloying potential of the precursor alloys increases as the content of the component with higher standard electrode potential increases. In this study, the standard electrode potential of Pd/Pd^{2+} is 0.34 V , much higher than that of Ni/Ni^{2+} (-0.25 V). Therefore, the increase of Pd in metallic glasses leads to higher critical dealloying potential. Since the selective etching of Ni and P can take place above 0.80 V in all the $\text{Pd}_x\text{Ni}_{80-x}\text{P}_{20}$ glasses, 0.80 V is chosen as the standard dealloying potential to form NPMs. As is shown in Figure 2, the dealloying process of three glasses is mainly composed of two current stages, similar to that of dealloying solid solutions and intermetallic metals: steady stage and decay stage [11]. The steady stage increases obviously with increasing Pd content in the metallic glasses, which may be attributed to the different overpotential used in dealloying the glasses. Since it has the highest critical dealloying potential among the three glasses, the $\text{Pd}_{40}\text{Ni}_{40}\text{P}_{20}$ glass is dealloyed at the lowest overpotential (the different between the applied dealloying potential and the critical dealloying potential). Similarly, the $\text{Pd}_{10}\text{Ni}_{70}\text{P}_{20}$ glass is dealloyed at the highest overpotential. As a consequence, the dealloying kinetic decreases with the increasing Pd content in $\text{Pd}_x\text{Ni}_{80-x}\text{P}_{20}$ glasses though the applied dealloying potential is the same for all three dealloying precursors.

Figure 3 shows the SEM images of the as-obtained NPM 1# (a), NPM 2# (b), and NPM 3# (c). All the samples exhibit

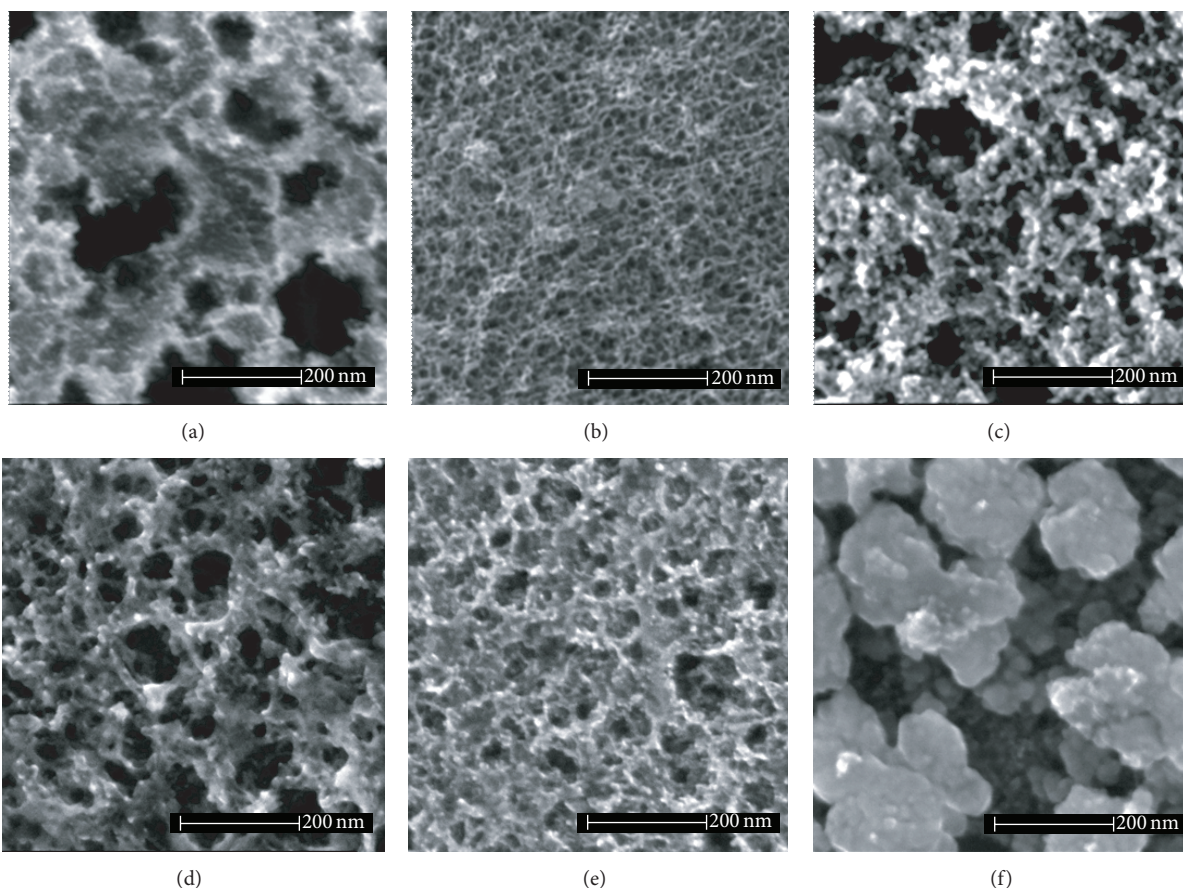


FIGURE 3: SEM images of the as-obtained NPMs (NPM 1#: (a), NPM 2#: (b), and NPM 3#: (c)) and the NPMs subjected to 1000 potential cycles in 0.1 M KOH solution containing 50 mM glucose (NPM 1#: (d), NPM 2#: (e), and NPM 3#: (f)).

an open, three-dimensional, ligament-channel nanoporous structure, indicating that NPMs can be obtained by dealloying the $\text{Pd}_x\text{Ni}_{80-x}\text{P}_{20}$ metallic glasses with a Pd content ranging within 10–40 at%. NPM 1# contains a rather coarse nanoporous structure, as is evidenced by the inhomogeneous pores with a size ranging within 5–200 nm and ligaments with a width of 7–8 nm. The increase of the Pd content to 20 at% in the metallic glass results in a refined nanostructure in NPM 2#, where nanopores of 10–20 nm and metallic ligaments of 7–8 nm are homogeneously dispersed. The finer structure may be attributed to the combination of relatively low dealloying overpotential and short dealloying time. Lower overpotential usually leads to higher activation energy for the diffusion of the noble element and thus improves the fine nanostructure in the NPM 2# [5, 12]. The short dealloying time is another important factor. Since the dealloying time is relatively short, the diffusion distance of Pd is limited. Thus, large pores and ligaments can barely form. Similar with NPM 1#, NPM 3# exhibits a coarse microstructure with nanopores ranging within 10–100 nm and metallic ligaments within 10–50 nm. The coarsening of NPM 3# may be caused by the much longer dealloying time. The dealloying kinetic of $\text{Pd}_{40}\text{Ni}_{40}\text{P}_{20}$ is the lowest among the glasses in this study and longer dealloying time is required to fully dealloy the $\text{Pd}_{40}\text{Ni}_{40}\text{P}_{20}$ glass. In the located areas where the selective cession is complete, pure

coarsening of the ligaments takes place and leads to located collapse. The morphology of NPM 3#, thus, becomes coarse and inhomogeneous.

The chemical compositions of the NPMs measured by EDS are summarized in Table 1. The results show that all the NPMs are mainly composed of Pd, together with a small amount of Ni and P, indicating that Pd-based NPMs are obtained. The preservation of much positive Ni and P elements in porous Pd can be explained by the core-shell structure which forms during dealloying [13]. When the positive elements (Ni and P) dissolve, the inert Pd atoms will be liberated and accumulated on the surface of the ligaments, forming a Pd or Pd-rich shell. If the applied dealloying potential is lower than the critical dealloying potential of the newly formed shell, no further dissolution is possible. Both Ni and P residuals in NPMs decrease with the increasing Pd content in $\text{Pd}_x\text{Ni}_{80-x}\text{P}_{20}$ metallic glasses; that is, Ni decreases from 5.94 at% in NPM 1# to 3.00 at% in NPM 3#, and P goes down from 4.1 at% NPM 1# to 2.00 at% in NPM 3# when the Pd content in the glass precursors increases from 10 to 40 at%.

The electrocatalytic activities of the as-prepared NPMs towards glucose electrooxidation were characterized by CV curves in 0.1 M KOH alkaline aqueous solutions with and without 50 mM of glucose (Figure 4). In 0.1 M KOH + 50 mM glucose solutions, all the NPMs exhibit a sharp current

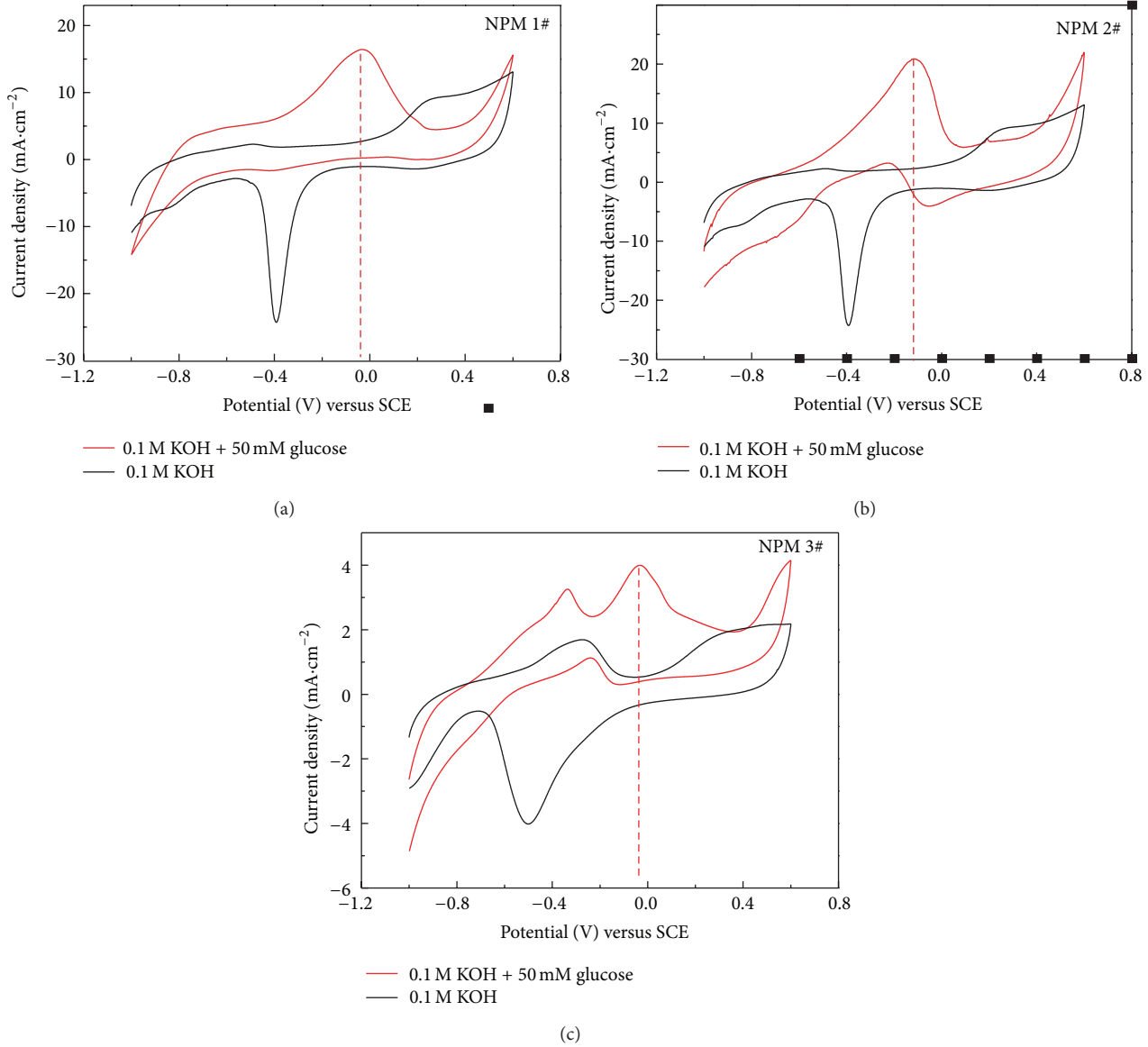


FIGURE 4: CV curves of the NPMs in 0.1 M KOH solution with and without 50 mM glucose, scan rate: 0.05 V/s.

TABLE 1: Chemical compositions of the as-obtained NPMs.

Samples	Pd (at%)	Ni (at%)	P (at%)
NPM 1#	89.54	5.94	4.1
NPM 2#	90.74	3.55	5.71
NPM 3#	95.00	3.00	2.00

density peak at the potential range from -0.10 V to -0.03 V, which cannot be detected in pure KOH solution. According to the former related reports, the current peak is associated to the absorption of OH^{-1} and the oxidation of glucose and intermediate [14], indicating that the NPMs prepared by dealloying the $\text{Pd}_x\text{Ni}_{80-x}\text{P}_{20}$ metallic glasses have catalytic activity towards the electrochemical oxidation of glucose.

The current density/the potential of oxidation peak of NPM 1#, NPM 2# and NPM 3# are about $16.3 \text{ mA}\cdot\text{cm}^{-2}/-0.03$ V, $20.9 \text{ mA}\cdot\text{cm}^{-2}/-0.1$ V and $4 \text{ mA}\cdot\text{cm}^{-2}/-0.03$ V, respectively. Clearly, NPM 2# with the smallest pore size shows the highest oxidation current density and the lowest oxidation potential. Similar phenomenon has been found in other NPMs. For instance, Ge et al. studied the size effect of NP Au for methanol electrooxidation. They found that the smaller pore and ligament size leads to higher electrooxidation activity, consistent with our results [3].

The electrochemical stabilities of the NPMs prepared by dealloying $\text{Pd}_x\text{Ni}_{80-x}\text{P}_{20}$ glasses are also investigated by CV tests for 1000 potential cycles performed in KOH alkaline aqueous solutions with 50 mM glucose and the results are shown in Figure 5. After 1000 times of CV scans, the oxida-

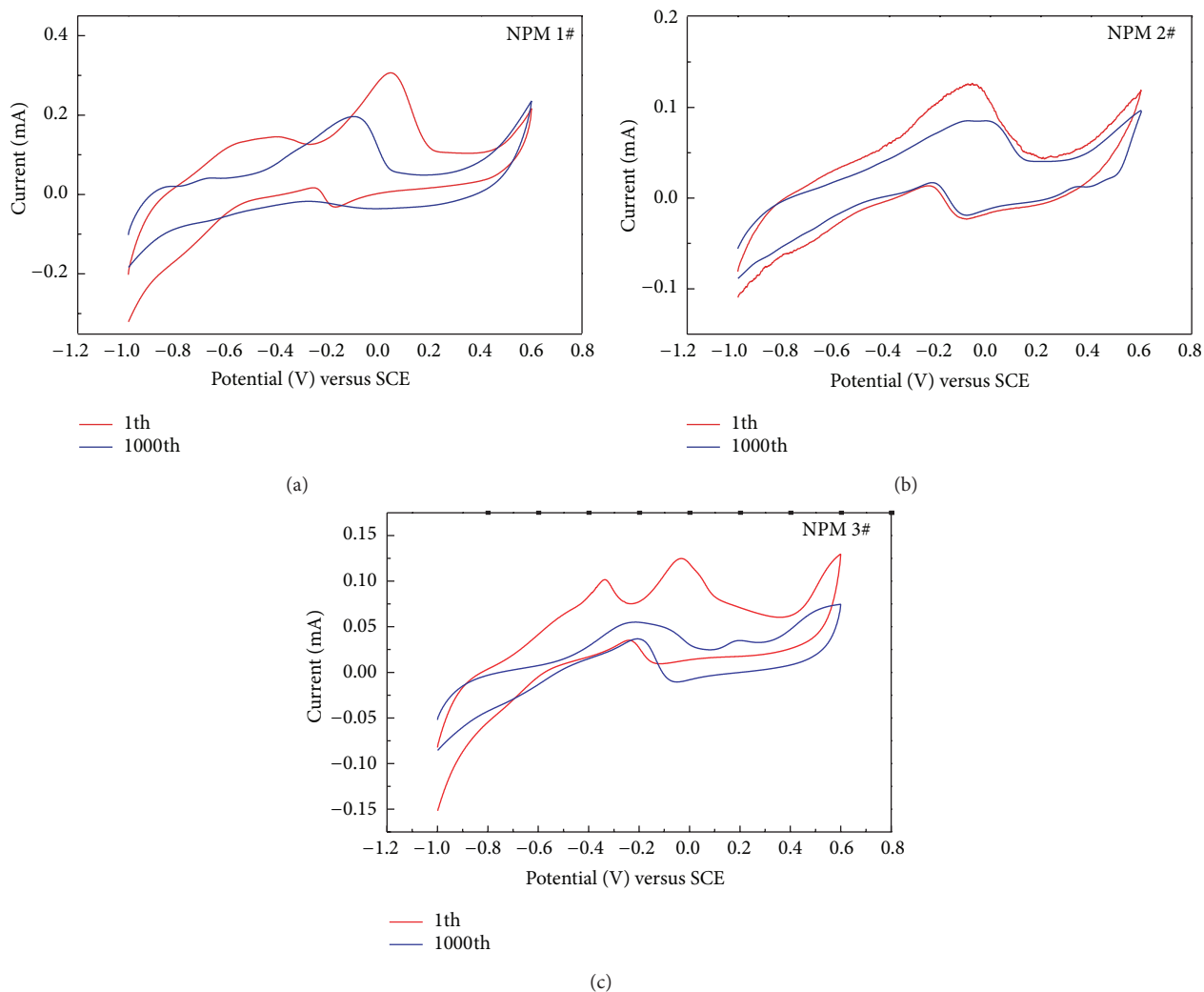


FIGURE 5: CV curves of the NPMs in 0.1 M KOH solutions containing 50 mM glucose during 1000 potential cycles.

tion peak of NPM 1# shifts to lower potential and the peak density drops to 67% of the first test value. In the case of the NPM 2#, the peak density is 64% of the first test value while the peak potential does not move. For NPM 3#, the catalytic activity suffers the most serious gradation, as evidenced from the disappearance of the characteristic oxidation peak. To further clarify the reason which leads to the different catalytic stability of the NPMs, the morphology of the NPMs that undergo 1000 times of CV scans is investigated and the results are shown in Figures 3(d)-3(e). Coarsening of the nanopores and ligaments can be vividly seen in all the NPMs. In NPM 1#, the pores size is almost the same as that of the as-obtained NPM 1#, but the ligaments increase up to about 25–50 nm. In NPM 2#, the pores size increases up to 10–100 nm and the ligaments are about 25–50 nm. The most apparent nanostructure coarsening can be observed in NPM 3# after 1000 times of CV scans. The ligaments degenerate and aggregate to nanoparticles with a size of about 200 nm and the bicontinuous ligaments-nanoporous structure can hardly be seen. The coarsenes structure may cause the great decrease of the active Pd sites and the catalytic actively of the NPMs.

4. Conclusion

Pd-based NPMs can be prepared by dealloying the $\text{Pd}_x\text{Ni}_{80-x}\text{P}_{20}$ metallic glasses ($x = 10, 20, 40$). When the content of Pd content is 20 at% in the $\text{Pd}_x\text{Ni}_{80-x}\text{P}_{20}$ metallic glass, Pd-based NPM with the most homogeneous nanoporous structure can be obtained and it is chemically active to the electrochemical oxidation of glucose.

Conflict of Interests

The authors declare that there is no conflict of interests regarding the publication of this paper.

Acknowledgments

This work is supported by the National Science Foundation of China (51001026), the Project sponsored by SRF for ROCS, SEM (6812000013), the Project sponsored by Nanjing for ROCS (7912000011), Opening Project of Jiangsu Key Laboratory of Advanced Metallic Materials (AMM201101), and

the Fundamental Research Funds for the Central Universities (3212002205, 3212003102).

References

- [1] J. Erlebacher, M. J. Aziz, A. Karma, N. Dimitrov, and K. Sieradzki, "Evolution of nanoporosity in dealloying," *Nature*, vol. 410, no. 6827, pp. 450–453, 2001.
- [2] T. Fujita, L. H. Qian, K. Inoke, J. Erlebacher, and M. W. Chen, "Three-dimensional morphology of nanoporous gold," *Applied Physics Letters*, vol. 92, no. 25, Article ID 251902, 2008.
- [3] X. Ge, R. Wang, P. Liu, and Y. Ding, "Platinum-decorated nanoporous gold leaf for methanol electrooxidation," *Chemistry of Materials*, vol. 19, no. 24, pp. 5827–5829, 2007.
- [4] Z. Yi, X. Tan, G. Niu et al., "Facile preparation of dendritic Ag-Pd bimetallic nanostructures on the surface of Cu foil for application as a SERS-substrate," *Applied Surface Science*, vol. 258, no. 14, pp. 5429–5437, 2012.
- [5] J. Erlebacher, "An atomistic description of dealloying porosity evolution, the critical potential, and rate-limiting behavior," *Journal of the Electrochemical Society*, vol. 151, no. 610, pp. 616–624, 2004.
- [6] J. Yu, Y. Ding, C. Xu, A. Inoue, T. Sakurai, and M. Chen, "Nanoporous metals by dealloying multicomponent metallic glasses," *Chemistry of Materials*, vol. 20, no. 14, pp. 4548–4550, 2008.
- [7] D. van Noort and C. F. Mandenius, "Porous gold surfaces for biosensor applications," *Biosensors and Bioelectronics*, vol. 15, no. 3-4, pp. 203–209, 2000.
- [8] Z. Liu, L. Huang, L. Zhang, H. Ma, and Y. Ding, "Electrocatalytic oxidation of d-glucose at nanoporous Au and Au-Ag alloy electrodes in alkaline aqueous solutions," *Electrochimica Acta*, vol. 54, no. 28, pp. 7286–7293, 2009.
- [9] Y. Ding, Y. J. Kim, and J. Erlebacher, "Nanoporous gold leaf: "Ancient technology"/advanced material," *Advanced Materials*, vol. 16, no. 21, pp. 1897–1900, 2004.
- [10] J. Xu, Y. Wang, and Z. Zhang, "Potential and concentration dependent electrochemical dealloying of Al₂Au in sodium chloride solutions," *Journal of Physical Chemistry C*, vol. 116, no. 9, pp. 5689–5699, 2012.
- [11] N. Tavakkoli and S. Nasrollahi, "Non-enzymatic glucose sensor based on palladium coated nanoporous gold film electrode," *Australian Journal of Chemistry*, vol. 66, pp. 1097–1104, 2013.
- [12] L. H. Qian and M. W. Chen, "Ultrafine nanoporous gold by low-temperature dealloying and kinetics of nanopore formation," *Applied Physics Letters*, vol. 91, no. 8, Article ID 083105, 2007.
- [13] A. J. Forty, "Corrosion micromorphology of noble metal alloys and depletion gilding," *Nature*, vol. 282, no. 5739, pp. 597–598, 1979.
- [14] Y. Kuang, B. Wu, D. Hu, X. Zhang, and J. Chen, "One-pot synthesis of highly dispersed palladium nanoparticles on acetylenic ionic liquid polymer functionalized carbon nanotubes for electrocatalytic oxidation of glucose," *Journal of Solid State Electrochemistry*, vol. 16, no. 2, pp. 759–766, 2012.